IV Electroweak interactions

We now turn to the electroweak interactions, which is arguably the most subtle and mysterious of forces that remain at the forefront of research. We first look at some of the measurements at low energies mostly in the 1950s concerning weak interactions, in particular broken discrete symmetries. Historically, this was first manifested by nuclear beta decay of nuclei and then by muon and pion decays. Today, we now know these weak interactions are mediated by the $W^{\pm}$ boson and Z bosons, which require constructing city-sized colliders and house-sized experiments to create. Finally, we discuss more contemporary topics of the Higgs boson and neutrino oscillations.

12 Low-energy beta decay

Decades after beta decay had been discovered, we now know the fundamental interaction is a W^- boson mediating a neutron turning into a proton alongside an electron and anti-neutrino:

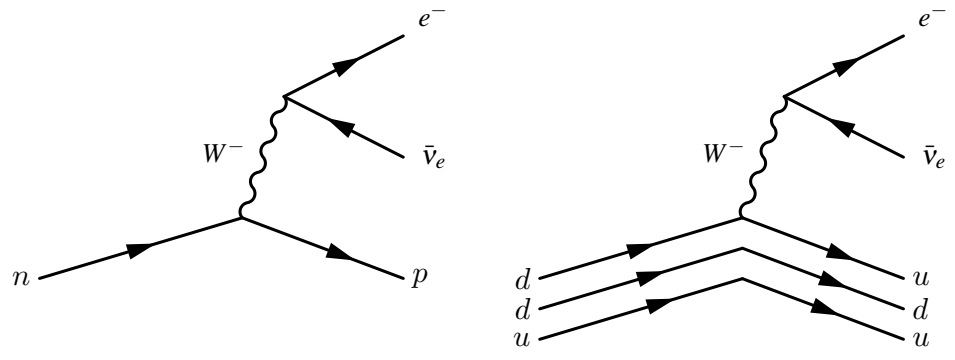

(12.1)

The right diagram shows but with quark lines for the neutron and proton, illustrating the down transformed into an up quark with the other two spectator quarks unchanged.

The simplest beta decay involves purely leptonic interactions such as muon decay

$$\mu^- \to e^- + \bar{\nu}_e + \nu_\mu . \tag{12.2}$$

The Feynman diagram for this process is:

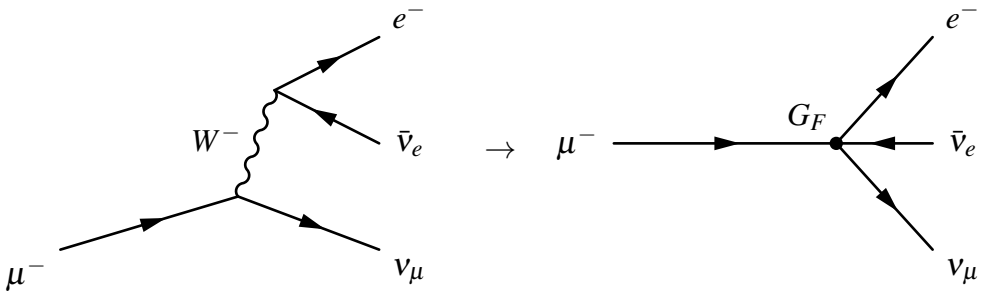

(12.3)

This shows the low-energy limit, where W^- is highly off-shell so can be described by a three-point Fermi interaction vertex.

The tau-lepton is the heaviest lepton with 1.776 GeV mass and therefore can also beta decay via a highly off-shell $W^\pm$ boson to both electrons and muons:

$$\tau^- \to e^- + \bar{\nu}_e + \nu_\tau, \tag{12.4}$$

$$\tau^- \to \mu^- + \bar{\nu}_\mu + \nu_\tau. \tag{12.5}$$

This dual-flavour decay is the pivotal signature for how the tau-lepton was discovered in 1975 at the SPEAR electron–positron collider in SLAC, California. When they ramped the beam energy above around $\sqrt{s} = 4$ GeV, this triggered production of opposite-charge different-flavour leptons plus missing momentum:

$$e^+e^- \to e^\pm\mu^\mp + \geq 2 \text{ invisible particles}, \tag{12.6}$$

with no other charged particles or photons. The authors conclude pretty frankly [79]:

> "We have no conventional explanation for these events."

This was the tell-tale discovery of a new particle: the tau-lepton $\tau^\pm$.

12.1 Fermi theory of weak decays

The electroweak fine structure coupling α_{EW} around the Z boson mass:

$$\alpha_{\text{EW}} \simeq \frac{1}{30} \tag{12.7}$$

Intriguingly, this is larger than the electromagnetic fine structure constant $\alpha_{\text{EM}} \simeq 1/128$. The weakness of the weak force arises due to the heaviness of the electroweak bosons. The Fermi coupling is a dimensionful quantity

$$G_F \simeq \frac{\pi}{\sqrt{2}} \frac{\alpha_{\text{EW}}}{m_W^2} \simeq 1.166 \times 10^{-5}\ \text{GeV}^{-2} = 90\ \text{eV fm}^3. \tag{12.8}$$

We can see the smallness of G_F is due to the factor of $1/m_W^2$ suppressing this. For momentum transfer q, the propagator Π_W for the W boson has a dependence

$$\Pi_W \propto \frac{1}{q^2 - m_W^2}. \tag{12.9}$$

When the momentum transfer is much smaller than the W mass $q^2 \ll m_W^2$, this reduces to the form seen in the Fermi constant. In the case of nuclear beta decays, the typical energies are on the order of 100s of MeV at most, which is far below m_W. This is an example of an effective field theory.

Fermi proposed the first successful theory to explain and predict beta decay rates. The theory assumes 4 particle interactions take place at a single point in spacetime whose amplitude is governed by the **Fermi coupling constant**. This ignores the Coulomb interaction and is a good approximation for sufficiently high electron energies. At the low energies in Fermi theory, we assume G_F to be a universal constant.

Consider beta β^- decay. Let the initial state be $|i\rangle$ and the final state $|f\rangle$ be

$$|i\rangle = |\psi_i\rangle, \qquad |f\rangle = |\psi_f\rangle|\psi_e\rangle|\psi_\nu\rangle$$

where the product of the final nuclear, electron and anti-neutrino respectively states We wish to calculate the interaction amplitude $\mathscr{M}_{fi} = \langle f|H_{\text{int}}|i\rangle$ given by

$$\langle f|\mathscr{A}|i\rangle = \int G_F \psi_e^* \psi_\nu^* \psi_f^* \psi_i \, \mathrm{d}^3\mathbf{r} \tag{12.10}$$

Now assume the outgoing electron and anti-neutrino are plane waves

$$\langle \mathbf{r}|\psi_e\rangle = \frac{\mathrm{e}^{\mathrm{i}\mathbf{p_e}\cdot\mathbf{r}}}{L^{3/2}}, \qquad \langle \mathbf{r}|\psi_\nu\rangle = \frac{\mathrm{e}^{\mathrm{i}\mathbf{p}_\nu\cdot\mathbf{r}}}{L^{3/2}}, \tag{12.11}$$

where L^3 is some normalising volume (that will cancel in the end result). Taylor expand the product $\psi_e^*\psi_\nu^*$:

$$\psi_e^*\psi_\nu^* \approx 1 - \mathrm{i}(\mathbf{p}_e + \mathbf{p}_\nu)\cdot\mathbf{r} \tag{12.12}$$

Provided the first term is non-vanishing on integration, we expect it to dominate. We justify the higher ordered terms are small by noting the nuclear energies pc and sizes r are of order MeV and 10 fm respectively

$$\left|\frac{(\mathbf{p}_e + \mathbf{p}_\nu)\cdot\mathbf{r}}{\hbar}\right| \sim \frac{pc}{\hbar c} r \sim \frac{\text{MeV}}{197 \text{ MeV fm}} 10 \text{ fm} \sim \frac{1}{20} \tag{12.13}$$

with $\hbar c \approx 197$ MeV fm. So the amplitude (12.10) is related by the Fermi constant G_F and a matrix element $\mathscr{M}_{fi}$ dependent only on the initial and final nuclear states:

$$\mathscr{M}_{fi} = \frac{1}{L^3}\int G_F \psi_f^* \psi_i \mathrm{d}^3\mathbf{r} = \frac{G_F}{L^3} M_{\text{nucl}} \tag{12.14}$$

The differential rate of transitioning from an initial state $|i\rangle$ to some final state $|f\rangle$ with electron energy in interval $[E_e, E_e + \mathrm{d}E_e]$ is given by the Fermi golden rule:

$$\frac{\mathrm{d}w}{\mathrm{d}E_e} = 2\pi |\langle f|\mathscr{H}_{\text{int}}|i\rangle|^2 \frac{\mathrm{d}N_\nu}{\mathrm{d}E_\nu}\frac{\mathrm{d}N_e}{\mathrm{d}E_e} \tag{12.15}$$

where $\mathrm{d}N_{\nu,e}/\mathrm{d}E_{\nu,e}$ are the densities states of the free neutrino and electron. Here w is the decay rate, related to the mean lifetime τ by $w = 1/\tau$. The neutrino density of states is

$$\frac{\mathrm{d}N_\nu}{\mathrm{d}p_\nu} = \left(\frac{L}{2\pi}\right)^3 p_\nu^2 \mathrm{d}p_\nu \mathrm{d}\Omega \tag{12.16}$$

Integrating over the solid angle and using $\mathrm{d}p_\nu/\mathrm{d}E_\nu = E_\nu/p_\nu$, we obtain

$$\frac{\mathrm{d}N_\nu}{\mathrm{d}E_\nu} = \left(\frac{L}{2\pi\hbar}\right)^3 4\pi p_\nu E_\nu \tag{12.17}$$

With a similar expression for the electron density of states, the Fermi Golden Rule becomes

$$\frac{\mathrm{d}w}{\mathrm{d}E_e} = 2\pi G_F^2 \left|M_{\text{nucl}}\right|^2 \frac{(4\pi)^2}{(2\pi)^6} p_\nu E_\nu p_e E_e \tag{12.18}$$

Changing variables to p_e and letting the neutrino be massless such that $E_\nu = p_\nu c$, we obtain

$$\frac{\mathrm{d}w}{\mathrm{d}p_e} = \frac{\mathrm{d}E_e}{\mathrm{d}p_e}\frac{\mathrm{d}w}{\mathrm{d}E_e} = \frac{G_F^2 \left|M_{\text{nucl}}\right|^2}{2\pi^3} p_e^2 E_\nu^2 \tag{12.19}$$

Letting $\mathscr{Q} = E_e - E_\nu$ be the total energy released in the beta decay, we obtain

$$\frac{\mathrm{d}w}{\mathrm{d}p_e} = \frac{G_F^2 \left|M^{\text{nucl}}\right|^2}{2\pi^3} p_e^2 (Q - E_e)^2 \tag{12.20}$$

In the ultrarelativistic limit $E_e \approx p_e c$, we can integrate over the electron energies analytically to obtain **Sargent's rule**

$$\boxed{w \propto \int_0^{\mathscr{Q}} E_e^2 (\mathscr{Q} - E_e)^2 \mathrm{d}E_e = \frac{\mathscr{Q}^5}{30}} \tag{12.21}$$

The rate of beta decay w is proportional to the fifth power of the energy released $\mathscr{Q}^5$. In the case of muon lifetime τ_μ, the muon mass is converted into energy released and we have the lifetime

$$\frac{1}{\tau_\mu} = \Gamma_\mu \propto G_F^2 m_\mu^5. \tag{12.22}$$

12.2 Neutrino direct detection

Clyde Cowan and NYU alumnus Frederick Reines led a definitive experiment in 1956 that enabled the first direct detection of neutrinos [80]. This utilised nuclear reactor at the Savannah River Plant in South Carolina as the source of neutrinos from neutron beta decay. Beta decays $n \to p + e^- + \bar{\nu}_e$ occurs at nuclear reactors and they proposed detecting the anti-neutrinos via inverse beta decay:

$$\bar{\nu}_e + p \to n + e^+. \tag{12.23}$$

From Fermi theory, Hans Bethe and Rudolf Peierls first calculated in 1934 [81] that for a neutrino with 2.3 MeV energy, this process would have an very small cross-section no larger than

$$\sigma \lesssim 10^{-44}\ \text{cm}^2. \tag{12.24}$$

They concluded that:

> "It seems highly improbable that, even for cosmic ray energies, the cross-section becomes large enough to allow the process to be observed."

Fortunately, they could neither foresee the development of large neutrino fluxes from nuclear reactions nor experimental ingenuity.

Cowan and Reines were originally thinking of detecting the neutrinos from a nuclear explosion. Luckily, they concluded it is safer to use nuclear power plants as a more controlled source of neutrinos. They constructed a stack of large water tanks using protons in H_2O as the target medium. This pioneering detection method comprising water forms the basis of many important neutrino detectors at the Sudbury Neutrino Observatory, Kamiokande, and Homestake Experiments that would reveal neutrino oscillations. The detection of inverse beta decay occurs in two stages:

- The e^+ annihilates with an electron, producing a distinctive pair of back-to-back gamma rays. These are detected by a total of 100 photomultipliers surrounded each of the three tanks of water.

- The small central tanks of water are doped with cadmium chloride enables the neutron to be detected via ^{108}Cd capture. The resulting ^{108}Cd state is a metastable isotope that decays into a gamma ray

$$n + {}^{108}\text{Cd} \to {}^{109}\text{Cd}^* \to {}^{108}\text{Cd} + \gamma \tag{12.25}$$

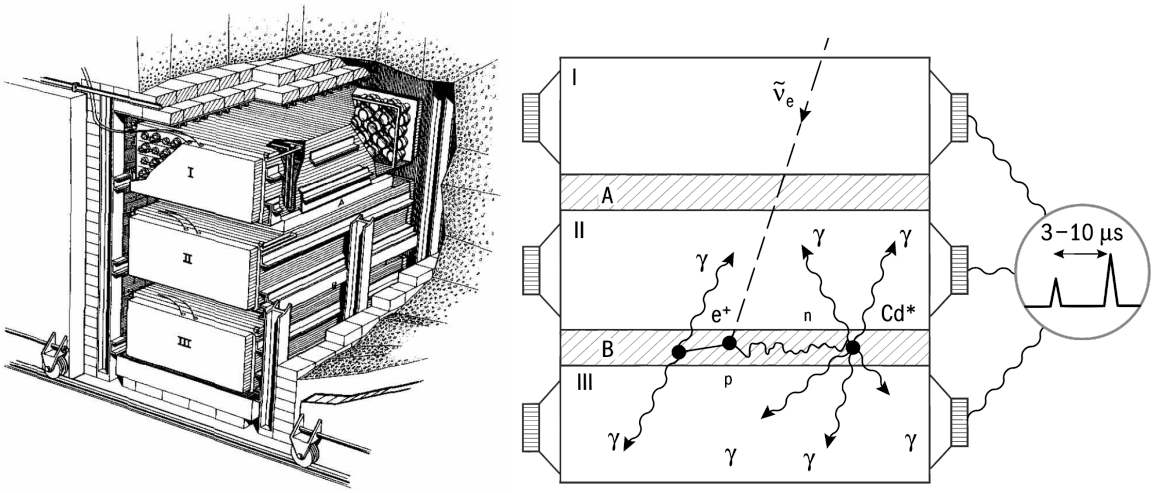

(a) Savannah River experiment

(b) Neutrino detection [82]

Figure 78: **Cowan–Reines neutrino detection experiment**. The experimental setup at Savannah River has three 1400-litre tanks of liquid scintillator (I, II, III) with 100 photomultipliers, and two tanks of Cadmium-doped water (A, B). Images: CERN Courier (July 2016)

> The neutron performs a random walk in the liquid before cadmium absorption resulting in a measurable three to ten microseconds delay. The coincidence of this signal with the first diphoton signature provided excellent signal discrimination.

They ran the experiment for 1371 hours in 1956. When the reactor was on, they detected 3.0 ± 0.2 neutrino candidates per hour. This experiment has the great benefit of having a reliable way to switch off the signal when the reactor is off to carefully determine the background rates. They also measured the neutrino-proton cross-section and found this to be compatible with estimates from Fermi theory:

$$\sigma_{\text{experiment}} = 12^{+7}_{-4} \times 10^{-44}\ \text{cm}^2, \tag{12.26}$$

$$\sigma_{\text{Fermi-theory}} = (5 \pm 1) \times 10^{-44}\ \text{cm}^2 \tag{12.27}$$

When they made this unambiguous detection, they sent a telegram to Pauli then at a conference in CERN[57]

> "We are happy to inform you that we have definitely detected neutrinos from fission fragments by observing inverse beta decay of protons. Observed cross

[57] See Reines' Nobel lecture https://www.nobelprize.org/uploads/2018/06/reines-lecture.pdf

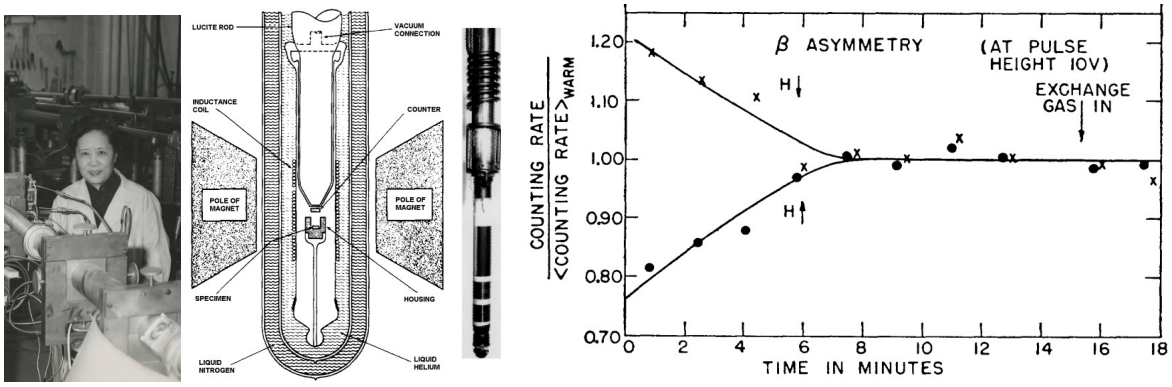

(a) C.-S. Wu (b) Co-60 experiment (c) Polarisation asymmetry vs warm-up time

Figure 79: **Wu et al. Cobalt-60 experiment**. The plot shows the beta asymmetry from the discovery paper [83], which illustrates the magnetic field polarisation up $H\uparrow$ and down $H\downarrow$ vs warm-up time of six minutes. Images: Smithsonian Institute Archives, National Institute of Standards and Technology, Ref. [83].

> section agrees well with expected six times ten to minus forty four square centimeters."

Pauli must have been thrilled to learn that the particle once thought to be undetectable had been discovered via direct means. Around 1986, his student C. P. Enz uncovered the response Pauli composed but Cowan and Reines never received:

> "Thanks for the message. Everything comes to him who knows how to wait."

12.3 Parity violation

The discovery of parity violation is a defining unexpected feature of the weak force uncovered in low-energy beta decays. We first study the famous Colbat-60 experiment led by Chien-Shiung Wu before turning to helicity suppression in pion decays. Electromagnetism, gravity, and the strong force all respect parity. The weak force remains the only fundamental force observed to do so. Why is nature like this? Why does the weak force not interact with right-handed states but only to left-handed ones? We do not know. This remains an open problem in physics.

As a quick review, the **parity operator** P maps coordinates $\mathbf{r} = (x, y, z)$ to its inverse $-\mathbf{r} = (-x, -y, -z)$ through the origin:

$$P\colon \mathbf{r} \mapsto -\mathbf{r} \tag{12.28}$$

Polar vectors $\mathbf{v}_{\text{po}}$, such as momentum $\mathbf{p}$ and electric field $\mathbf{E}$, acquire a negative sign. By contrast, **axial vectors** $\mathbf{v}_{\text{ax}}$, such as angular momentum $\mathbf{l} = \mathbf{r} \times \mathbf{p}$ and magnetic field $\mathbf{B}$, remain unchanged under parity transformations:

$$P\colon \mathbf{v}_{\text{po}} \mapsto -\mathbf{v}_{\text{po}} \tag{12.29}$$

$$P\colon \mathbf{v}_{\text{ax}} \mapsto \mathbf{v}_{\text{ax}} \tag{12.30}$$

The electromagnetic and strong interactions are invariant under parity transformations.

In 1956, Chien-Shiung Wu (figure 79a) led a team comprising Ernest Ambler, Raymond Hayward, Dale Hoppes, and Ralph Hudson at the National Bureau Standards to demonstrate parity violation in beta decay [83]. The cobolt-60 is cooled inside a cryogenic dewar shown in figure 79b. It involved aligning the nuclear magnetic moments of ^{60}Co to an external magnetic field at temperatures of 0.01 K. The ^{60}Co undergoes beta decay

$$^{60}\text{Co} \to {}^{60}\text{Ni}^{*} + e^{-} + \bar{\nu}_e \tag{12.31}$$

Under parity transformations, the nuclear magnetic moment $\boldsymbol{\mu}_n$, being axial, remains unchanged while the electron momentum $\mathbf{p}_e$, being polar, acquires a negative sign:

$$P : \boldsymbol{\mu}_n \mapsto \boldsymbol{\mu}_n, \qquad P : \mathbf{p}_e \mapsto -\mathbf{p}_e$$

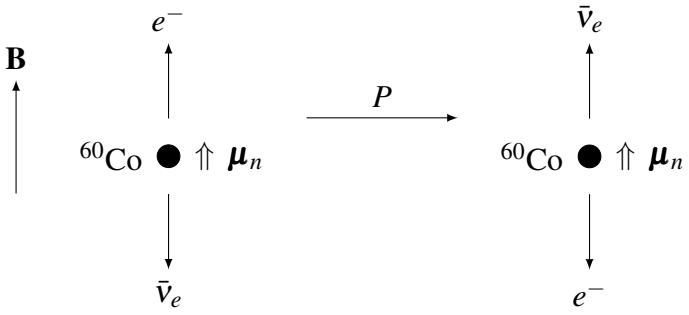

Performing a parity transformation on beta decay of ^{60}Co, the applied magnetic $\mathbf{B}$ field aligns the nuclear magnetic moment $\Uparrow \boldsymbol{\mu}$ in a fixed direction. The thin arrows indicate the linear momenta of the electron and antineutrino. If parity were conserved i.e. the parity transformation leaves the physics of the interaction invariant, we expect the detection rate of electrons in the $+\mathbf{B}$ hemisphere to be equal to that in the $-\mathbf{B}$ hemisphere.

However, the contrary is measured: the decay was preferentially emitting electrons in the $-\mathbf{B}$ direction (figure 79c). Therefore, this is empirical evidence that:

$$\boxed{\text{Weak interactions violate parity conservation.}} \tag{12.32}$$

Particle	Helicity h	Diagram	Handedness
ν	$-\frac{1}{2}$	$\xrightarrow{p}$ $\Leftarrow h$	left-handed
$\bar{\nu}$	$+\frac{1}{2}$	$\xrightarrow{p}$ $\Rightarrow h$	right-handed

Table 4: Observed helicities of neutrinos and antineutrinos.

Remarkably, the weak interactions violate parity symmetry not just by a little bit, but in a maximal way. The weak force appears all and nothing: left-handed (massless) particles feel the weak force, but right-handed particles do not at all. This is why you sometimes see subscript L by the SU(2) group describing the weak force: "$\mathrm{SU}(2)_\mathrm{L}$". We could imagine a universe where the weak force couples to left-handed particles 2.5% times stronger than right-handed particles and this effect would be much more subtle to observe. But this time, nature surprised us in the most striking manner.

Helicity suppression

Helicity h is the projection of the particle spin along the momentum. For ultrarelativistic particles $v \to c$, it is given by the operator

$$h = \frac{\mathbf{s}\cdot\mathbf{p}}{|\mathbf{p}|}, \qquad v \to c \tag{12.33}$$

where $\mathbf{s}$ and $\mathbf{p}$ are the spin and momentum vectors.

Under a parity transformation, helicity acquires a negative sign:

$$P : h \mapsto -h \tag{12.34}$$

Neutrinos are observed to violate parity conservation; their helicities are preferentially $h = +\frac{1}{2}$. Table 4 shows the following properties:

- Neutrinos are always 'left-handed' with helicity $h = -\frac{1}{2}$.
- Antineutrinos are always 'right-handed' with helicity $h = +\frac{1}{2}$.

This result generalises for other ultrarelativistic particles:

> For ultrarelativistic particles, charged current weak interactions only couple to **left-handed particles** and **right-handed antiparticles**. (12.35)

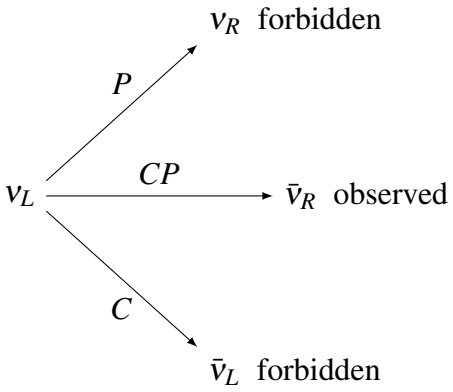

Figure 80: Neutrinos states after C, P and CP transformations.

This is an example of **charge-conjugation–parity conservation**, or **CP invariance**. Charge conjugation is the transformation that maps a particle to its antiparticle

$$C : a \mapsto \bar{a} \tag{12.36}$$

The following are illustrated in figure 80:

- Charge conjugation turns a left-handed neutrino into a left-handed antineutrino, which is not observed.
- Parity transformation turns a left-handed neutrino into a right-handed neutrino, which is not observed
- By performing charge conjugation and parity transformations, we turn a left-handed neutrino into a right-handed antineutrino, which is observed.

Pion decay helicity suppression

Published at the same time as the cobalt-60 experiment by Richard Garwin, Leon Lederman, and graduate student Marcel Weinrich using Columbia's Nevis Cyclotron Laboratory [84] about 20 up to Hudson river from Manhattan, where pions are created (figure 81a).

Consider a pion in its rest frame decaying into kinematically accessible leptons

$$\pi^+ \to \ell^+ + \nu_\ell, \qquad \ell = [e, \mu] \tag{12.37}$$

For e^+, we have $m_\pi \gg m_e$ so we work in the ultrarelativistic limit. By result (12.35), this means the electrons must be right-handed and the neutrino left-handed as depicted in figure 81 (a).

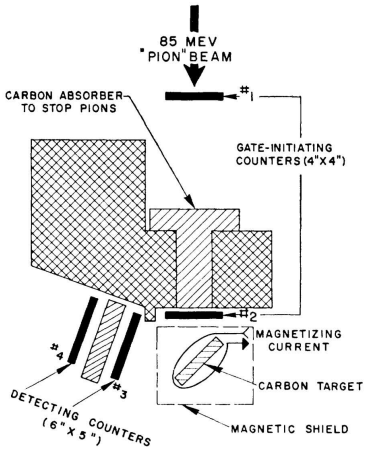

(a) Experimental setup [84]

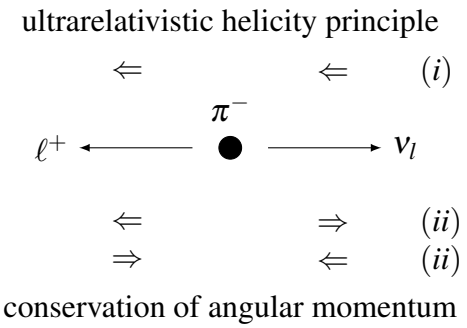

(b) Helicity of pion decay

Figure 81: The singly solid arrows denote linear momentum and double arrows denote spin. In the ultrarelativistic limit, we must have left-handed particles (neutrino) and right-handed antiparticles (antilepton) as depicted by (i) by principle 12.35. However a pion has spin-0. To conserve angular momentum, the spins of the antilepton and neutrino must be 'anti-aligned', as depicted in (ii) or (iii).

Now pions are spin-0 implying the spins of the positron and neutrino must be antialigned to conserve angular momentum. This means we have both particles must be either 'anti-aligned', as illustrated in figure 81 (b) or (c). So by demanding conservation of angular momentum, we violate the handedness principle (12.35) for charged weak interactions. Of course, the particles are not truly massless so decay into the electron type channel is not entirely forbidden. For decay involving muon flavoured leptons, these are of a similar mass to the pion and we are no longer in the ultrarelativistic limit. Pion decays to muons are not helicity suppressed.

Vector–axial (V-A) interaction

The implication of parity violation is that Fermi's theory of beta decay needs modifications. There are several ways to combine Dirac spinors in Lorentz covariant bilinears:

$$\bar{\psi}\psi \quad \text{scalar}, \tag{12.38}$$

$$\bar{\psi}\gamma^5\psi \quad \text{pseudo-scalar}, \tag{12.39}$$

$$\tfrac{1}{2}\bar{\psi}(\gamma^\mu\gamma^\nu - \gamma^\nu\gamma^\mu)\psi \quad \text{tensor}, \tag{12.40}$$

$$\bar{\psi}\gamma^\mu\psi \quad \text{vector}, \tag{12.41}$$

$$\bar{\psi}\gamma^\mu\gamma^5\psi \quad \text{axial-vector}. \tag{12.42}$$

The full electroweak interaction uses the vector and axial bilinears of Dirac spinors, which for beta decay looks like

$$\mathscr{M}_{fi} = \left[\bar{\psi}_p\gamma^\mu\frac{1-\gamma^5}{2}\psi_n\right]\frac{g_W}{\sqrt{2}}\left[\frac{\eta_{\mu\nu}}{q^2-m_W^2}\right]\frac{g_W}{\sqrt{2}}\left[\bar{\psi}_e\gamma^\nu\frac{1-\gamma^5}{2}\psi_\nu\right]. \tag{12.43}$$

We identify the charged current propagator $\eta_{\mu\nu}/(q^2-m_W^2)$ together with the weak vertex factors $g_W/\sqrt{2}$. Crucially, parity violation is explicitly encoded via the left-handed projection operators $P_L = \frac{1}{2}(1-\gamma^5)$ of the fermion currents. In the low-energy limit $q^2 \ll m_W^2$, we identify the prefactors with the Fermi constant

$$\frac{G_F}{\sqrt{2}} = \frac{g_W^2}{8m_W^2}. \tag{12.44}$$

12.4 Flavour mixing

We can extend the formulation of the weak interaction to quarks by claiming each generation of leptons and quarks have a one-to-one correspondence:

$$\begin{pmatrix}\nu_e\\ e^-\end{pmatrix} \to \begin{pmatrix}u\\ d\end{pmatrix} \quad \text{and} \quad \begin{pmatrix}\nu_\mu\\ \mu^-\end{pmatrix} \to \begin{pmatrix}c\\ s\end{pmatrix} \tag{12.45}$$

This is the *lepton–quark symmetry principle*, which asserts that quarks of the same generation have exactly the same coupling constant as the corresponding generations of leptons:

$$g_W = g_{ud} = g_{cs} \quad \text{[no flavour mixing]} \tag{12.46}$$

This works well for reactions as pion decay

$$\pi^+ \to \mu^+ + \nu_\mu \quad \Leftrightarrow \quad (d\bar{u}) \to \mu^+ + \nu_\mu \tag{12.47}$$

But this seems to preclude reactions when flavour changes involve crossing generations such as

$$K^+ \to \mu^+ + \nu_\mu \quad \Leftrightarrow \quad (s\bar{u}) \to \mu^+ + \nu_\mu \tag{12.48}$$

Cabibbo remedied this theoretical problem by introducing primed versions of d and s quarks, which are the actual ones interacting with the weak force:

$$\begin{pmatrix} u \\ d' \end{pmatrix} \quad \begin{pmatrix} c \\ s' \end{pmatrix}, \tag{12.49}$$

where d' and s' undergo weak interactions by linear superpositions given by

$$\begin{pmatrix} d' \\ s' \end{pmatrix} = \begin{pmatrix} \cos\theta_c & -\sin\theta_c \\ \sin\theta_c & \cos\theta_c \end{pmatrix} \begin{pmatrix} d \\ s \end{pmatrix}. \tag{12.50}$$

Here we introduce the **Cabibbo angle**, which has a measured value of $\theta_c \simeq 13^\circ \approx \pi/14$ or equivalently $\sin\theta_W \simeq 0.22$. We recognise the matrix has the form of a rotation and is known as the Cabibbo matrix. The unprimed d and s quarks are identified as mass eigenstates i.e. that feel the Higgs boson. The primed d' and s' quarks are identified as the gauge eigenstates i.e. that feel the W gauge boson. We can illustrate the effect of this by considering an up quark interacting via the W boson. The up quark can actually annihilate with the observed d' and s' quarks (in the mass basis) as a superposition of the underlying d and s quarks (in the flavour basis) by:

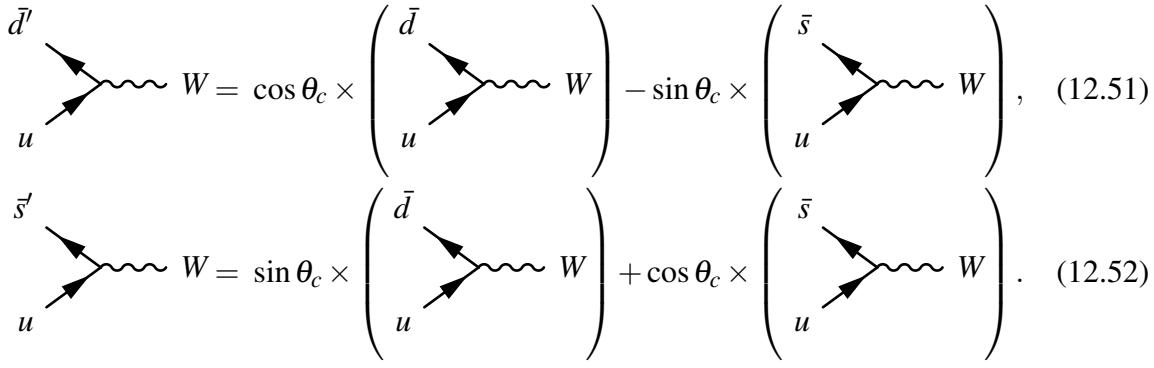

(12.51)

(12.52)

Accounting for this flavour mixing, we obtain the vertex factors

$$\begin{aligned} g_{ud} &= g_{cs} = g_W \cos\theta_c \\ g_{us} &= -g_{cd} = g_W \sin\theta_c \quad \text{[with flavour mixing]} \end{aligned} \tag{12.53}$$

So we interpret weak processes involving a change of generation in quark flavour have their coupling constants suppressed by a factor of $\sin\theta_c$. We shall see that this extends to the 3×3 Cabibbo–Kobayashi–Maskawa matrix in section 15.4.

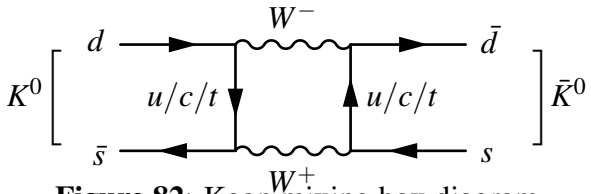

Figure 82: Kaon mixing box diagram.

12.5 Charge-parity violation in kaons

The evidence for broken charge-parity symmetry in nature was first observed in kaons. A consequence of quark mixing is that the neutral kaon $K^0 = d\bar{s}$ and its antiparticle $\bar{K}^0 = \bar{d}s$ can oscillate into each other via box diagrams (figure 82): The u quark can also be c and t but these are suppressed by the CKM matrix elements. These kaon oscillations were already first noticed by Gell-Mann and Abraham Pais in 1955 [85]. The Bettini textbook chapter 8 provides a lucid, more detailed account including kaon oscillations.

The kaons are pseudoscalars and have the transformation properties under parity P and charge conjugation C operations:

$$P|K^0\rangle = -|K^0\rangle, \quad C|K^0\rangle = |\bar{K}^0\rangle, \tag{12.54}$$

$$P|\bar{K}^0\rangle = -|\bar{K}^0\rangle, \quad C|\bar{K}^0\rangle = |K^0\rangle, \tag{12.55}$$

where charge conjugation swaps the quark charges $C|d\bar{s}\rangle = |\bar{d}s\rangle$. We can then construct eigenstates of CP operators:

$$|K_{\text{even}}\rangle = \frac{1}{\sqrt{2}}(|K^0\rangle - |\bar{K}^0\rangle), \quad CP \text{ even}, \tag{12.56}$$

$$|K_{\text{odd}}\rangle = \frac{1}{\sqrt{2}}(|K^0\rangle + |\bar{K}^0\rangle), \quad CP \text{ odd}. \tag{12.57}$$

We call these the CP-even ($CP|K_{\text{even}}\rangle = |K_{\text{even}}\rangle$) and CP-odd ($CP|K_{\text{odd}}\rangle = -|K_{\text{odd}}\rangle$) eigenstates, which you can verify by directly applying (12.55). To respect CP symmetry, there should be two different decays distinguished by their pion decay multiplicity:

$$K_{\text{even}} \to \pi\pi, \quad \text{CP even} \tag{12.58}$$

$$K_{\text{odd}} \to \pi\pi\pi, \quad \text{CP odd}. \tag{12.59}$$

To work out the CP transformation of decaying pions, we consider the operations of charge conjugation combined with intrinsic and orbital parity:

$$CP = C \times P_{\text{intrinsic}} \times P_{\text{orbital}}. \tag{12.60}$$

Stepping through the two and three pion decays separately:

- **Two-pion systems are CP even**: $CP|\pi\pi\rangle = +|\pi\pi\rangle$.

  We first see each pion is a pseudoscalar so has intrinsic parity -1, so a pair of pions has even parity

  $$P_{\text{intrinsic}}(\pi\pi) = (-1)^2 = +1. \tag{12.61}$$

  The two pions decay from a spin-zero kaon so the orbital angular momentum is $L = 0$, giving a total parity of

  $$P_{\text{orbital}}(\pi\pi) = (-1)^L = +1. \tag{12.62}$$

  We then consider C for the neutral and charged pairs separately:

  – *Neutral pair* $|\pi^0\pi^0\rangle$: neutral pions comprise a superposition of same-flavour quarks $|\pi^0\rangle = \frac{1}{\sqrt{2}}(|u\bar{u}\rangle - |d\bar{d}\rangle)$, so are individually even under the charge conjugation $C = +1$. The pair of neutral pions then has

  $$C(\pi^0\pi^0) = +1. \tag{12.63}$$

  Therefore, $|\pi^0\pi^0\rangle$ is CP-even.

  – *Charged pair* $|\pi^+\pi^-\rangle$: charge conjugation is equivalent to swapping their spatial positions, which is the same as a parity operation $C|\pi^+\pi^-\rangle = |\pi^-\pi^+\rangle = P|\pi^+\pi^-\rangle = (-1)^L$. Given $L = 0$, we find

  $$C(\pi^+\pi^-) = +1. \tag{12.64}$$

  Therefore, $|\pi^+\pi^-\rangle$ is also CP-even.

- **Three-pion systems are CP odd**: $CP|\pi\pi\pi\rangle = -|\pi\pi\pi\rangle$.

  The intrinsic parity of three pions is odd

  $$P_{\text{intrinsic}}(\pi\pi\pi) = (-1)^3 = -1. \tag{12.65}$$

  We now consider P_{orbital} and C separately for the cases with and without charged pions:

  – *Neutral triplet* $|\pi^0\pi^0\pi^0\rangle$. This is even under charge conjugation

  $$C(\pi^0\pi^0\pi^0) = (+1)^3 = +1. \tag{12.66}$$

  For orbital angular momentum, there are two independent axes: L_1 for the first pair orbiting each other, and L_2 for the third pion orbiting the first pair. So the orbital parity is $P_{\text{orbital}}(\pi^0\pi^0\pi^0) = (-1)^{L_1} \times (-1)^{L_2}$. Angular momentum sums

according to the usual rules of quantum-mechanical addition $|L_1+L_2|, |L_1+L_2-1|, \ldots |L_1-L_2|$. This can only include the spin-zero of the initial kaon if $L_1 = L_2$, implying orbital parity is always even

$$P_{\text{orbital}}(\pi^0\pi^0\pi^0) = (-1)^{2L_1} = +1. \tag{12.67}$$

Therefore, $|\pi^0\pi^0\pi^0\rangle$ is CP-odd.

– *Charged triplet* $|\pi^+\pi^-\pi^0\rangle$. Like the $|\pi^0\pi^0\pi^0\rangle$ case, the total orbital angular momentum being zero again constrains $L_1 = L_2$ such that orbital parity is even

$$P_{\text{orbital}}(\pi^+\pi^-\pi^0) = (-1)^{2L_1} = +1. \tag{12.68}$$

Charge conjugation of π^0 is still even but the charged pair is now more subtle. We still have $C(\pi^+\pi^-) = P(\pi^+\pi^-) = (-1)^{L_1}$ but unlike the two-pion case (12.64), L_1 is now no longer fully constrained to be zero. Nonetheless, we can invoke kinematic arguments. The three-pion system has very little phase space because of the small mass difference $m(K^0) - 2m(\pi^\pm) - m(\pi^0) \approx 498 - 2\times 139.6 - 135 \approx 83$ MeV. The $L_1 = 1$ case is therefore highly suppressed because the three pions must share the low kinetic energy and requires significant impact parameter. Therefore, the zero orbital angular momentum state $L_1 = 0$ dominates. This leads to the charge conjugation to be even

$$C(\pi^+\pi^-\pi^0) = P(\pi^+\pi^-)\times C(\pi^0) \simeq (-1)^{L=0}\times(+1) = +1. \tag{12.69}$$

Therefore, the combined $|\pi^+\pi^-\pi^0\rangle$ state is well approximated to be CP-odd.

The two states K_{even} and K_{odd} mix into two experimentally distinct states distinguishable by their lifetimes. We call the observed mass eigenstates of neutral kaons "K-short" K^0_{short} and "K-long" K^0_{long}. Their decay lifetimes differ strikingly by three orders of magnitude due to phase space differences Δm:

$$K^0_{\text{short}} \to \pi\pi, \quad \Delta m(K, 2\pi) \approx 220 \text{ MeV}, \quad \tau_{\text{rest}}(K^0_{\text{short}}) \approx 9\times 10^{-11} \text{ s}, \tag{12.70}$$

$$K^0_{\text{long}} \to \pi\pi\pi, \quad \Delta m(K, 3\pi) \approx 90 \text{ MeV}, \quad \tau_{\text{rest}}(K^0_{\text{long}}) \approx 5\times 10^{-8} \text{ s}. \tag{12.71}$$

If nature respected CP, the observed mass eigenstates would equal these CP eigenstates distinguished by pion multiplicity:

$$K^0_{\text{short}} = K_{\text{even}}, \quad K^0_{\text{long}} = K_{\text{odd}}, \quad \text{CP conservation condition.} \tag{12.72}$$

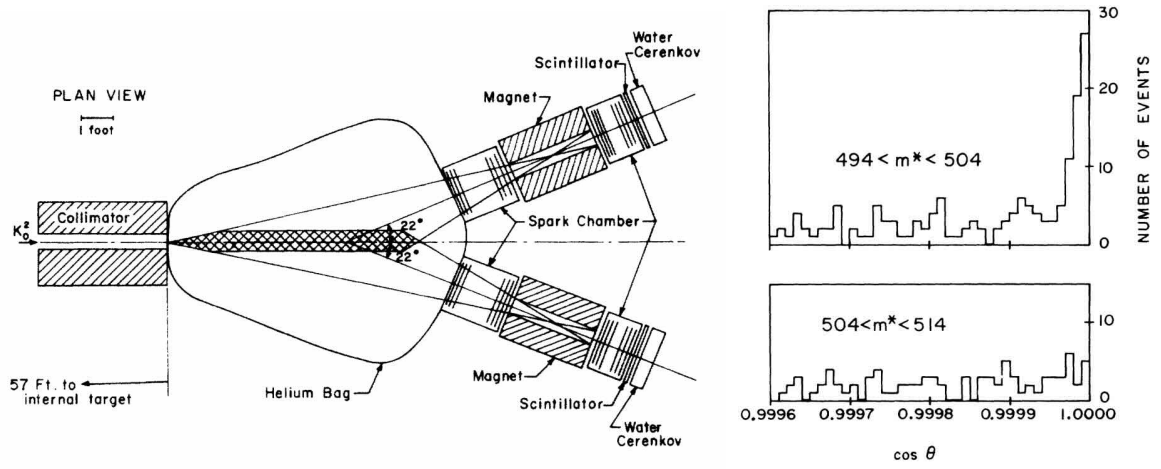

(a) Experimental apparatus (b) Di-pion system

Figure 83: **Experiment discovering kaon CP violation**. Note K_0^2 is what we call the K_{long}. The plot shows the pion invariant mass distributions at high scattering angle $\cos\theta > 0.9995$ inside for signal (upper) and above (lower) the kaon mass to estimate background; the peak shows the two pions originate from a kaon. Diagrams from Ref. [86].

To test this hypothesis, J. Christenson, James Cronin, Val Fitch, and Rene Turlay constructed an experiment at the Brookhaven Alternating Gradient Synchrotron (AGS) in 1964 [86]. Protons accelerated to 30 GeV bombard a Be target, and a resulting beam of neutral kaons enter an 18 m decay chamber. For relativistic kaons with energy greater than a few GeV, the decay length $c\tau_{\text{rest}}$ for K^0_{short} and K^0_{long} is 2.7 cm and 15.6 m, respectively, so nearly all the short-lived K^0_{short} states decay. The exiting beam is then highly pure in K^0_{long}, so they could observe if K^0_{long} indeed decayed to three pions and thus respected CP conservation.

Instead, they produced a high-statistics K^0_{long} sample and counted a significant number of two-pion decays:

$$\frac{N(K^0_{\text{long}} \to \pi^0\pi^0) + N(K^0_{\text{long}} \to \pi^+\pi^-)}{N(K^0_{\text{long}} \to \text{all decays})} = \frac{45}{22\,700} \neq 0. \tag{12.73}$$

Therefore, CP symmetry is not conserved in weak decays. Historically, this was an utterly shocking discovery. This 0.2% deviation from the CP conservation condition (12.72), $K^0_{\text{short}} \neq K_{\text{even}}, K^0_{\text{long}} \neq K_{\text{odd}}$, identifies the mass eigenstates as a small ε superposition of the

CP-violating contribution:

$$|K^0_{\text{short}}\rangle = \frac{1}{\sqrt{1+\varepsilon^2}}(|K^0_{\text{even}}\rangle - \varepsilon|K^0_{\text{odd}}\rangle), \tag{12.74}$$

$$|K^0_{\text{long}}\rangle = \frac{1}{\sqrt{1+\varepsilon^2}}(|K^0_{\text{even}}\rangle + \varepsilon|K^0_{\text{odd}}\rangle), \tag{12.75}$$

with $\varepsilon \approx 2 \times 10^{-3} \neq 0$ measured. While this effect is at a subtle per-mille level in the neutral kaon system, an analogous but larger effect is also observed in B-mesons. While it is far from obvious from these first observations, the existence of CP violation in the quark sector requires there to be at least three generations of quarks. We shall see the modern prescription of CP violation in the quark sector arising from one complex phase in the Cabibbo–Maskawa–Kobayashi matrix in section 15.4.

13 City-sized collider experiments

Unveiling the dynamics at the electroweak scale requires constructing colliders the size of cities and detectors the size of cathedrals. The reason we require such powerful machines to explore this sector is because of high energies required to probe the large $\mathcal{O}(100\ \text{GeV})$ mass scales and intense beam luminosities to probe the comparatively rare event rates of electroweak interactions.

13.1 High energy accelerators

Table 5 shows some notable particle colliders. The Large Electron Positron Collider and Large Hadron Collider (LHC) are the largest synchrotons constructed to date, with a circumference of 27 km (figure 84). That is around the length of the Circle Line of the London Tube underground train system, which surrounds inner London. The tunnels house the magnets that steer the beams around the ring and into each other at the interaction points (figure 85). The LHC has and operates up to a centre-of-mass energy of $\sqrt{s} = 13.6$ TeV, and is set for upgrades to the High-Luminosity LHC in 2026.

Collider	Lab	Beams	$\sqrt{s_{\text{max}}}$	Operational	Length	Experiments
PETRA	DESY	e^-e^+	46 GeV	1978–1986	2.3 km	JADE, MARK-J, PLUTO, TASSO
SLC	SLAC	e^-e^+	100 GeV	1989–1998	3.2 km	SLD
LEP	CERN	e^-e^+	209 GeV	1989–2000	27 km	ALEPH, DELPHI, L3, OPAL
HERA	DESY	e^-p	320 GeV	1992–2007	6.3 km	H1, HERMES, HERA-B, ZEUS
SppS	CERN	$p\bar{p}$	400 GeV	1981–1991	6.9 km	UA1, UA2
Tevatron	FNAL	$p\bar{p}$	1.96 TeV	1983–2011	6.3 km	CDF, DZero
LHC	CERN	pp	13.6 TeV	2008–2026	27 km	ALICE, ATLAS, CMS, LHCb

Table 5: **Notable high-energy particle colliders**. The full names are: Positron–Electron Tandem Ring Accelerator (PETRA), Stanford Linear Collider (SLC), Large Electron Positron Collider (LEP), Hadron–Electron Ring Accelerator (HERA), Super Proton–Antiproton Synchrotron (SppS), Large Hadron Collider (LHC).

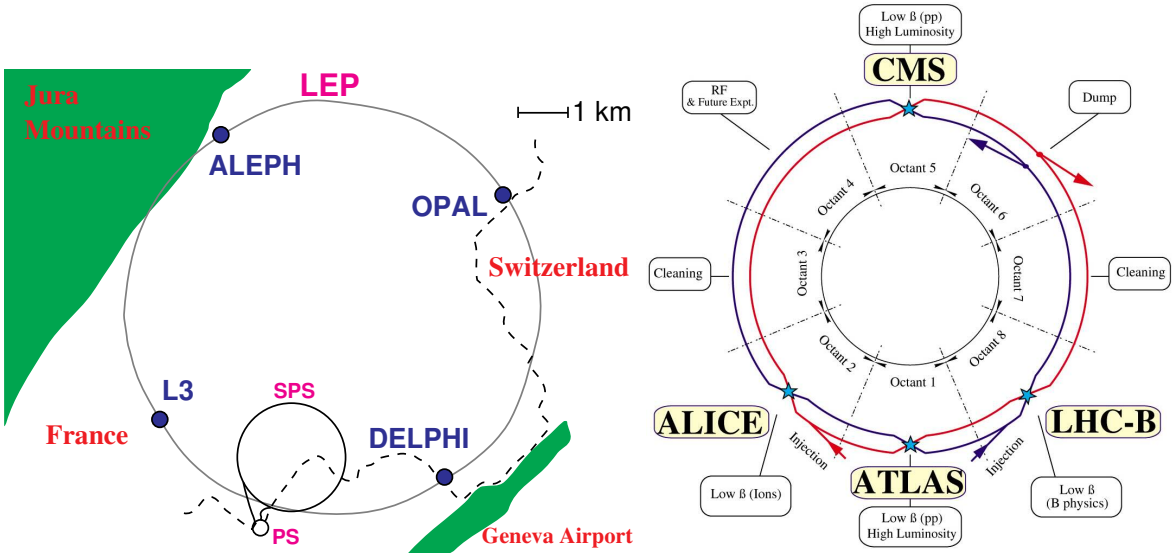

(a) Large Electron Positron Collider (b) Large Hadron Collider

Figure 84: **LEP and LHC layout at CERN**. Layout of the largest synchrotron constructed to date at 27 km circumference located at Geneva, Switzerland. Displayed are the Large Electron Positron (LEP) Collider, which was superseded by the Large Hadron Collider. Each collider has four interaction points where collisions occur and experiments are installed. The Proton Synchrotron (PS) and Super Proton Synchrotron (SPS) serve as lower-energy beam injectors into LEP and the LHC. Figures from Refs. [87, 88].

The Barr et. al. *Particle Physics in the LHC Era* textbook [1] unsurprisingly provides excellent detailed coverage of experimental aspects of collider physics, which we summarise in this section. We focus on the LHC and ATLAS as concrete examples of contemporary experiments, but the principles they illustrate readily generalise to other operational particle physics experiments.

13.2 Particle interactions with matter

We detect a particle via its interactions with matter. Detectors are thus built to fully exploit these known behaviours.

Ionisation Charged particles can liberate electrons from atoms, creating positive ions and free electrons while the incident particle loses energy. The rate of ionisation depends on the velocity $\beta\gamma$ of incident particles of charge z traversing through a material with mass density ρ, atomic number Z and atomic mass A. In 1930, Hans Bethe derived the mean rate of energy

(a) CERN LHC aerial view [89]

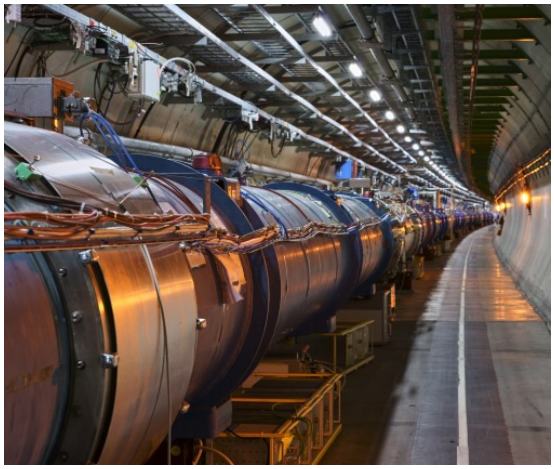

(b) LHC tunnel [90]

Figure 85: **CERN aerial view of LHC**. Photo from 2008 and tunnel of the Large Hadron Collider (LHC), which also housed the Large Electron Positron (LEP) Collider. The city of Geneva, Switzerland alongside the Alps mountain range are visible in the background.

loss per unit length $\langle \mathrm{d}E/\mathrm{d}x \rangle$ [MeV cm^{-1}] of the incident charged particle on material[58]:

$$\left\langle \frac{\mathrm{d}E}{\mathrm{d}x} \right\rangle \approx \underbrace{\left(\rho \frac{Z}{A}\right)}_{\text{target}} \left(4\pi N_A r_e^2 m_e\right) \frac{z^2}{\beta} \left[\ln\left(\frac{2m_e(\beta\gamma)^2}{I_e} \right) - \beta^2 \right]. \tag{13.1}$$

The only terms that depend on the target material properties are $\rho Z/A$, along with the effective ionisation potential I_e averaged over the electrons for the materials' atoms, given approximately by $I_e \approx 10 \cdot Z$ eV. The linear Z/A dependence is crucial for selecting materials as we want to increase the material's atomic charge Z to mass number A ratio for increased $\mathrm{d}E/\mathrm{d}x$ energy loss rate. The other proportionality constants are Avogadro's number N_A, electron mass m_e, and what is called the *classical electron radius* r_e given by

$$r_e = \frac{e^2}{4\pi\varepsilon_0 m_e c^2}. \tag{13.2}$$

Figure 86 shows this for a single charged particle traversing through liquid hydrogen, helium gas, carbon, aluminium, iron, tin, and lead. Using $\beta\gamma = \frac{p}{mc}$, we can translate the horizontal axis into the muon, pion, and proton momentum. Ionisation is strongest for low particle velocity, shown by the sharp rise at low $\beta\gamma$ and a flatter $\mathrm{d}E/\mathrm{d}x$ at high $\beta\gamma$. There is a broad minimum at around $\beta\gamma \approx 3$, and particles with such values are called **minimum**

[58] This is often called the Bethe or Bethe–Bloch formula.

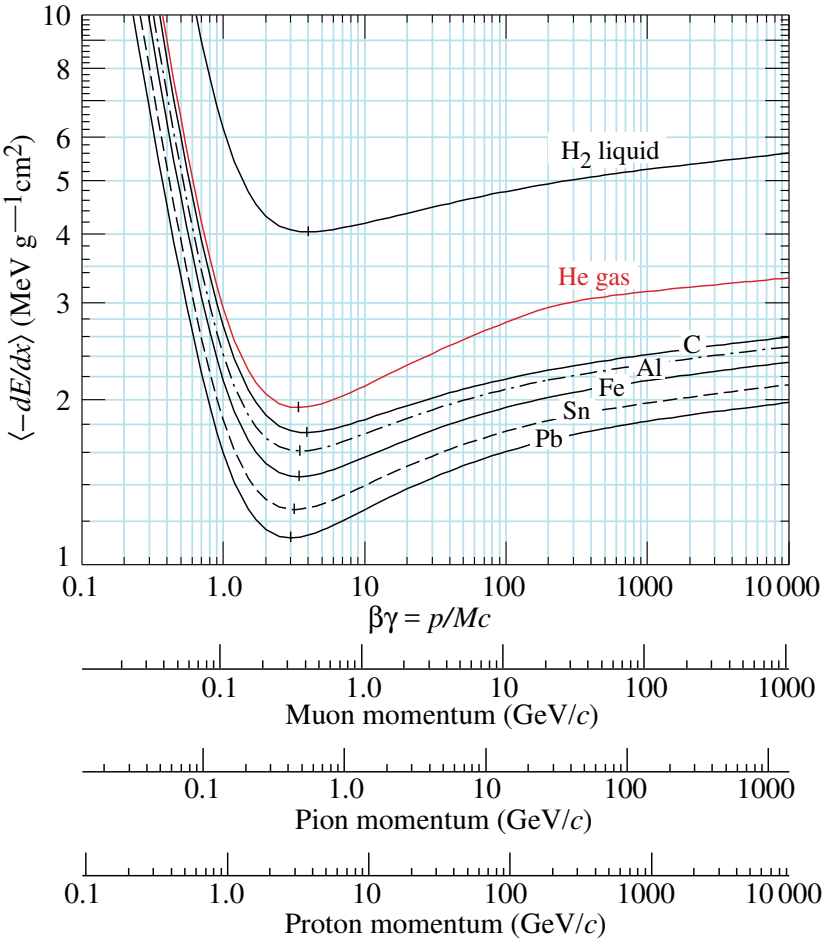

Figure 86: **Particle stopping power by material**. Stopping power $\mathrm{d}E/\mathrm{d}x$ for muon and by material from Ref. [75].

ionising particles (MIPs), which often applies to muons at colliders. At low $\beta\gamma$, the energy loss is dominated by the logarithm term and the large electromagnetic cross-section relative to the atom's ionization energy I_e. At relativistic energies, incident particles can interact with atoms deeper into the material.

Bremmstrahlung The Bethe–Bloch formula (13.1) applies to electrons and positrons at low energies. But above a critical energy E_c, the energy loss is dominated by bremsstrahlung "braking radiation", whereby the incident electron radiates a photon when bending around an atomic nucleus. This is approximately inversely proportional to the atomic number

$$E_c \approx \frac{800\ \mathrm{MeV}}{Z}. \tag{13.3}$$

At the LHC, electrons typically carry GeV-scale energies so bremsstrahlung energy losses dominate. Bremsstrahlung occurs for all charged particles but is most notable for electrons because energy loss is inversely proportional to the particle mass squared, so is a factor of $(m_e/m_\mu)^2 \approx 0.005$ rarer for muons.

When photons are radiated off, these photons can also interact electromagnetically. For energies $E_\gamma \gtrsim 1$ MeV, Compton scattering $\gamma e^- \to \gamma e^-$ becomes significant. When photon energies reach $E_\gamma \gtrsim 10$ MeV, pair creation dominates, where the photon scatters off a nucleus to undergo pair creation $\gamma N \to e^+ e^- N$.

These electron/positron/photon interactions create an **electromagnetic shower** characterised by a **radiation length** X_0. The rate of energy lost by per unit length is given by

$$\frac{\mathrm{d}E}{\mathrm{d}x} = -\frac{E}{X_0}, \quad \Rightarrow \quad E(x) = E_{\text{initial}} \mathrm{e}^{-x/X_0}. \tag{13.4}$$

The most salient features of X_0 are captured in an approximate expression

$$\frac{1}{X_0} \approx 4\alpha_{\text{EM}} n Z^2 r_e^2 \ln\left(\frac{287}{\sqrt{Z}}\right), \tag{13.5}$$

where n is the nuclei number density. Crucially, we see dependence Z^2 dependence allows short radiation lengths using high atomic number materials. Example radiation lengths for heavy materials are $X_0(\text{iron}) = 1.76$ cm and $X_0(\text{lead}) = 0.56$ cm.

13.3 Detectors for terascale physics

Detectors like ATLAS and CMS (figure 87) at the LHC contains many layers with various functions (figure 91). They typically comprise an cylindrical geometry with onion-like structures from inside to outside: (i) precision trackers with high spatial resolution surrounding the interaction point, (ii) electromagnetic (ECal) and hadronic (HCal) calorimeters for energy measurement, (iii) muon systems on the outside.

Trackers for charged-particle measurements

These measure the charge and sample the positions where charged particles pass allowing a track to be reconstructed. Bathed in a uniform magnetic field, this reconstructs the paths of muons, electrons and hadrons. More specifically, the charge to momentum ratio q/p of charged particles, whose radius of curvature $r \propto B(q/p)$ in a magnetic field strength of B. It is made from silicon pixels with strips surrounding it, designed to withstand large doses of radiation. It has a resolution of around 10μm. Long-lived particles such as B-mesons

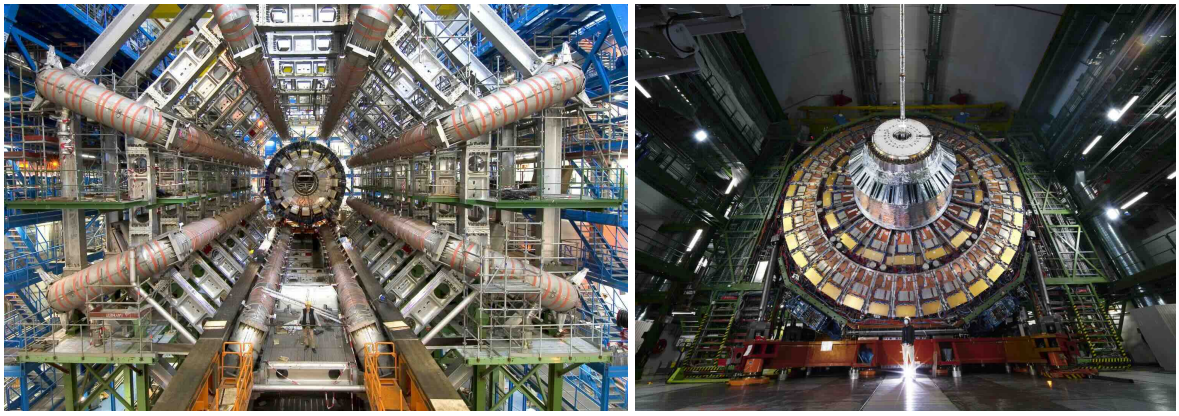

(a) ATLAS detector (b) CMS detector

Figure 87: **Photos of ATLAS and CMS detectors**. Roger Ruber is pictured standing at the bottom of the famous ATLAS photo. Images: CERN-EX-0511013 , CERN-PHOTO-202108-102.

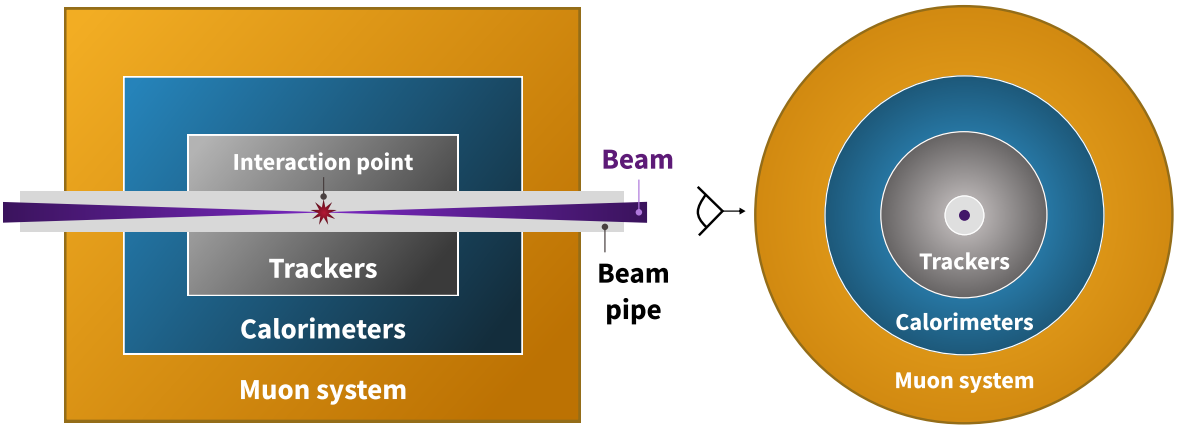

Figure 88: **Schematic of general collider detector**. The layout shows the beam interaction point, comprising the beam pipe, trackers, calorimeters, and muon chambers. The hadronic calorimeter (HCal) surrounds the electromagnetic calorimeter (ECal). Right shows the cross-section looking down the beam pipe.

containing b quarks have rest lifetimes around $\tau(B) \approx 10^{-12}$ s, leading to a finite measurable distance $c\tau(B) \approx 3 \times 10^{8}$ m s$^{-1} \times 10^{-12}$ s ≈ 0.3 mm, which increases with boost $\gamma c\tau$. So a tracker with spatial resolution of $\mathcal{O}(10\ \mu\text{m})$ can resolve the displaced tracks as the B-meson decays to tag the object as originating from a b quark.

The general principle of tracking is to measure the charge and positions of where the particles passed. This allows deduction charge to momentum ratio and radius of curvature.

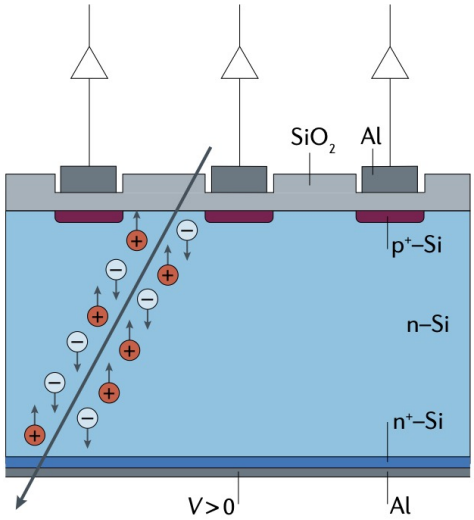

Figure 89: **Silicon sensor schematic**. This showing the principle of detection from Ref. [91].

Ideally, the tracking minimises the interactions with the charged particles it is trying to reconstruct. This allows for accurate energy momentum measurement in the calorimeter. This is primarily done through:

- **Semiconductor trackers**. Silicon can be doped to create p-n junctions (figure 89), the former with a deficit and latter with a surplus of electrons. Passing charged particles ionise the semiconductor, leaving electron–hole pairs in its path. A large reverse-bias potential difference is applied, and the holes drift with the induced electric field. These are collected at p–n junctions where an electrical signal is measured so the charge and position of the particle is determined. Two varieties of silicon trackers are used: strips and pixel detectors. Silicon strips are separated by order $\sim 25\,\mu$m while pixels give a precise position in 2 dimensional space. These can furthermore provide sensitivity to secondary vertices from delayed decays of b hadrons.

- **Gas/wire drift chambers** . This comprises array of wires, each filled with a gas such as argon-ethane. Charged particles ionise the gas and the electrons liberated from the atoms drift towards a positive anode. This is converted to an electrical signal, which is used to determine the charge of the particle and its position.

- **Muon chambers**. These are essentially large-scale tracking detectors that surround the exterior of the calorimeters. They are typically gaseous detectors, given they are more cost-effective than solid-state technology for the large required surface areas. Essentially a heavier version of the electron, muons do not interact strongly with the inner

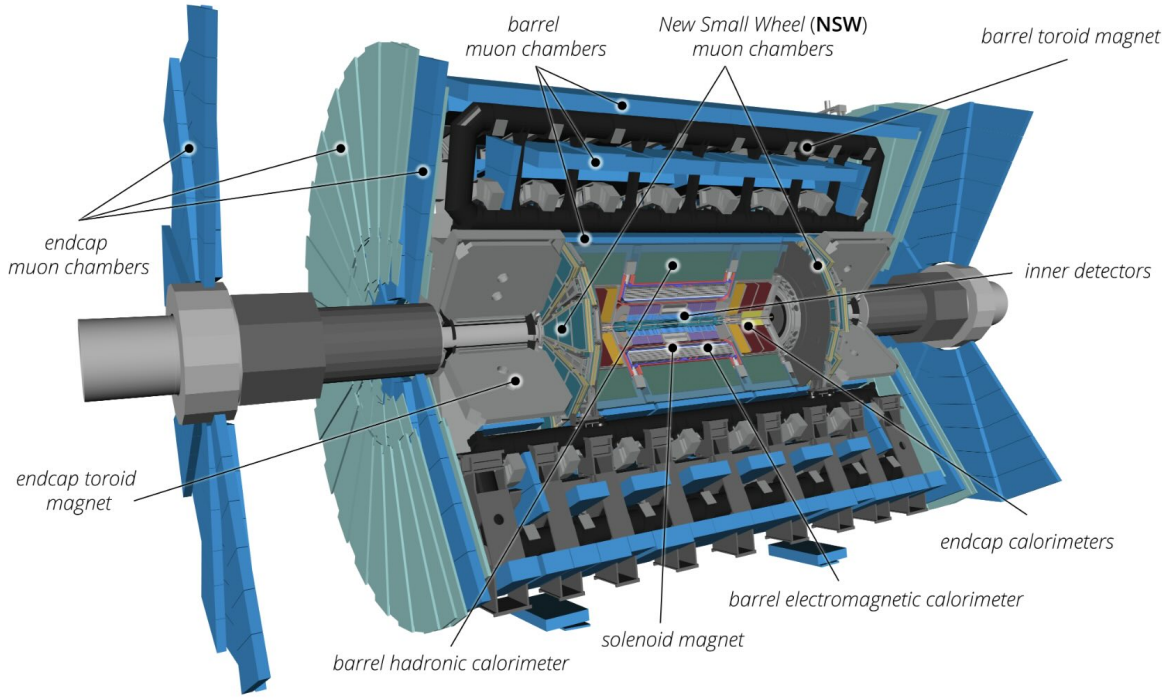

Figure 90: **ATLAS Experiment layout**. The components exemplifies a modern collider detector from Ref. [92].

calorimeters. Powerful magnets bend the muons allowing momentum measurement upon matching with trackers. New long-lived charged particles beyond the Standard Model could show up as an excess against these muons.

Calorimeters for energy measurement

These measure the kinematics of electrons and photons. These are made from crystals or liquid argon that scintillate when electrons or photons pass through. Light is emitted proportional to the particle's energy, which is converted to an electric signal for amplification.

Electromagnetic calorimeters use heavy high Z materials to stop and measure the energies of electrons and photons. In the CMS detector, they use an inorganic scintillator made of lead tungstate ($PbWO_4$) crystals, arranging 75,000 of them into a dense array. These are optically transparent and owing to a short stopping length of $X_0 = 0.83$ cm, the electromagnetic showers are contained within a compact space. Photon detectors amplify the scintillation light, which is proportional to the total energy of the incoming electron or photon. The

typical energy resolution is of the order of percent:

$$\frac{\sigma_E}{E} \sim \frac{3\% - 10\%}{\sqrt{E/\mathrm{GeV}}}. \tag{13.6}$$

Hadronic calorimeters measure kinematics of the strongly interacting hadrons, made of quarks and gluons that are emitted in collisions. Hadrons interact with dense absorbers which trigger showers into a cascade of further particles. There is also scintillators that fluoresce, whose signal is amplified by photodetectors. Many models of supersymmetry have supersymmetric particles that are coloured and hence hadronise. The comparatively larger internuclear distance of traversing hadrons usually means this calorimeter to be much larger than the electromagnetic calorimeter. A sandwich formation is typically employed: the hadronic showers develop in thick layers of highly dense absorbers, while the energies of the charged particles are measured in thinner layers of active material. The ATLAS experiment contains alternating layers of steel absorbers and plastic scintillator tiles. We then sum the signals arising from the different layers is then summed to give the total energy of the hadronic activity. Hadronic calorimeters typically have order of magnitude coarser energy resolution relative to the electromagnetic counterpart

$$\frac{\sigma_E}{E} \gtrsim \frac{50\%}{\sqrt{E/\mathrm{GeV}}}. \tag{13.7}$$

Triggering

The LHC has an operational energy of 13.6 TeV and luminosity of $10^{34}\,\mathrm{cm}^{-2}\,\mathrm{s}^{-1}$ and typical total cross-sections of 10^8 nb. The bunch spacing is 25 ns, which translates into a collision rate at the LHC is 40 MHz. Storing all events is therefore practically impossible. Modern collider experiments therefore employ a **trigger** to rapidly decide which interesting events to store permanently. In the end, only $1/40\,000$ events that occurred are actually stored for analysis. With such a high rejection ratio, it is important to understand what new physics signatures could look like in hadronic collisions. Even after this enormous rejection, the LHC records some $\approx 10^{16}$ bytes (15 000 terabytes) per year. ATLAS and CMS use a two-level trigger system:

- **First-level hardware trigger ("Level-1, L1")**: 40 MHz $\rightarrow$ 100 kHz event rate. Hardware processors seek high momentum signatures e.g. large p_T leptons and have lower resolution information from the calorimeter or muon systems to relay this to the counting room extremely quickly. The hardware trigger is fast, taking at most 2.5 microseconds to perform calculations about the event. The price for this speed is that it requires

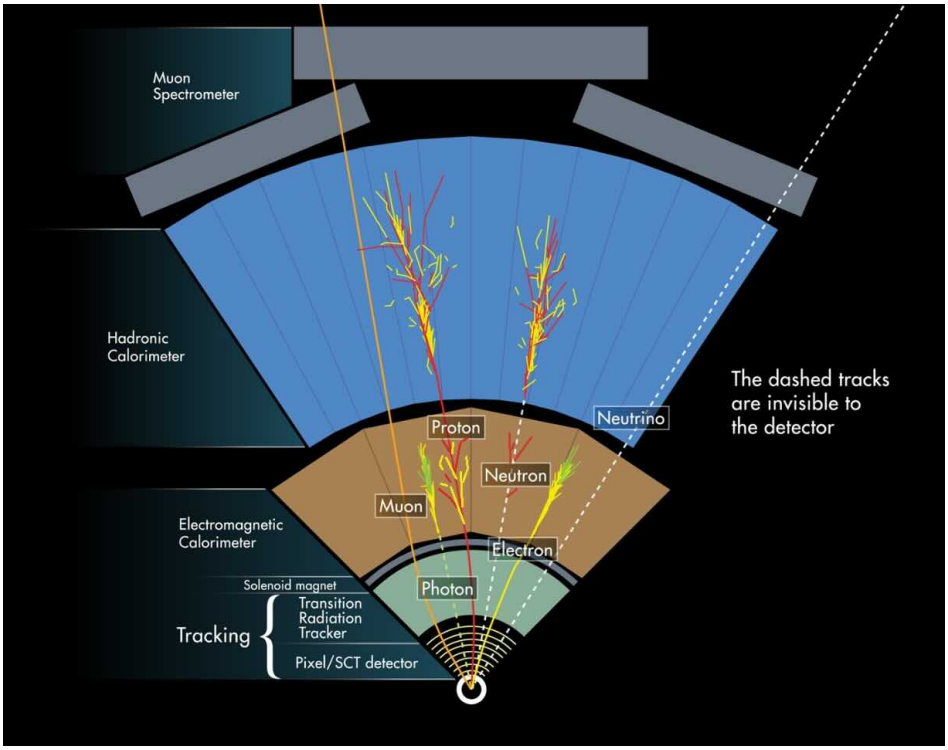

Figure 91: Particles traversing through the various subsystems of the ATLAS detector [93].

lower-level firmware programming and the event information is coarser than the software trigger.

- **Second-level software trigger ("High-level, HLT")**: 100 kHz $\rightarrow$ 1 kHz event rate. The HLT uses a large farm of 40,000 CPU cores with more configurable software code than the L1 trigger. This can utilise event information and perform basic particle reconstruction from the whole detector with higher granularity than the L1 trigger. This selects around 1000 events per second to be recorded permanently.

The trigger's primary objective is to determine if objects are *above threshold* e.g. if an electron is $p_{\mathrm{T}} > 25$ GeV rather than measuring with high precision. Events that fail to pass a trigger will never be recorded, so it is important to keep triggers as loose as possible.

13.4 Collider kinematics

At hadron colliders, the beam centre-of-mass frame does not usually coincide with the centre-of-mass frame of the interaction because protons are not fundamental particles. Only the energy and momentum $(E, \mathbf{p})$ **transverse** to the beam direction can be reliably measured. Fur-

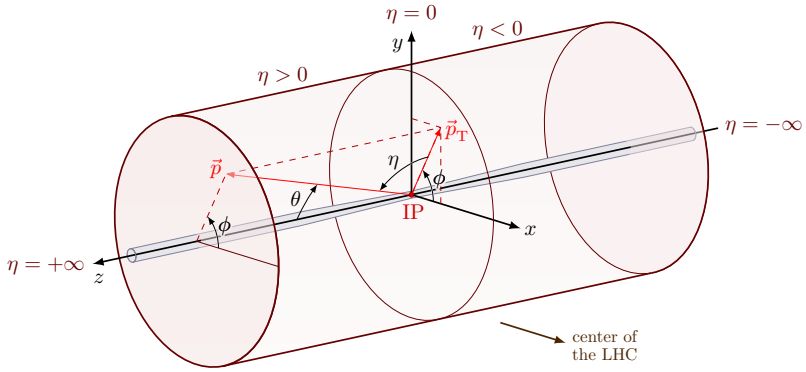

Figure 92: LHC detector coordinate system from Izaak Neutelings.

thermore, the cylindrical nature of collider detectors make cylindrical coordinates (p_T, θ, ϕ) more natural (figure 92), where θ and ϕ are the usual polar and azimuthal angles of a right-handed coordinate system. So conventionally the x direction is towards the centre of the LHC and y is towards the sky. The transverse three-momentum

$$p_{\mathrm{T}} = |\mathbf{p}| \sin\theta \tag{13.8}$$

is indeed Lorentz invariant under longitudinal boosts and has an intuitive interpretation. We can *define* the transverse energy associated with this transverse momentum

$$E_{\mathrm{T}} = E \sin\theta \tag{13.9}$$

along with the **transverse mass**

$$m_{\mathrm{T}} = \sqrt{E_{\mathrm{T}}^2 - p_{\mathrm{T}}^2}. \tag{13.10}$$

(Pseudo-)rapidity Now the polar angle θ is not boost invariant in the longitudinal direction. The reason we use the rapidity is that it is Lorentz invariant under longitudinal boosts, unlike the polar angle θ. We can define the **rapidity** y of a particle with energy E and longitudinal momentum p_z to be

$$y = \frac{1}{2} \log\left(\frac{E + p_z}{E - p_z}\right) = \tanh^{-1}\left(\frac{p_z}{E}\right). \tag{13.11}$$

For ultrarelativistic or massless particles, the rapidity limits to a quantity called the **pseudo-rapidity** η, which is still a (longitudinally) boost invariant parametrisation of the polar angle θ

$$\eta \equiv \frac{1}{2} \ln\left(\frac{1 + \cos\theta}{1 - \cos\theta}\right) = \ln\left(\cot\frac{\theta}{2}\right). \tag{13.12}$$

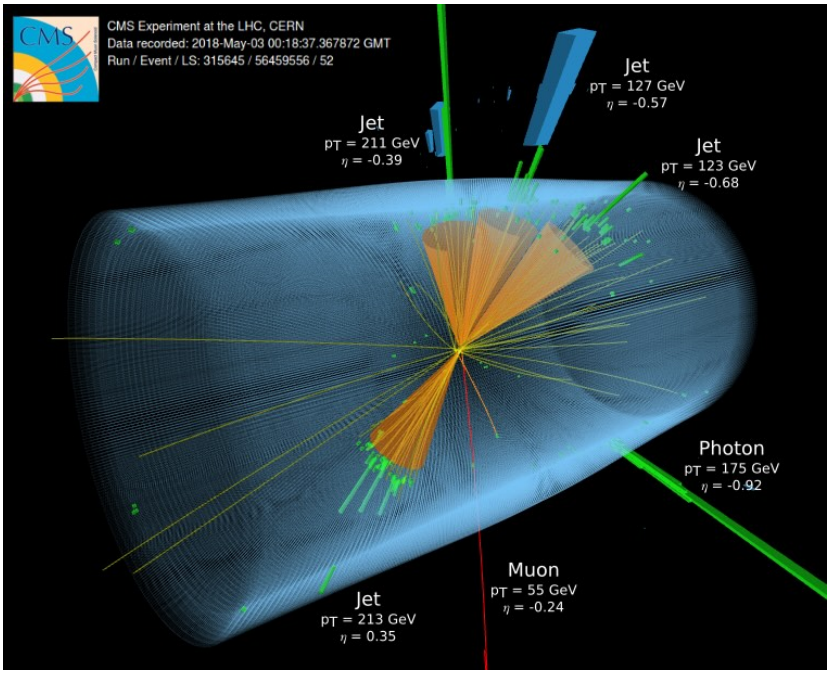

Figure 93: CMS event display where different objects are annotated by their identity, transverse momentum p_{T} and pseudorapidity η. Four hadronic jets as orange cones, one photon as a green electromagnetic calorimeter deposit, and one muon as the red line appear in this event. From CMS-PHO-EVENTS-2021-005.

We have that $\eta = 0$ is transverse to the beam while $\eta \to \pm\infty$ is parallel to the beam direction and $\theta = 45^\circ$ is about $\eta \simeq 0.88$. Lastly, ϕ is the azimuthal angle in the transverse plane to the beam.

We define η to make the detector have higher resolution in directions transverse to the beam. Interesting objects produced from hard collisions are usually ejected in the more transverse directions. The surface surrounding the detector is divided into $\Delta\eta$ and $\Delta\phi$, which coincides with how the detector components are segmented into **cells**. The region $\eta \lesssim 2.5$ is referred to as 'central' while the region $\eta \gtrsim 2.5$ towards the beam is called 'forward', which corresponds to a polar angle of $\theta \simeq 10^\circ$ from the beam direction.

We usually define the cone opening angle for objects like jets by

$$\Delta R = \sqrt{(\Delta\eta)^2 + (\Delta\phi)^2}. \tag{13.13}$$

Central jets usually have $\Delta R \sim 0.4$ Recombination algorithms used to reconstruct jets can adjust this ΔR parameter according to what kind of jets we want to analyse.

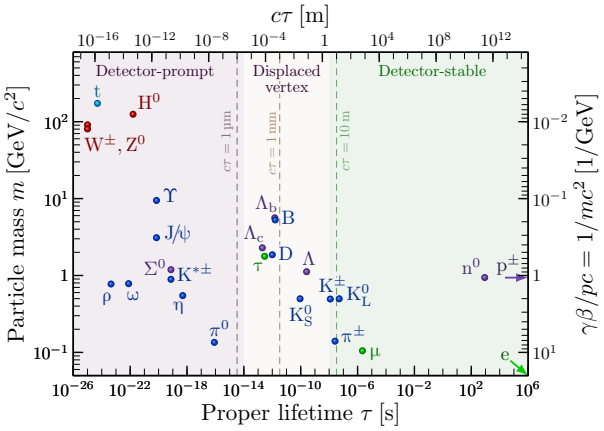

(a) SM particle proper lifetimes

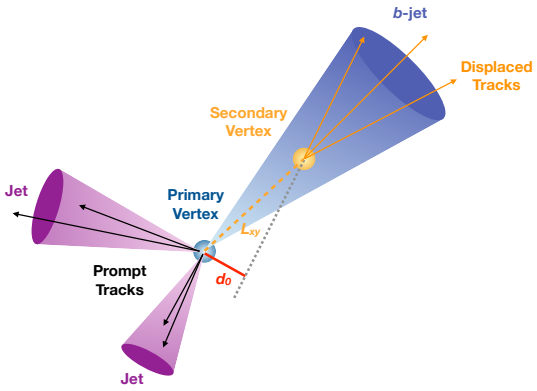

(b) Displaced vertex schematic

Figure 94: Prompt, displaced vertex, stable signatures of Standard Model particles. Proper lifetime τ and decay length $c\tau$ of particles relative to detector geometry from tikz.net. Metastable particles such as a B-hadron gives secondary vertices with finite impact parameters for heavy-flavour jet tagging from Ref. [94].

13.5 Particle identification

There are actually only a subset of the Standard Model particles we observe in modern collider detectors. Heavy states like the $W^{\pm}, Z, h$ bosons and top quark decay promptly at time scales of

$$t_W \sim \frac{1}{\Gamma} \sim \frac{1}{2\,\text{GeV}} \simeq 3.3 \times 10^{-25}\,\text{s}. \tag{13.14}$$

The lighter quarks hadronise due to QCD confinement at time scales governed by the QCD scale

$$t_{\text{QCD}} \sim \frac{1}{\Lambda_{\text{QCD}}} \simeq \frac{1}{200\,\text{MeV}} \simeq 3.3 \times 10^{-24}\,\text{s}. \tag{13.15}$$

These processes happen instantaneously relative to the capabilities of detector technologies, which are typically on the order of 0.1 to 10s of nanoseconds, depending on the detection technology. Unstable particles have a decay length of

$$d = \gamma\beta c\tau_{\text{rest}} \simeq \gamma(300\,\mu\text{m})\left(\frac{\tau_{\text{rest}}}{10^{-12}\,\text{s}}\right). \tag{13.16}$$

With these detectors in place, the signatures of standard LHC objects are illustrated in figure 91:

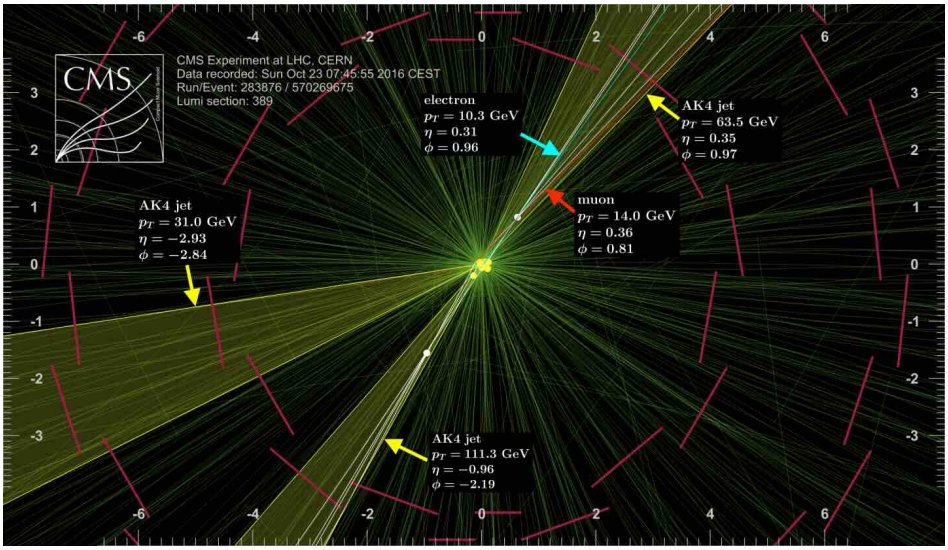

Figure 95: Event display from 2016 data collected at 13 TeV from the CMS Experiment showing displaced heavy-flavour tracks from CMS-PHO-EVENTS-2017-006. This is shown in *x*-*y* projection with the beam pipe into page. Three jets coloured yellow, one displaced muon, and one displaced electron tracks. Faint green lines show tracks with $p_{\mathrm{T}} > 0.5$ GeV. Yellow dots show the 44 primary vertices due to pileup. Displaced secondary vertices are white dots. The pink lines show the pixel detector.

- **Electrons and positrons** $e^{\pm}$: charged track with significant energy deposition in electromagnetic calorimeter and little to no hadronic activity.

- **Photons**: same as $e^{\pm}$ without corresponding hits in tracker.

- **Muons**: charged tracks in tracker, little to no deposition in calorimeters, activity in muon chambers.

- **Hadronic jets**: at ATLAS and CMS, collections of collimated hadrons are usually identified as a jet rather than individual hadrons. This allows an identification to the original hard quark or gluon that showers and hadronises. The signature is a conical spray of charged tracks left in tracker spatially correlated with significant energy deposition in both electromagnetic and hadronic calorimeters.

  Jet algorithms are employed to reconstruct the shower of particles resulting from parton hadronisation into a jet. This is done using algorithms that collect together deposits of calorimeter energy, where the preferred choice at the LHC ordered inversely to

their transverse momentum (called anti-k_T). This results in cone-shaped jets useful for experimental analysis.

- **Heavy-flavour jets**. Jets arising from a high-momentum b-quark can be identified due to the long lifetime distance $c\tau \sim 450\mu$m and relatively large mass. Figure 94 displays the hallmark signature tracks not all tracing back to the same interaction point, this being called a secondary (displaced) vertex. The impact parameter transverse to the beam line is denoted d_0.

- **Tau-lepton jets**. These have very short lifetimes $\tau_\tau \sim 10^{-13}$ s. They have a branching ratio of $\sim 49\%$ to a single charged hadron plus neutrino and $\sim 15\%$ to 3 charged hadrons plus neutrinos. These types of jets should be highly collimated. Reconstruction algorithms employ two cones to define the τ jets: 1) the signal cone is formed by surrounding the hadron shower with a cone off ΔR then 2) a larger ΔR isolation cone surrounds this first signal cone where there is little track or calorimetry activity. The signal cone requires 3 tracks and activity in the electromagnetic calorimeter. Leptonic decay channels are in principle indistinguishable from other sources of electrons and muons.

- **Neutrinos and invisibles particles**. Neutrinos are too weakly coupled to interact with conventional LHC detectors with high rate, so are classed as invisible at ATLAS and CMS. These are both the most difficult and most interesting signatures. Detectors are designed to be as hermetic as possible to impose momentum conservation in the plane transverse to the beam line:
$$\mathbf{p}_T^{\text{miss}} = -\sum_i \mathbf{p}_T^{\text{visible}}. \tag{13.17}$$
This is a two-vector in the x-y plane and its magnitude is denoted $E_T^{\text{miss}} = |\mathbf{p}_T^{\text{miss}}|$, called "missing transverse energy" or "MET". This is also the primary signature in the search for dark matter candidates.

Figure 93 shows an example annotated event display of various objects in the CMS detector. There are now interactive detector and event displays you can play with in your Internet browser[59].

[59] https://opendata.cern.ch/visualise/events/cms

14 Electroweak symmetry breaking

The city-sized colliders of LEP, Tevatron, LHC probe the fundamental dynamics of the Standard Model. At its heart is electroweak symmetry breaking via the Brout–Englert–Higgs mechanism. This generates the masses for the gauge bosons while leaving the photon massless via spontaneous symmetry breaking of a gauge theory. Direct empirical evidence of the underlying Higgs field is the experimental detection of the Higgs boson.

Let us proceed in a sequence of increasing sophistication, building up towards the Standard Model realisation of the mechanism:

- Simple illustration of spontaneous symmetry breaking.
- Abelian Higgs model: application to a gauge theory with a local U(1) symmetry.
- Standard Model: application to a chiral non-Abelian gauge theory of electroweak interactions.

14.1 Brout–Englert–Higgs mechanism

To illustrate the idea of spontaneous symmetry breaking, we can consider a very simple complex scalar field $\phi(x)$ with a quartic potential:

$$V(|\phi|^2) = \mu^2|\phi|^2 + \lambda|\phi|^4. \tag{14.1}$$

This system has a symmetry upon sign inversion $\phi \to -\phi$. We can find the minima and maxima by differentiating

$$0 = \frac{\partial V(\phi)}{\partial \phi} = (\mu^2 + 2\lambda\phi_0^2)\phi_0. \tag{14.2}$$

In the case $\mu^2 > 0$ and $\lambda > 0$, the only minimum is at $\phi_0 = 0$. Spontaneous symmetry breaking occurs when $\mu^2 < 0$, where the solutions become degenerate

$$\phi_0 = \pm\sqrt{\frac{-\mu^2}{2\lambda}}, \quad \phi_0 = 0. \tag{14.3}$$

We can visualise the shape of the potential as the sign of the quadratic term inverts in figure 96. The quartic potential $V(\phi^2)$ initially has a global minimum at $\phi^2 = 0$ when $\mu^2 > 0, \lambda > 0$. When the sign inverts $\mu^2 < 0$, the $\phi^2 = 0$ becomes unstable while the potential develops two minima. The system describing the scalar field settles into one of the two minima and the $\phi \to -\phi$ symmetry is broken.

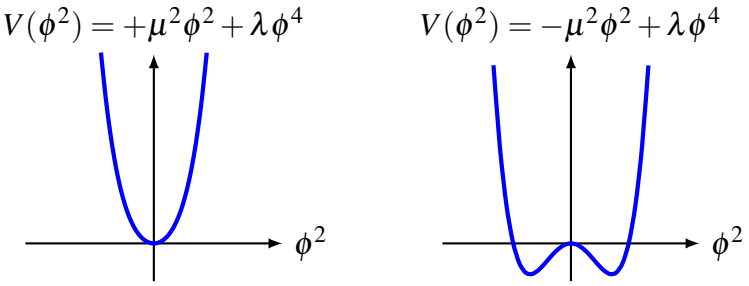

Figure 96: Simple visualisation of quartic function.

As an aside, this may seem rather contrived to the point of oversimplification. But the parameter undergoing sign inversion can be temperature dependent $\mu = \mu(T)$ and $\phi^2 \neq 0$ corresponds to a condensate when modelling superconductivity or the early universe phase transitions. We shall now illustrate its application in particle physics for mass generation in a gauge theory.

Abelian Higgs model

We now apply spontaneous symmetry breaking to the mechanism of mass generation in the simplest gauge theory: the **Abelian Higgs model**. This idea for mass generation was developed by numerous theoretical physicists in the 1960s and is now designated the Brout–Englert–Higgs mechanism. The Lagrangian comprises a massless vector A_μ interacting with a complex scalar $\phi(x)$ field

$$\mathscr{L} = -\frac{1}{4}F_{\mu\nu}F^{\mu\nu} + \frac{1}{2}(D_\mu\phi)(D^\mu\phi)^* - V(\phi^*\phi), \quad V(\phi^*\phi) = \lambda\left(\phi^*\phi - \tfrac{1}{2}v^2\right)^2, \tag{14.4}$$

where the covariant derivative is $D_\mu = \partial_\mu + \mathrm{i}eA_\mu$.

The Lagrangian is invariant under the U(1) Abelian local symmetry and gauge transformations:

$$\phi \to e^{\mathrm{i}\alpha(x)}\phi, \quad A_\mu \to A_\mu - (\partial_\mu\alpha)/e. \tag{14.5}$$

The scalar field rolls from the unstable centre $|\phi|^2 = 0$ down to the minimum of the potential at value $|\phi|^2 = v^2$, as sketched in figure 97. We assume the vev v to be real such that $\langle\phi\rangle = v$. We can expand the field $\phi(x)$ around the minimum in small perturbations $h(x)$

$$\phi(x) = \frac{\mathrm{e}^{\mathrm{i}\chi(x)}}{\sqrt{2}}(v + h(x)). \tag{14.6}$$

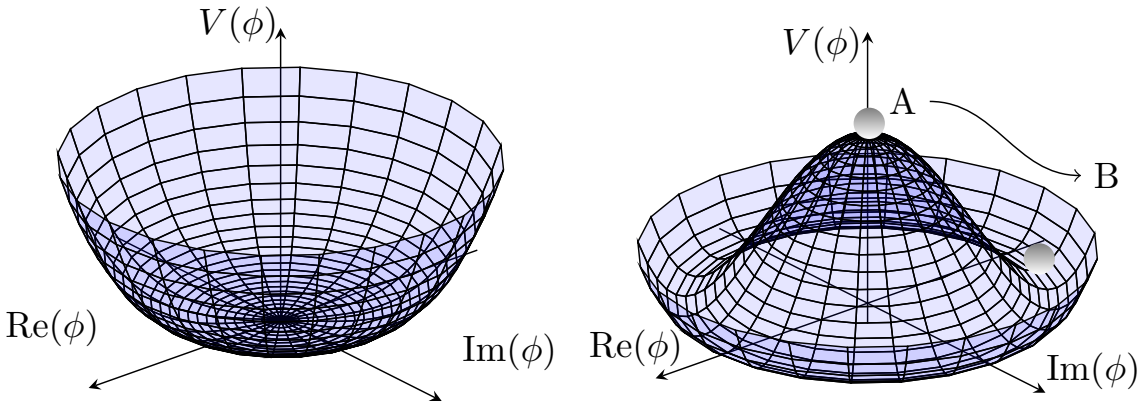

(a) Unbroken phase: "wine glass" (b) Broken phase: "wine bottle"

Figure 97: **Higgs potential visualisation**. The two-dimensional potential $V(\phi)$ starts from the characteristic "wine glass" shape. Spontaneous symmetry breaking occurs, after which into the shape becomes the base of a "wine bottle". Figures: adapted from tikz.net.

Substituting this into the kinetic and potential terms of the Lagrangian (14.4) gives

$$(D_\mu\phi)^*(D^\mu\phi) = \frac{1}{2}\left[(\partial_\mu h)^2 + (v+h)^2(\partial^\mu\chi + eA^\mu)^2\right], \tag{14.7}$$

$$V(\phi^*\phi) = \lambda\left[\frac{1}{2}(v+h)^2 - \frac{v^2}{2}\right]^2 = \lambda v^2h^2 + \lambda v^2h^3 + \frac{\lambda}{4}h^4. \tag{14.8}$$

Right now, we now see the propagating scalar degree of freedom $h(x)$ has a mass term $m_h^2/2 = \lambda v^2$; this corresponds to states oscillating up and down the radial direction of the potential in figure 97. We also see a $(\partial_\mu\chi)^2$ term that appears without any quadratic mass term; this is the **Nambu–Goldstone boson** corresponding to states rotating around the well at constant radius of the wine bottle in figure 97. To illuminate the physical vector degrees of freedom, we fix the gauge by redefining $A_\mu \to A_\mu - (\partial_\mu\chi)/e$, which is called the unitary gauge. The Lagrangian then becomes

$$\mathscr{L} = \underbrace{-\frac{1}{4}F_{\mu\nu}F^{\mu\nu} + \frac{e^2v^2}{2}A^2}_{\text{massive vector}} + \underbrace{\frac{1}{2}(\partial_\mu h)^2 - \lambda v^2h^2}_{\text{mass real scalar}} - \underbrace{\lambda v^2h^3 - \frac{\lambda}{4}h^4}_{\text{Higgs self-couplings}} + \underbrace{\frac{1}{2}(vh+h^2)A^2}_{\text{Higgs-vector couplings}}. \tag{14.9}$$

This makes manifest the **Brout–Englert–Higgs mechanism**: a non-zero vacuum expectation value of the complex scalar reshuffles the degrees of freedom (abbreviated dof.) in the theory

$$\boxed{\begin{pmatrix}\phi : 2\text{ dof.}\\ A_\mu, m_A = 0 : 2\text{ dof.}\end{pmatrix} \langle\phi\rangle \neq 0 \longrightarrow \begin{pmatrix}h : 1\text{ dof.}\\ A_\mu, m_A \neq 0 : 3\text{ dof.}\end{pmatrix}.} \tag{14.10}$$

Writing this explicitly makes it clear how the accounting of degrees of freedom are conserved. To recap on what we just saw:

- Originally, we started with two degrees of freedom in the massless vector A_μ and two in the complex scale $\phi(x) = \mathrm{Re}\phi(x) + \mathrm{iIm}\phi_(x)$ in equation (14.4).
- After symmetry breaking, the scalar acquires a vacuum expectation value $\langle\phi\rangle = v$, a massless Goldstone boson $\chi(x)$ appears and a real scalar $h(x)$ gains a mass m_h.
- By fixing the gauge choice, the massless Nambu–Goldstone boson disappears and is reassigned[60] to become the longitudinal polarisation of the massive vector A_μ. This supplements the original two transverse polarisations of a massless vector.
- At the end, we have one degree of freedom in the real scalar $h(x)$ and three degrees of freedom in the massive vector A_μ.

Applying this to chiral and non-Abelian structure of the electroweak force is slightly more complicated and is central to the Standard Model.

14.2 Glashow–Salam–Weinberg model

The Brout–Englert–Higgs mechanism applied to the Standard Model of electroweak interactions is slightly more complicated than the Abelian toy example. The SM Higgs field Φ_{SM} is exists in an SU(2) doublet of complex scalar fields, with 4 degrees of freedom. Two degrees of freedom of Φ of which are charged and the remaining two are neutral. We arrange the Higgs field into a weak isospin $\mathrm{SU(2)_L}$ doublet

$$\Phi_{\mathrm{SM}} = \begin{pmatrix} \phi^+ \\ \phi^0 \end{pmatrix} = \frac{1}{\sqrt{2}} \begin{pmatrix} \phi_1 + \mathrm{i}\phi_2 \\ \phi_3 + \mathrm{i}\phi_4 \end{pmatrix}. \tag{14.11}$$

This Higgs doublet interacts with a massless hypercharge vector B_μ and the three massless weak isospin $W_\mu^{(1,2,3)}$ vector fields. Analogous to equation (14.10), we again write out explicitly how the degrees of freedom (dof.) reshuffles to ensure our accounting adds up:

$$\begin{pmatrix} \Phi_{\mathrm{SM}} = (\phi^+, \phi^0) : 4 \text{ dof.} \\ B_\mu, m_B = 0 : 2 \text{ dof.} \\ W_\mu^{(1,2,3)}, m_W = 0 : 3 \times 2 \text{ dof.} \end{pmatrix} \underset{\longrightarrow}{\langle\Phi_{\mathrm{SM}}\rangle \neq 0} \begin{pmatrix} h : 1 \text{ dof.} \\ A_\mu, m_A = 0 : 2 \text{ dof.} \\ Z_\mu, m_Z \neq 0 : 3 \text{ dof.} \\ W_\mu^\pm, m_W \neq 0 : 2 \times 3 \text{ dof.} \end{pmatrix}. \tag{14.12}$$

[60] Textbooks often uses the technical jargon of the Nambu–Goldstone boson being "eaten".

After electroweak symmetry breaking, there is one real Higgs boson h, a massless photon, a neutral massive vector Z, and two charged massive vector $W^{\pm}$ bosons fields. Three of the degrees of freedom of the complex Higgs doublet comprise the Nambu–Goldstone bosons that are reassigned to ("eaten by") the longitudinal components of the massive vector bosons. We start with 12 physical propagating modes and also end up with 12 physical propagating modes: excellent.

The Lagrangian for the Higgs doublet of complex scalar fields is

$$\mathscr{L}_{\text{Higgs}} = (D^{\mu}\Phi)(D_{\mu}\Phi)^{\dagger} - V(\Phi^{\dagger}\Phi). \tag{14.13}$$

The Higgs field Lagrangian has the desired $\mathrm{U(1)_Y}$ and $\mathrm{SU(2)_L}$ local symmetries

$$\begin{pmatrix}\phi^{+}\\ \phi^{0}\end{pmatrix} \to \begin{pmatrix}\mathrm{e}^{\mathrm{i}g_1 Y_\phi \beta(x)/2} & 0\\ 0 & \mathrm{e}^{\mathrm{i}g_1 Y_\phi \beta(x)/2}\end{pmatrix}\begin{pmatrix}\phi^{+}\\ \phi^{0}\end{pmatrix} \qquad U(1)_Y \text{ symmetry} \tag{14.14}$$

$$\begin{pmatrix}\phi^{+}\\ \phi^{0}\end{pmatrix} \to \mathrm{e}^{\mathrm{i}g_2 I_\phi \sigma_a \alpha(x)}\begin{pmatrix}\phi^{+}\\ \phi^{0}\end{pmatrix} \qquad SU(2)_L \text{ symmetry.} \tag{14.15}$$

The Higgs field is defined to have the following weak hypercharge Y_Φ and isospin I_Φ:

$$Y_\Phi = 1, \quad I_\Phi = \frac{1}{2}. \tag{14.16}$$

Using these values, the relevant covariant derivative for the Higgs field under these local transformations is

$$D_\mu \Phi = \left(\partial_\mu - \frac{\mathrm{i}}{2}g_1 B_\mu - \frac{\mathrm{i}}{2}g_2 \sigma_a W_\mu^a\right)\Phi. \tag{14.17}$$

These covariant derivatives act on the left-handed leptons formed into $\mathrm{SU(2)_L}$ doublets

$$L_\ell = \begin{pmatrix}\nu_\ell\\ \ell\end{pmatrix}_L = \left\{\begin{pmatrix}\nu_e\\ e\end{pmatrix}_L, \begin{pmatrix}\nu_\mu\\ \mu\end{pmatrix}_L, \begin{pmatrix}\nu_\tau\\ \tau\end{pmatrix}_L\right\}. \tag{14.18}$$

Meanwhile the right-handed leptons form a singlet, comprising only of the electron flavour without neutrinos:

$$R_\ell = \ell_R = \{e_R, \mu_R, \tau_R\}. \tag{14.19}$$

The left-handed doublet experience $\mathrm{SU(2)_L}$ transformations symmetry while the right-handed leptons remain invariant:

$$\begin{pmatrix}\nu_\ell\\ \ell\end{pmatrix}_L \to \mathrm{e}^{\mathrm{i}g_2 I_L \sigma_a \alpha^a}\begin{pmatrix}\nu_\ell\\ \ell\end{pmatrix}_L, \tag{14.20}$$

$$\ell_R \to \ell_R. \tag{14.21}$$

The σ_a are the standard Pauli matrices. That $\mathrm{SU(2)_L}$ exhibits couples only to left-handed spinors and not right-handed ones is a manifestation of maximal parity violation in electroweak interactions. Consistent to this definition, the left-handed doublet and right-handed singlet take on these **weak isospin** values:

$$I_L = \frac{1}{2}, \qquad I_R = 0. \tag{14.22}$$

As the right-handed weak isospin value is zero, the nonchalance of the $\mathrm{SU(2)_L}$ is exhibited as the identity operator acting on ℓ_R. Table 6 summarise all the charges of the leptons and quarks in the Standard Model.

For the lepton fields L, ℓ_R to acquire mass after symmetry breaking, we couple them to the Higgs field via Yukawa interaction terms

$$\mathscr{L}_{\text{Yukawa}} = -y_\ell \left(\bar{L}\Phi\ell_R + \bar{\ell}_R\Phi^\dagger L \right). \tag{14.23}$$

This remain invariant under the local $\mathrm{SU(2)_L} \times \mathrm{U(1)_Y}$ symmetry. The Higgs-lepton coupling constant y_ℓ dictates the strength with which the lepton fields couple to the Higgs field. The kinetic terms for the three $\mathrm{SU(2)_L}$ weak isospin fields are W^a_μ and $\mathrm{U(1)_Y}$ hypercharge fields are B_μ:

$$\mathscr{L}_{\text{gauge}} = -\frac{1}{4} W^a_{\mu\nu} W_a^{\mu\nu} - \frac{1}{4} B_{\mu\nu} B^{\mu\nu}, \tag{14.24}$$

where the field strengths are correspondingly

$$B_{\mu\nu} = \frac{1}{\mathrm{i}g_1}[D_\mu, D_\nu] = \partial_\mu B_\nu - \partial_\nu B_\mu, \tag{14.25}$$

$$W^a_{\mu\nu} = \frac{1}{\mathrm{i}g_2}[D_\mu, D_\nu]^a = \partial_\mu W^a_\nu - \partial_\nu W^a_\mu - g_2 f^{abc} W^b_\mu W^c_\nu. \tag{14.26}$$

Putting all the ingredients together with the Dirac kinetic term describing the fermions, we arrive at the Glashow–Salam–Weinberg electroweak model of leptons before symmetry breaking

$$\begin{aligned}
\mathscr{L}_{\text{EW}} = \quad & -\frac{1}{4} W^a_{\mu\nu} W_a^{\mu\nu} - \frac{1}{4} B_{\mu\nu} B^{\mu\nu} && \text{gauge kinetic} \\
& + \mathrm{i}\bar{L}_\ell \gamma^\mu D_\mu L_\ell + \mathrm{i}\bar{\ell}_R \gamma^\mu D_\mu \ell_R && \text{Dirac leptons} \\
& - y_\ell \left(\bar{L}\Phi\ell_R + \ell_R\Phi^\dagger L \right) && \text{Yukawa couplings (14.23)} \\
& + (D^\mu\Phi)(D_\mu\Phi)^\dagger - V(\Phi^\dagger\Phi) && \text{Higgs field (14.13)}
\end{aligned} \tag{14.27}$$

This is starting to look like the Lagrangian that appears on the CERN mug of figure 6. Here the only massive field is the Higgs ϕ. The gauge $B_{\mu\nu}$, $W^a_{\mu\nu}$ and lepton fields L_l, R_l remain massless prior to symmetry breaking i.e. so long as $\mathscr{L}_{EW}$ remains invariant under the $\mathrm{SU(2)_L} \times \mathrm{U(1)_Y}$ local symmetry.

	Charge Gauge group Symbol	Colour $SU(3)_C$ C	Weak Isospin $SU(2)_L$ I_3	Hypercharge $U(1)_Y$ Y	Electric $U(1)_{EM}$ $Q = Y + \frac{I_3}{2}$
Leptons	$\begin{pmatrix}\nu_{eL}\\ e_L\end{pmatrix}, \begin{pmatrix}\nu_{\mu L}\\ \mu_L\end{pmatrix}, \begin{pmatrix}\nu_{\tau L}\\ \tau_L\end{pmatrix}$	0	$\begin{pmatrix}+\frac{1}{2}\\ -\frac{1}{2}\end{pmatrix}$	-1	$\begin{pmatrix}0\\ -1\end{pmatrix}$
	$\nu_{eR}, \nu_{\mu R}, \nu_{\tau R}$	0	0	0	0
	e_R, μ_R, τ_R	0	0	-2	-1
Quarks	$\begin{pmatrix}u_L\\ d_L\end{pmatrix}, \begin{pmatrix}c_L\\ s_L\end{pmatrix}, \begin{pmatrix}t_L\\ b_L\end{pmatrix}$	(r,g,b)	$\begin{pmatrix}+\frac{1}{2}\\ -\frac{1}{2}\end{pmatrix}$	$+\frac{1}{3}$	$\begin{pmatrix}+\frac{2}{3}\\ -\frac{1}{3}\end{pmatrix}$
	u_R, c_R, t_R	(r,g,b)	0	$+\frac{4}{3}$	$+\frac{2}{3}$
	d_R, s_R, b_R	(r,g,b)	0	$-\frac{2}{3}$	$-\frac{1}{3}$

Table 6: Charge assignment for the Standard Model matter (fermion) content. Fermions can carry colour charge C, weak isospin I_3, hypercharge Y, and electric charge $Q = Y + I_3/2$. This corresponds to the $SU(3)_C$, $SU(2)_L$, $U(1)_Y$, $U(1)_{EM}$ gauge groups, respectively. The left-handed fermions are displays as doublets **2** of $SU(2)_L$. The quarks are implicitly triplets **3** of $SU(3)_C$ with (r,g,b) colour charges. The right-handed neutrinos are greyed out given they are hypothetical singlets (uncharged) under the SM gauge groups.

14.3 Generating gauge boson masses

We now walk through the mathematical anatomy of mass generation for the fermions and gauge bosons in the Standard Model via electroweak symmetry breaking. The Higgs potential is given by (where we can define an additive constant)

$$V(\Phi^\dagger\Phi) = \lambda\left(|\Phi^\dagger\Phi|^2 - \frac{v^2}{2}\right)^2. \tag{14.28}$$

The first step is to define the electroweak vacuum expectation value and the Higgs as an excitation of this. The minimum is no longer at the origin $(\Phi)_0 = 0$ but is instead is a continuously degenerate minima satisfying

$$\frac{\partial V}{\partial \Phi} = 0 \quad \Rightarrow \quad (\Phi^\dagger\Phi)_0 = \frac{1}{2}\left(\phi_1^2 + \phi_2^2 + \phi_3^2 + \phi_4^2\right) = \frac{\mu^2}{\lambda}, \tag{14.29}$$

defining $\mu^2 = v^2\lambda/2$. Without loss of generality, we choose the ground state to be

$$(\Phi_i)_0 = \begin{cases} \sqrt{\dfrac{2\mu^2}{\lambda}} = v, & \text{if } i = 1; \\ 0, & \text{if } i = 2,3,4. \end{cases} \tag{14.30}$$

Now we find the new non-zero vacuum expectation value is

$$\langle 0|\Phi|0\rangle = \begin{pmatrix} \phi^+ \\ \phi^0 \end{pmatrix}_0 = \frac{1}{\sqrt{2}} \begin{pmatrix} 0 \\ v \end{pmatrix} \tag{14.31}$$

We can consider small perturbations $h(x) \ll v$ about the new non-zero vacuum expectation value of ϕ in the unitary gauge

$$\Phi(x) = \frac{1}{\sqrt{2}} \begin{pmatrix} 0 \\ v + h(x) \end{pmatrix}. \tag{14.32}$$

The consequences of this electroweak symmetry breaking, leading to non-zero vacuum expectation value of the Higgs field, are profound. We substitute the small field fluctuations of equation (14.32) into the kinetic term to give

$$(D_\mu \Phi)^\dagger (D_\mu \Phi) = \frac{1}{2}(\partial_\mu h)^2 + \text{terms involving gauge fields.} \tag{14.33}$$

We shall study the terms involving gauge fields below, which generates the gauge boson masses.

Generation of W boson masses

The masses of the gauge bosons after symmetry breaking are encoded in $(D_\mu\Phi)(D^\mu\Phi)^\dagger$. This is a somewhat fiddly but rewarding calculation. Using the explicit forms of the Pauli matrices and acting D_μ on the unitary gauged $H(x)$, we find

$$\begin{aligned} D_\mu \Phi &= \left[\partial_\mu - \frac{\mathrm{i}}{2} \begin{pmatrix} g_1 B_\mu + g_2 W_\mu^{(3)} & g_2 \left(W_\mu^{(1)} - \mathrm{i} W_\mu^{(2)} \right) \\ g_2 \left(W_\mu^{(1)} + \mathrm{i} W_\mu^{(2)} \right) & g_1 B_\mu - g_2 W_\mu^{(3)} \end{pmatrix} \right] \frac{1}{\sqrt{2}} \begin{pmatrix} 0 \\ v + h(x) \end{pmatrix} \\ &= \frac{1}{\sqrt{2}} \begin{pmatrix} -\frac{\mathrm{i} g_2}{2} \left(W_\mu^{(1)} - \mathrm{i} W_\mu^{(2)} \right) (v + h(x)) \\ \partial_\mu h(x) - \frac{\mathrm{i}}{2} \left(g_1 B_\mu - g_2 W_\mu^{(3)} \right) (v + h(x)) \end{pmatrix}. \end{aligned} \tag{14.34}$$

Now take the Hermitian conjugate of this to yield $(D^\mu\phi)^\dagger$ and multiplying through with a plateful of algebra to write

$$\begin{aligned}(D_\mu\Phi)(D^\mu\Phi)^\dagger = &\frac{1}{2}(\partial_\mu h)(\partial^\mu h)\\ &+\frac{g_W^2}{8}\left(W_\mu^{(1)}-\mathrm{i}W_\mu^{(2)}\right)\left(W^{(1)\mu}+\mathrm{i}W^{(2)\mu}\right)(v+h(x))^2\\ &+\frac{1}{8}\left(g_1B_\mu-g_2W_\mu^{(3)}\right)\left(g_1B^\mu-g_2W^{(3)\mu}\right)(v+h(x))^2\,.\end{aligned} \tag{14.35}$$

For now we retain only terms involving v^2 as we would like to consider how the gauge fields interact with the now non-zero expectation value of the Higgs field. Thus we have

$$\begin{aligned}(D_\mu\Phi)(D^\mu\Phi)^\dagger = &\frac{1}{2}(\partial_\mu h)(\partial^\mu h)+\underbrace{\frac{g_2^2v^2}{8}}_{\text{mass term}}\left[\left(W_\mu^{(1)}\right)^2+\left(W_\mu^{(2)}\right)^2\right]\\ &+\frac{v^2}{8}\left(g_1B_\mu-g_2W_\mu^{(3)}\right)^2+\text{terms involving } h(x).\end{aligned} \tag{14.36}$$

We can now proceed to extract the masses of the W bosons. This is encoded in the second line of (14.36) as the coefficients of the $\left(W_\mu^{(1,2)}\right)^2$ terms. There are two charged $W_\mu^\pm$ boson fields comprising linear combinations of $W_\mu^{(1,2)}$ with equal mass m_W

$$\boxed{W_\mu^\pm=\frac{W_\mu^{(1)}\mp\mathrm{i}W_\mu^{(2)}}{\sqrt{2}},\quad \frac{m_W^2}{2}=\frac{g_2^2v^2}{8}.} \tag{14.37}$$

The mass of the W bosons is determined by the coupling g_2 of the $\mathrm{SU(2)_L}$ gauge interaction and the vacuum expectation value of the Higgs field v.

Generation of photon and massive Z boson

Surreptitiously concealed in the last term of (14.36) are the massive Z boson and photon fields, which we first write as a quadratic form

$$\frac{v^2}{4}\left(g_1B_\mu-g_2W_\mu^{(3)}\right)^2=\frac{v^2}{4}\begin{pmatrix}W_\mu^{(3)} & B_\mu\end{pmatrix}\begin{pmatrix}g_2^2 & -g_1g_2\\ -g_1g_2 & g_1^2\end{pmatrix}\begin{pmatrix}W^{(3)\mu}\\ B^\mu\end{pmatrix}. \tag{14.38}$$

The off-diagonal elements in the matrix couple the $W_\mu^{(3)}$ and B_μ fields. Therefore, to find the physical independently propagating fields, we should diagonalise this matrix. Solving this

eigenvalue problem using our favourite pen-and-paper or computer method, we find (14.38) rewritten elegantly diagonal:

$$\frac{1}{2}\begin{pmatrix}A_\mu & Z_\mu\end{pmatrix}\begin{pmatrix}0 & 0\\ 0 & \frac{v^2}{2}\left(g_1^2+g_2^2\right)\end{pmatrix}\begin{pmatrix}A^\mu\\ Z^\mu\end{pmatrix}=\frac{1}{2}\begin{pmatrix}A_\mu & Z_\mu\end{pmatrix}\begin{pmatrix}m_A^2 & 0\\ 0 & m_Z^2\end{pmatrix}\begin{pmatrix}A^\mu\\ Z^\mu\end{pmatrix}. \tag{14.39}$$

From this we can read off the masses of the A_μ and Z_μ fields. Amazingly, we see a massless boson field A_μ, more affectionately known as the photon, in addition to a massive neutral boson field Z_μ. This happened as a consequence of breaking the electroweak $\mathrm{SU(2)_L}\times\mathrm{U(1)_Y}$ symmetry. These physical boson fields A_μ and Z_μ are linear combinations of the initial $W_\mu^{(3)}$ and B_μ fields:

$$\begin{pmatrix}A_\mu\\ Z_\mu\end{pmatrix}=\frac{1}{\sqrt{g_1^2+g_2^2}}\begin{pmatrix}g_2 & g_1\\ -g_1 & g_2\end{pmatrix}\begin{pmatrix}B_\mu\\ W_\mu^{(3)}\end{pmatrix}. \tag{14.40}$$

This is a rotation of basis, which we make manifest by defining the **Weinberg angle** $\tan\theta_W = g_1/g_2$ relating the ratio of $\mathrm{U(1)_Y}$ and $\mathrm{SU(2)_L}$ couplings to rewrite equation (14.40) as

$$\boxed{\begin{pmatrix}A_\mu\\ Z_\mu\end{pmatrix}=\begin{pmatrix}\cos\theta_W & \sin\theta_W\\ -\sin\theta_W & \cos\theta_W\end{pmatrix}\begin{pmatrix}B_\mu\\ W_\mu^{(3)}\end{pmatrix},\quad m_A^2=0,\quad m_Z^2=\frac{v^2}{2}\left(g_1^2+g_2^2\right).} \tag{14.41}$$

With these relations and equation (14.37), we can rewrite the Z boson mass as $m_Z=\frac{vg_2}{\sqrt{2}\cos\theta_W}$ to obtain a key prediction of electroweak symmetry breaking

$$\frac{m_W}{m_Z}=\cos\theta_W. \tag{14.42}$$

The electric charge e is then related to the $\mathrm{U(1)_Y}$ and $\mathrm{SU(2)_L}$ couplings by

$$e=g_1\sin\theta_W=g_2\cos\theta_W. \tag{14.43}$$

The relationship of electric charge with hypercharge and weak isospin couplings is usually referred to as **electroweak unification**. Knowing $e=\sqrt{4\pi\alpha_{\mathrm{EM}}}\approx 0.3$ and measuring $\cos\theta_W=m_W/m_Z$, we can determine the couplings g_1 and g_2.

Electroweak symmetry breaking results in the $\mathrm{SU(2)_L}\times\mathrm{U(1)_Y}$ gauge group being replaced by the electromagnetism $\mathrm{U(1)_{EM}}$:

$$\langle\Phi\rangle\neq 0 \quad\Rightarrow\quad \mathrm{SU(2)_L}\times\mathrm{U(1)_Y}\to\mathrm{U(1)_{EM}}. \tag{14.44}$$

In terms of the physical fields, interactions of electroweak gauge bosons to fermion currents $j^\mu = \bar{\psi}\gamma^\mu\psi$ take the form

$$-\mathscr{L}_{\rm EW}^{\rm int} = -\underbrace{eA_\mu j^\mu_{\rm EM}}_{\rm EM} + \underbrace{\frac{e}{\sqrt{2}\sin\theta_W}\left(W^+_\mu j^\mu_+ - W^-_\mu j^\mu_-\right)}_{\text{charged current}} + \underbrace{\frac{e}{\sin\theta_W\cos\theta_W}Z_\mu j^\mu_Z}_{\text{neutral current}} \tag{14.45}$$

Let us state the charged currents are (and similar for the other generations)

$$j^+_\mu = \bar{u}_L\bar{\sigma}^\mu d_L + \bar{\nu}_L\bar{\sigma}^\mu e_L, \tag{14.46}$$

$$j^-_\mu = \bar{d}_L\bar{\sigma}^\mu u_L + \bar{e}_L\bar{\sigma}^\mu \nu_L. \tag{14.47}$$

The familiar electromagnetic current and neutral current interactions look like

$$j^\mu_{\rm EM} = \sum_f Q_f(\bar{f}_L\bar{\sigma}^\mu f_L + \bar{f}_R\sigma^\mu f_R), \tag{14.48}$$

$$j^\mu_Z = \frac{1}{2}(\bar{u}_L\bar{\sigma}^\mu u_L - \bar{d}_L\bar{\sigma}^\mu d_L + \bar{\nu}_L\bar{\sigma}^\mu\nu_L - \bar{e}_L\bar{\sigma}^\mu e_L) - \sin^2\theta_W j^\mu_{\rm EM} \tag{14.49}$$

The fundamental vertex of charged-current interaction showing fermions (quarks q, charged leptons ℓ and neutrinos) coupling with the $W^\pm$ boson has the Feynman diagrams:

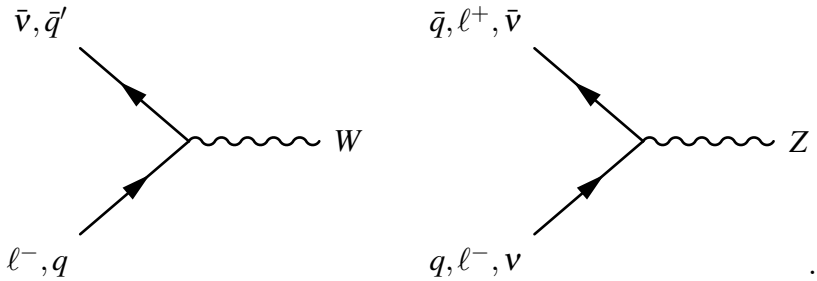

. (14.50)

Accounting for mass differences, the $W^\pm$ interact with each generation in identical ways. Consequently, the vertex of leptons and the $W^\pm$ bosons have the same weak coupling constant g_W, independent of the lepton flavour. The fundamental neutral-current interaction showing fermions (quarks q, charged leptons ℓ and neutrinos) coupling with the Z boson has this Feynman diagram.

The electrically charged leptons experience the electromagnetic and weak interactions while the neutrinos, being neutral, only experience the weak interaction. Each lepton is associated with a lepton flavour number. The electron lepton number L_e for example is given by

$$L_e = N(e^-) - N(e^+) + N(\nu_e) - N(\bar{\nu}_e), \tag{14.51}$$

where $N(X)$ denotes the number of X particles in a state. Lepton numbers for the μ and τ flavours are similarly defined by replacing e above with the flavour under discussion. In the Standard Model, the total lepton number

$$L_\ell = L_e + L_\mu + L_\tau \tag{14.52}$$

is conserved in all interactions.

Historically, the electroweak theory is due to work by Sheldon Glashow, Abdus Salam and Steven Weinberg, culminating around 1968. It made the surprising prediction that there should exist an electrically neutral massive gauge boson Z^0 which is heavier than two charged gauge bosons $W^\pm$, related by a parameter θ_W.

14.4 Discovery of W and Z bosons

The first indirect evidence for a neutral weak boson was the observation of **neutral current** interactions. At the CERN Proton Synchrotron (PS), they were able to create muon-neutrinos ν_μ from pion decays that scattered off quarks and electrons (figure 99):

$$\nu + q \to \nu + q \tag{14.53}$$

$$\nu + e^- \to \nu + e^-. \tag{14.54}$$

Such events are rather striking given a stationary electron suddenly and spontaneously gets knocked by the invisible neutrino. It is inferred that there exists a heavy neutral particle mediating these processes, which is later identified as the Z boson. These experiments were performed by the Gargamelle bubble chamber in 1973 (figure 98).

Super Proton Synchrotron

In 1983, the UA1 and UA2 collaborations[61] used events from the Super Proton Synchrotron (SPS) to directly observe the $W^\pm$ bosons in proton–antiproton $p\bar{p}$ collisions [95, 96] with centre-of-mass energies of $> 540\,\text{GeV}$. This was such that the interacting quarks carried the required $\sim 100\,\text{GeV}$ to form these heavy bosons on-shell. In 1968, the electromagnetic and weak interactions were unified into a single unified electroweak theory at high energies. One consequence of this theory is the prediction of a neutral current reactions mediated by a Z^0 boson. The $W^\pm$ and Z^0, bosons were discovered by in 1983. The masses are measured to be

$$m_W = 80.385 \pm 0.015\,\text{GeV},$$
$$m_Z = 91.1876 \pm 0.0021\,\text{GeV}.$$

[61] UA stands for Underground Area.

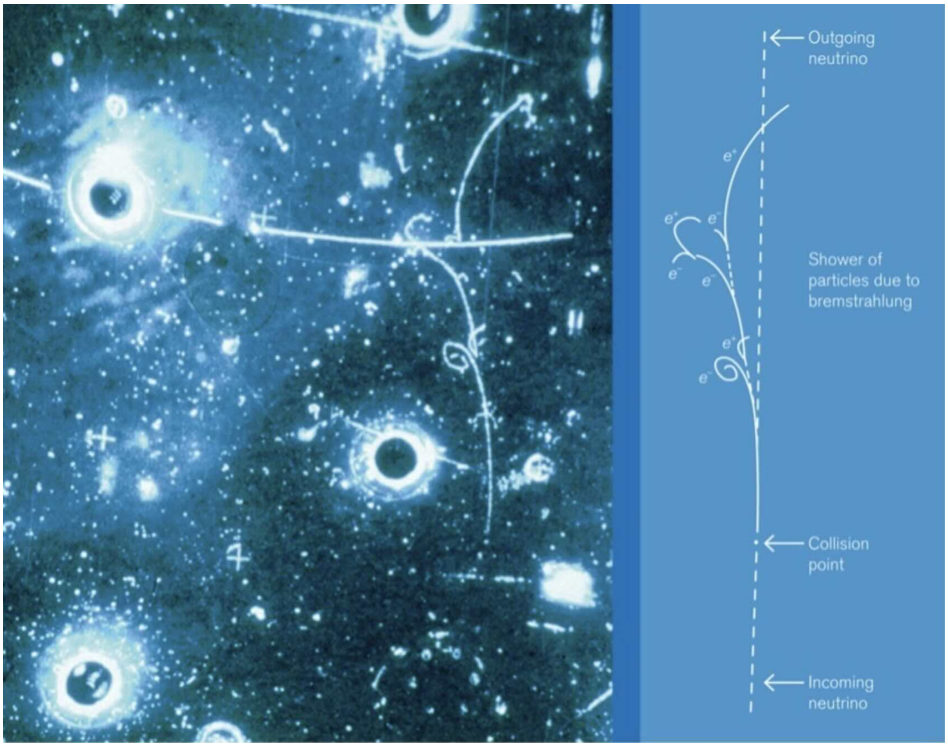

Figure 98: Neutral current by Gargemelle. Image from CERN

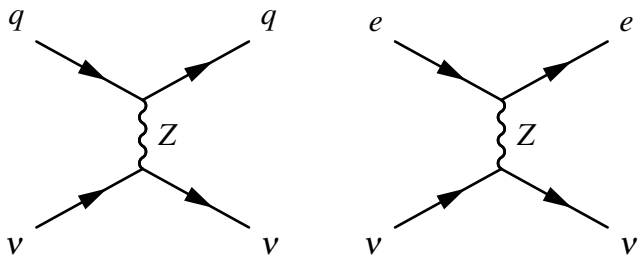

Figure 99: Neutrino-quark and neutrino-electron scattering that provided evidence for weak neutral current interactions, as indirect evidence for the existence of the Z boson.

The masses of the weak $W^{\pm}$ and Z bosons relate the mixture of the original hypercharge B_μ and weak isospin boson fields W^a_μ.

The Z boson is like the $W^{\pm}$ but is neutral and slightly more massive at $m_{Z^0} \approx 91\,\text{GeV}/c^2$. It interacts with all quarks and leptons but **conserves flavour** for any process in contrast to charged currents involving $W^{\pm}$. Thus no quark mixing occurs.

We calculate the centre-of-mass energy for production. Let each quark and antiquark carry fractions f_q and $f_{\bar{q}}$ of the proton and antiproton 4-momenta respectively. To produce a

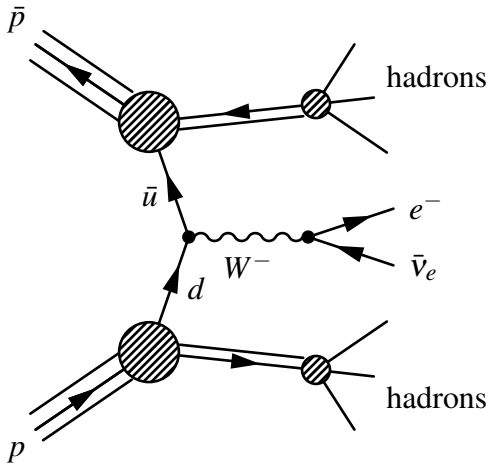

Figure 100: Production of W^- bosons via proton–antiproton collision and decay via $e^-\bar{\nu}_e$.

$W^\pm$ with mass m_W close to resonance, we conserve 4-momenta of the quarks in the centre-of-mass frame:

$$m_W^2 = (\mathsf{P}_q + \mathsf{P}_{\bar{q}})^2 = \mathsf{P}_q^2 + \mathsf{P}_{\bar{q}}^2 + 2\mathsf{P}_q \cdot \mathsf{P}_{\bar{q}} \tag{14.55}$$

The beam energies are much greater than the quark energies so $\mathsf{P}_q^2 \approx 0$ and $\mathsf{P}_{\bar{q}}^2 \approx 0$. The 4-momenta of the proton and antiproton are[62]

$$\mathsf{P}_q = f_q \begin{pmatrix} E_p \\ \mathbf{k}_p \end{pmatrix}, \qquad \mathsf{P}_{\bar{q}} = f_{\bar{q}} \begin{pmatrix} E_{\bar{p}} \\ -\mathbf{k}_{\bar{p}} \end{pmatrix}$$

Setting the magnitudes of their components to be equal, (14.55) becomes

$$m_W^2 = 4 f_q f_{\bar{q}} E_p^2. \tag{14.56}$$

Adhering to the particle physics convention of $\sqrt{s} = E_{\text{CM}}$ as the centre-of-mass energy, we obtain the condition to produce $W^\pm$ resonance:

$$\sqrt{s} = \frac{m_W}{\sqrt{f_q f_{\bar{q}}}}. \tag{14.57}$$

Figure 100 illustrates the dominant mechanism in producing W^- bosons via $p\bar{p}$ collisions. The outgoing quarks readily fragment into hadrons, generating significant background

[62] We use $\mathbf{k}$ for 3-momentum to minimise potential grief confusing it with the proton label p.

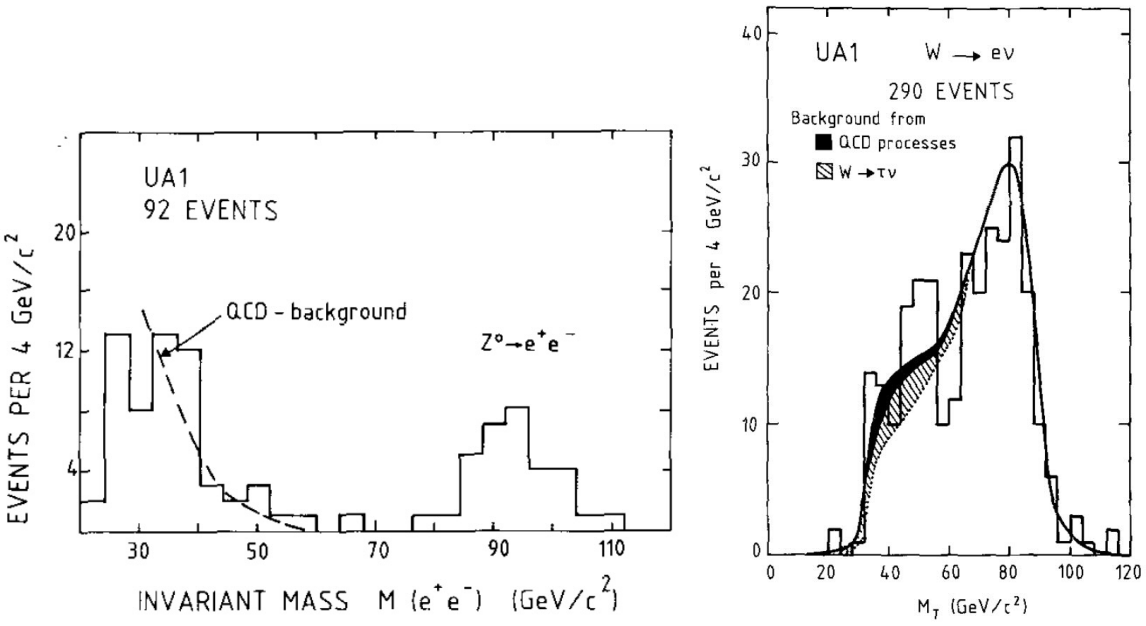

(a) Z boson (b) $W^{\pm}$ boson

Figure 101: Mass peaks of the $W^{\pm}$ and Z bosons from larger statistics samples from the UA1 Collaboration [97].

noise. Observing the W^- boson involves examining its decay modes:

$$W^- \to \begin{cases} \bar{u} + d' & (3) \\ \bar{c} + s' & (3) \\ e^- + \bar{\nu}_e & (1) \\ \mu^- + \bar{\nu}_\mu & (1) \\ \tau^- + \bar{\nu}_\tau & (1) \end{cases} \tag{14.58}$$

The $W^- \to \bar{t}b$ is kinematically forbidden as the top quark mass $> m_W$. The brackets show the relative weight of the decay channel. The hadronic ones are weighted by 3 due to quarks having a choice of existing in three colour states.

Observing the W^- boson decaying via a leptonic channel $W^- \to e^- + \bar{\nu}_e$ was key. Ignoring quark flavour mixing and assuming each decay mode in (14.58) are equally likely (given ultrarelativistic limit of outgoing particles and universality of weak coupling), we can estimate its branching ratio:

$$\mathrm{B}\left(W^- \to e^- + \bar{\nu}_e\right) \approx \frac{1}{3+3+1+1+1} = \frac{1}{9}. \tag{14.59}$$

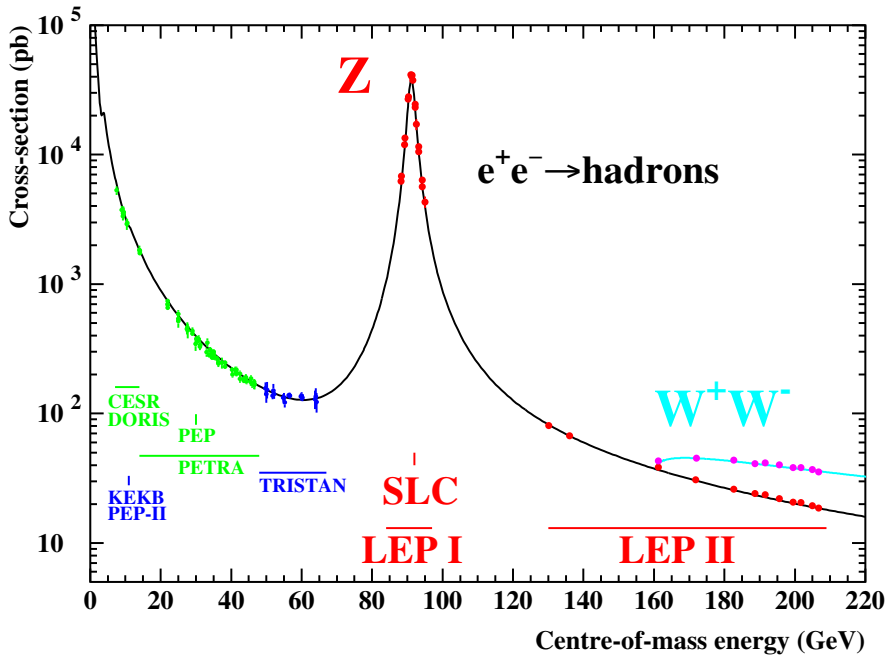

Figure 102: Measurements of e^-e^+ annihilation through LEP energies, from Ref. [87]

This decay produces a signature asymmetric track: the electrically charged e^- is easily detected but the antineutrino carrying the remaining momentum is very weakly interacting and does not leave a track.

With no QCD hadronic backgrounds to contend with, electron-positron collisions allow us to measure properties of the $W^\pm$ and Z^0 boson are most precisely. The reactions that take place are

$$e^+ + e^- \to X \to W^+ + W^-, \tag{14.60}$$

mediated by X, which can be a Z boson, photon γ or neutrino ν_e. This threshold is shown at high energies in figure 102.

14.5 Invisible width of Z boson

We exploit the fact all Standard Model fermions couple to the Z^0 boson equally to reveal an upper bound of only three neutrino types with masses below $< m_{Z^0}/2$. Considering the decay of Z^0 in its rest frame, we have the following observed states:

$$Z \to q\bar{q}, \quad q = u,d,s,c,b, \quad \text{(top too heavy)} \tag{14.61}$$

$$Z \to \ell\bar{\ell}, \quad \ell = e^-, \mu^-, \tau^-. \tag{14.62}$$

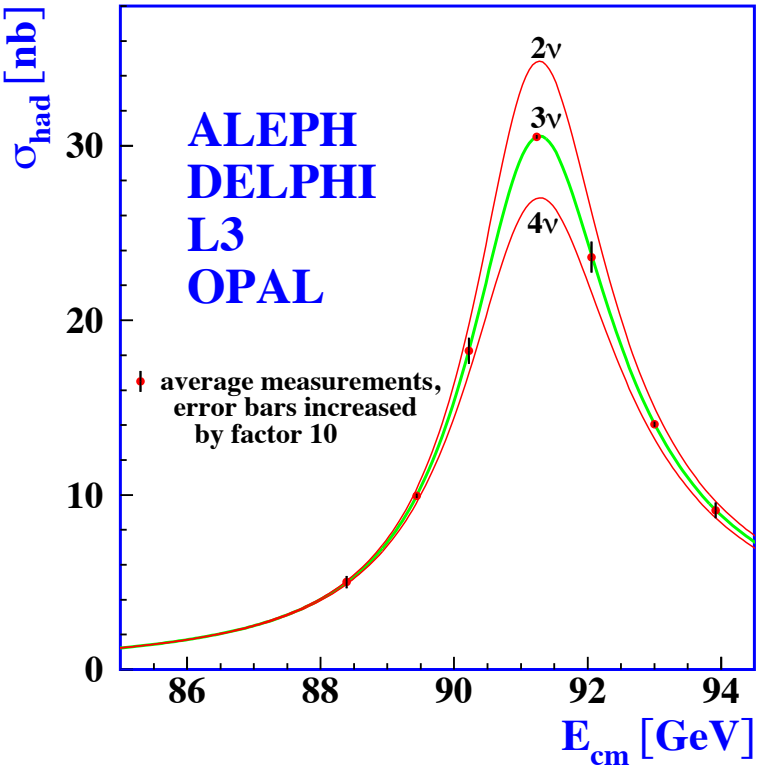

Figure 103: Invisible width of Z boson and number of neutrinos. The data are a combination of the four LEP experiments at CERN, where the measurement error bars are inflated by a factor of ten for visibility. Reproduced from the final LEP Z boson properties report [87].

The Breit–Wigner resonance gives:

$$\sigma = \frac{12\pi}{m_Z^2}\frac{\Gamma_e\Gamma_f}{\Gamma_Z^2}\frac{s\Gamma_Z}{(s-m_Z^2)^2+m_Z^2\Gamma_Z^2}. \tag{14.63}$$

It is found in experiments that the sum of the partial widths (observed decay channels) does not equal the full width (all possible decay channels):

$$\sum_{\text{observed}\,i}\Gamma_i \neq \Gamma_{\text{FWHM}}. \tag{14.64}$$

where i refers to all the observed states of (14.61) and (14.62).

This implies is some "invisible width" from which we infer the existence of further decay channels to neutrinos. We can measure the decay width of each decay channel to each type of neutrino pair $\Gamma_{\nu\bar{\nu}} = \Gamma(Z \to \nu\bar{\nu})$ via neutral current elastic scattering reactions such as:

$$\nu + q \to \nu + q.$$

These measurements can be cross-checked using electroweak theory to calculate the fermion branching width is given by

$$\Gamma_f = \Gamma(Z \to f\bar{f}) = \frac{G_F\sqrt{2}}{12\pi} m_Z^3 (c_V^2 + c_A^2) N_{\text{colours}}, \tag{14.65}$$

where the vector electroweak coupling is $c_V = I_3 - 2Q\sin^2\theta_W$ and $c_A = I_3$, with $I_3, (Q)$ being the weak isospin (electromagnetic) charges for the fermions. Making measurements of all these widths in e^+e^- collisions, we can count the number n_ν of neutrino species:

$$\Gamma_{\text{FWHM}} = \sum_{\text{observed}\, i} \Gamma_i + n_\nu \Gamma_{\nu\bar{\nu}} \tag{14.66}$$

$$= \Gamma_{\text{hadrons}} + \Gamma_{ee} + \Gamma_{\mu\mu} + \Gamma_{\tau\tau} + n_\nu \Gamma_{\nu\nu} \tag{14.67}$$

The best value for the number of light neutrino species is

$$n_\nu = 2.984(8). \tag{14.68}$$

We infer there are three types of neutrinos with mass $< m_Z/2$. Figure 103 shows the data from the four LEP experiments compared with different hypotheses considered, where the data unambiguously favours the three-neutrino hypothesis. This rules out there being more than three generations of leptons in the Standard Model, but it does not preclude the existence of neutrinos heavier than $m_Z/2$.

15 Higgs boson discovery

The Standard Model does not predict the Higgs boson mass. Substituting the small perturbations around the electroweak vacuum $\Phi(x) = \frac{1}{\sqrt{2}}\begin{pmatrix} 0 \\ v+h(x) \end{pmatrix}$ (14.32) into the Higgs potential (14.28) gives

$$V(\Phi^\dagger\Phi) = \lambda\left[\frac{1}{2}(v+h)^2 - \frac{v^2}{2}\right]^2 = \underbrace{\lambda v^2 h^2}_{\text{mass}} + \underbrace{\lambda v h^3 + \frac{1}{4}\lambda h^4}_{\text{self-interactions}}. \tag{15.1}$$

We find the Higgs boson mass is identified as $m_h^2 = 2\lambda v^2$ along with cubic and quartic terms defining Higgs boson self-interactions. Nonetheless, there were several indications for the Higgs boson mass before the direct LHC observation (figure 104).

15.1 Higgs boson searches

The W boson mass receives radiative corrections parametrised by Δr

$$m_W^2 = \frac{\pi\alpha}{\sqrt{2}G_F \sin^2\theta_W}\frac{1}{1-\Delta r}, \tag{15.2}$$

where the dominant contributions are from

$$\Delta r = \Delta r_{\text{QED}} + \Delta r_{\text{Higgs}} + \Delta r_{\text{top}}. \tag{15.3}$$

Here the contributions $\Delta r_{\text{QED}} = 1 - \alpha/\alpha(m_Z)$ is due to the running of the fine structure constant, while the Higgs and top loop contribute:

$$\Delta r_{\text{Higgs}} = \frac{11G_F^2}{24\pi^2\sqrt{2}} m_Z^2 \cos^2\theta_W \ln\left(\frac{m_h^2}{m_Z^2}\right) \propto \ln m_h, \tag{15.4}$$

$$\Delta r_{\text{top}} = \frac{3G_F^2}{8\pi^2\sqrt{2}}\frac{\cos^2\theta_W}{\sin^2\theta_W} m_t^2 \propto m_t^2. \tag{15.5}$$

Note the top loop contributes large corrections due to its quadratic mass dependence compared to the Higgs boson's logarithmic corrections. Therefore, precision measurements of the electroweak couplings $G_F, \sin\theta_W$ together with the masses m_W, m_Z, m_t can indirectly constrain the Higgs boson mass m_h.

Direct LEP searches exclude a light Higgs boson $m_h > 114.5$ GeV, while precision electroweak combinations disfavour one that is too heavy $m_h < 285$ GeV at 95% CL. The best fit value from the LEP 2005 combination is $m_h = 129^{+74}_{-49}$ GeV [87]. In 2011, Tevatron direct searches excluded of around Higgs boson 160–170 GeV.

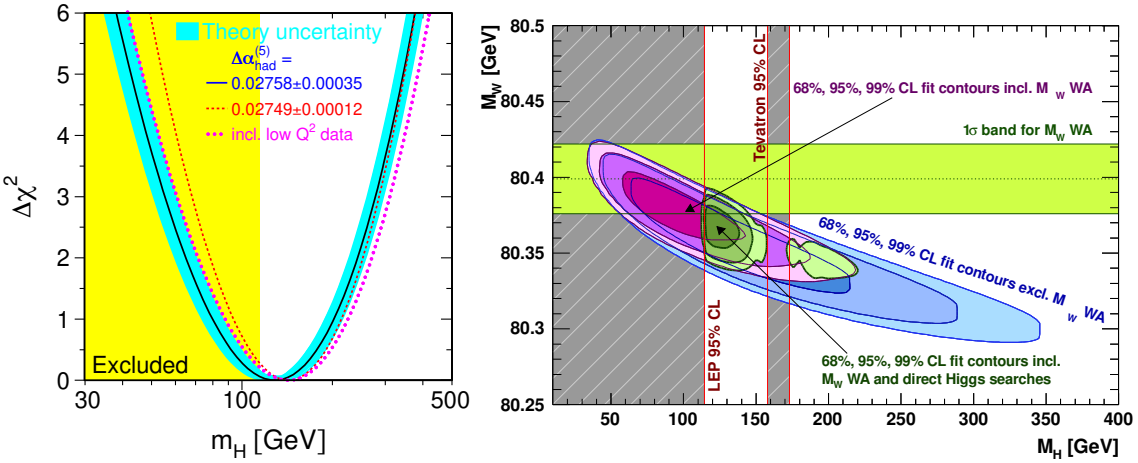

(a) LEP+SLD 2005 global fits [87] (b) Global fits 2011 with Tevatron exclusion [98]

Figure 104: Constraints on the Higgs boson mass from global electroweak data just after LEP finished in 2005. best fit Higgs boson mass of around 115 GeV, favouring masses $m_h <$ 285 GeV at 95% CL. In 2011, Tevatron direct searches excluded masses around 160 GeV.

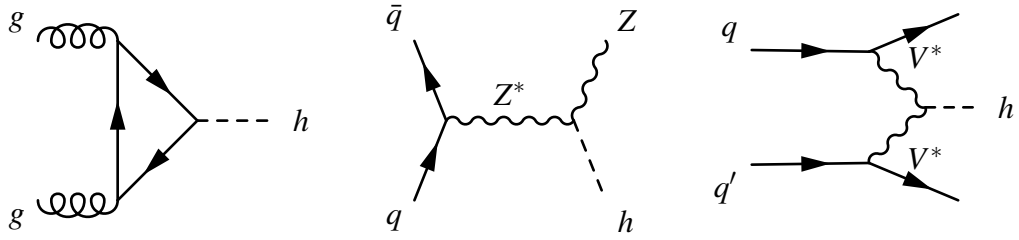

(a) Gluon-gluon fusion (b) Higgs-strahlung (c) Vector boson fusion

Figure 105: **Higgs boson production diagrams**. These show the important production mechanisms for the Higgs boson at the LHC.

Toward the end of 2011, ATLAS and CMS were analysing the first 7 TeV proton-proton collisions recorded at the LHC. There are a few different production modes of the Higgs boson:

- **Gluon-gluon fusion**: $gg \to h$ (figure 105a). A gluon from each of the protons fuse via a top quark loop. This has the highest cross-section at the LHC of all the production modes. At the LHC, the gluon parton distribution function from the protons dominate over the quarks. The top Yukawa coupling is the largest of all the quark loops, which dominates.

- **Higgs-strahlung**: $qq \to V^* \to Vh$, where $V = W/Z$ (figure 105b). This is also called **associated production**, where a Higgs boson in association with a gauge boson.

- **Vector boson fusion**: $qq \to q'(V^*V^* \to h)q'$ (figure 105c). Here quarks from each proton emit a virtual gauge boson W^*/Z^* that fuse into a Higgs boson. Two outgoing quarks form two additional jets, which are usually boosted in the forward direction.

The cross-sections for these are displayed in figure 107a, which steadily decrease with Higgs boson mass. The Higgs bosons decays depend strongly on the mass (figure 107b), but the primary channels used for the discovery were:

- **Diboson four-lepton** $h \to Z^*Z \to 4\ell$ (figure 106a). The small branching fraction is compensated by the relatively low background rate. The four-lepton invariant mass $m_{4\ell}$ distribution and a recent event display are shown in figure 108. In particular, the four leptons can either be electrons or muons, which are grouped into pairs of same-flavour opposite-sign pairs $(\ell^+\ell^-, \ell'^+\ell'^-)$, one of which satisfies an on-shell Z boson mass constraint $m_{\ell\ell} \in (m_Z \pm \Delta m)$.

- **Di-photon** $h \to \gamma\gamma$ (figure 106b). The branching fraction is only around 0.2%, but the excellent di-photon mass resolution of the ATLAS and CMS detectors means the signal-to-background rates are reasonable for discovery. The invariant mass distribution $m_{\gamma\gamma}$ and a recent event display are shown in figure 109.

- **Diboson semi-leptonic** $h \to W^*W \to \ell\nu_\ell\ell\nu_\ell$. This has a much higher branching fraction than the 4ℓ final state, but the two neutrinos makes reconstruction challenging.

- **Di-fermion** $h \to b\bar{b}, \tau^+\tau^-$ (figure 106c). Given the coupling is proportional to the fermion mass, these have large branching fractions. However, these hadronic signatures especially $b\bar{b}$ have very large backgrounds from QCD initiated processes such as gluon splitting $g \to b\bar{b}$. These channels do not contribute substantially to the discovery, but their later observation during 13 TeV runs play a pivotal role in testing the Yukawa structure of fermion couplings. Post-discovery, the branching ratios of $\mathscr{B}(h \to b\bar{b}) \approx 58\%$ and $\mathscr{B}(h \to \tau^+\tau^-) \approx 6.3\%$.

15.2 Discovery statistics

In data analysis or statistics classes, we first learn to fit data to some model expectation and quantify the goodness of fit. Among the simplest approaches is the method of *least*

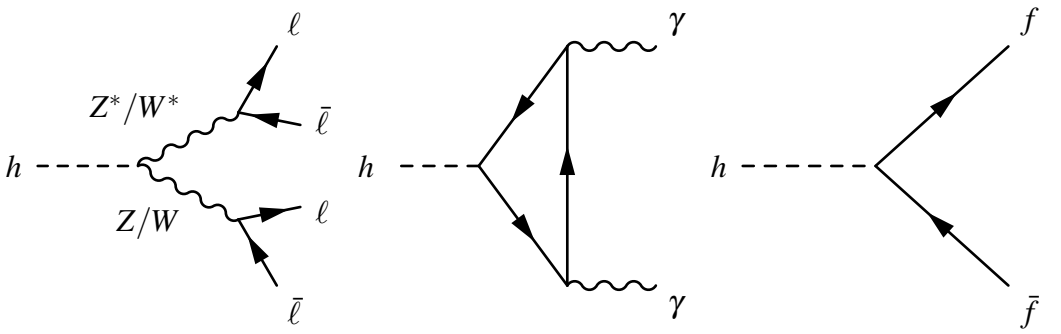

(a) Diboson (to four lepton) (b) Di-photon (c) Di-fermion

Figure 106: **Feynman diagrams of Higgs boson decays**. These are the key decay modes for discovering and characterising the Higgs boson.

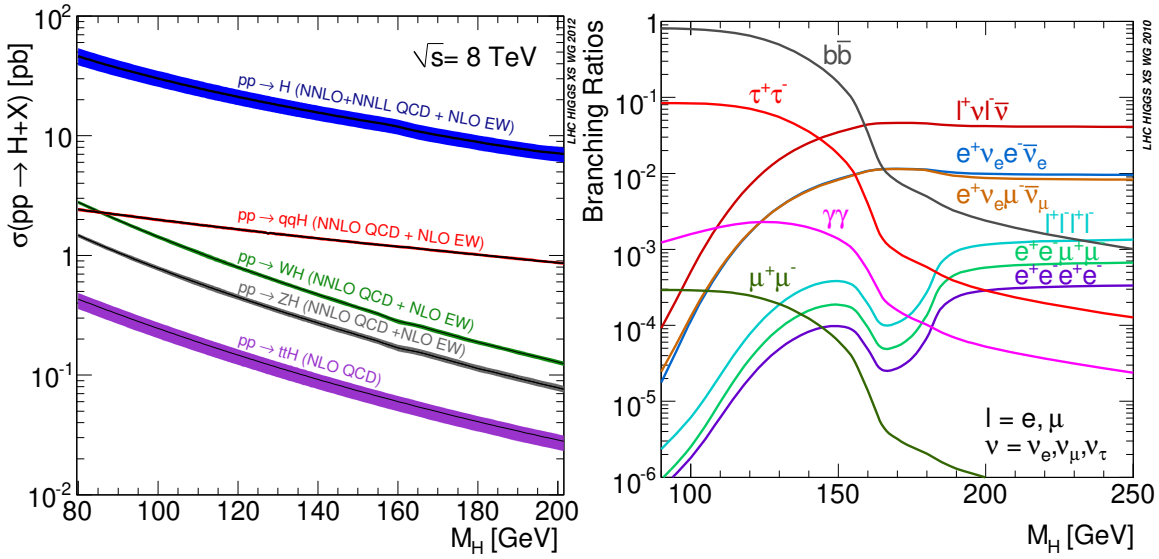

(a) LHC 8 TeV cross-section (b) Higgs branching fractions

Figure 107: **Higgs boson cross-sections and decays**. Standard Model Higgs boson production cross-section at 8 TeV vs mass and branching fraction with gauge boson decays into the observed lepton final states, from LHC Higgs Working Group.

squares, which minimises the sum of the square differences between the observed and model expectation given its uncertainties for each data point or bin i:

$$\chi^2 = \sum_i \frac{(\text{observed}_i - \text{expected}_i)^2}{(\text{uncertainty on expected})_i^2} = \sum_i \frac{(N^i_{\text{data}} - N^i_{\text{bkg}})^2}{\sigma^2_{\text{bkg},i}}. \tag{15.6}$$

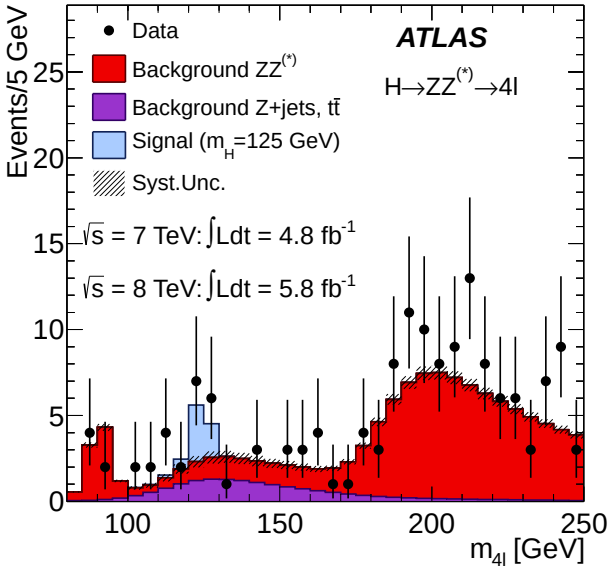

(a) ATLAS $h \to 4\ell$ 2011–12

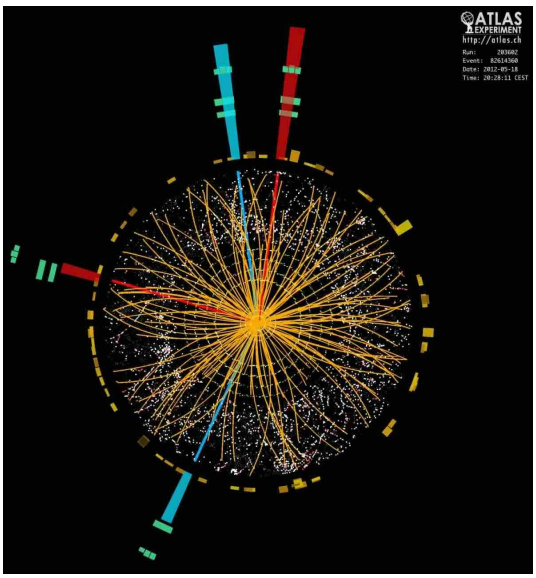

(b) Event display of $2e2\mu$

Figure 108: **ATLAS Higgs boson discovery: four-lepton channel**. The Higgs 4 lepton observed at the ATLAS Experiment in the $h \to 4\ell$ decay mode, which is the blue resonance peak centred at its 125 GeV mass. Images: Ref. [99], ATLAS-PHO-COLLAB-2012-007.

Not only is this intuitive, it is grounded in the statistics of the chi-square distribution. To discover new particles like the Higgs boson, we test the goodness of fit between two hypotheses: the background-only (null H_0) hypothesis with no Higgs boson and the background-plus-signal (alternative H_1) with a Higgs boson. As a rule of thumb (due to the central limit theorem), you will often see statistical significance Z formulas like

$$Z_{\text{stat}} \approx \frac{S}{\sqrt{B}}, \quad Z_{\text{stat+syst}} \approx \frac{S}{\sqrt{B + (\zeta_{\text{syst}} B)^2}} \tag{15.7}$$

as rough approximations of the signal significance for signal counts $S = N_{\text{obs}} - B$ above background counts B with uncertainties from only statistical fluctuations $\sigma_{\text{stat}} = \sqrt{B}$ or including systematic uncertainties $\sigma_{\text{syst}} = \zeta_{\text{syst}} B$. These apply in the limit where the background uncertainties follow a Gaussian distribution and the signal is small relative to the background.

For consistency between experiments, the LHC adopts community standards in presenting statistical analyses, detailed in Ref. [101, 102] with prominent NYU history spearheaded by Kyle Cranmer. These use the likelihood $L(\mu)$ function as a product of probabilities for observing event i

$$L(\mu) = \prod_i \text{Poisson}(i|\mu), \tag{15.8}$$

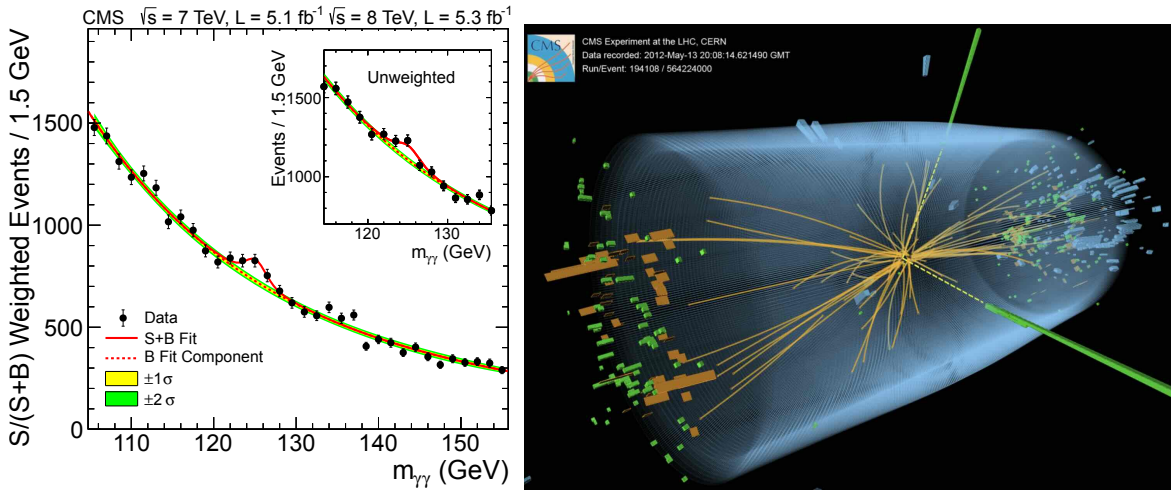

(a) CMS $h \to \gamma\gamma$ 2011–12 (b) Event display of $\gamma\gamma$

Figure 109: **CMS Higgs boson discovery: diphoton channel**. The original diphoton discovery data observed at the CMS Experiment using 2011–12 LHC data. Images: Ref. [100], CMS-PHO-EVENTS-2013-003.

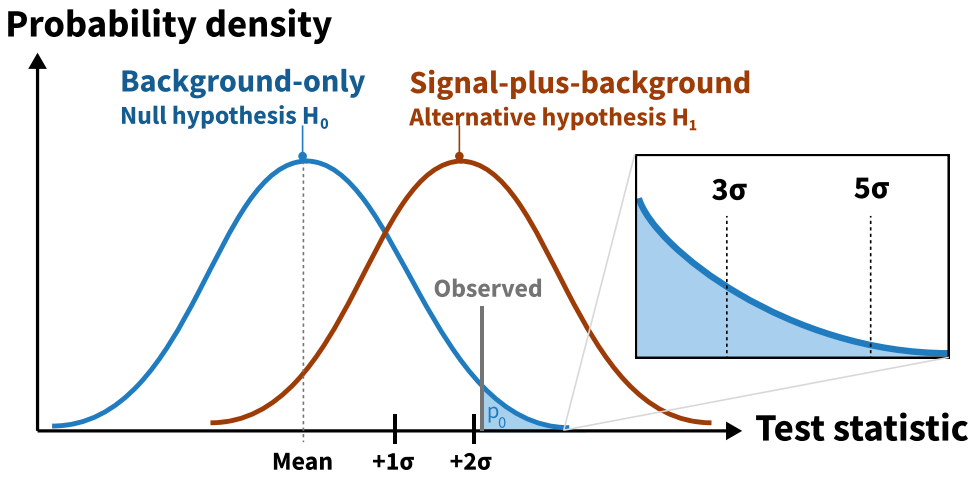

Figure 110: Sketch of probability distributions for test statistics and p-values for background-only and signal-plus-background hypotheses.

given a parameter μ characterising the presence of a signal, which follows a Poissonian distribution for random particle counts

$$\text{Poisson}(n|\lambda) = \frac{\lambda^n e^{-\lambda}}{n!}. \tag{15.9}$$

Figure 111: Selected photos from the 4th July 2012 event at the CERN main auditorium announcing the discovery of the Higgs boson. Centre shows Fabiola Gianotti announcing the ATLAS discovery. Right shows François Englert and Peter Higgs at the event. Images: CERN-HI-1207136-58.

For the scope of these lectures, we neglect systematic uncertainties in the likelihood. We then construct a test statistic called the **profile-likelihood ratio**[63] λ and the negative logarithm is taken (to turn products into summations) to give the profile log-likelihood q_μ:

$$q_\mu = -2\ln\lambda, \quad \lambda = \frac{L(\mu)}{L(\hat{\mu})}, \tag{15.10}$$

where $\hat{\mu}$ is the value of the signal parameter that maximises the likelihood L. You will often see the signal strength as the ratio of the fitted vs predicted $\mu = N_{\text{fit}}^{\text{signal}}/N_{\text{pred}}^{\text{signal}}$.

As we learn in statistics classes, we conduct statistical tests via two hypotheses:

- **Background-only hypothesis** (null hypothesis H_0) that sets signal $\mu = 0$ set to zero. We compute the probability that the test statistic is greater than that the data is compatible with the background-only hypothesis called the p-value

$$p_0 = 1 - p_b = \int_{q_0^{\text{obs}}}^{\infty} f(q_0|\mu = 0)\mathrm{d}q_0, \tag{15.11}$$

  where f is the probability density function of the test statistic, where Ref. [101] details asymptotic formulas for its determination.

- **Signal-plus-background hypothesis** (alternative hypothesis H_1) that is the scenario with a non-zero signal $\mu \neq 0$. We compute an analogous p-value for this hypothesis:

$$p_{s+b} = \int_{q_\mu^{\text{obs}}}^{\infty} f(q_\mu|\mu)\mathrm{d}q_\mu. \tag{15.12}$$

[63] For enthusiasts, the Neyman–Pearson lemma ensures the likelihood ratio is the most powerful test statistic.

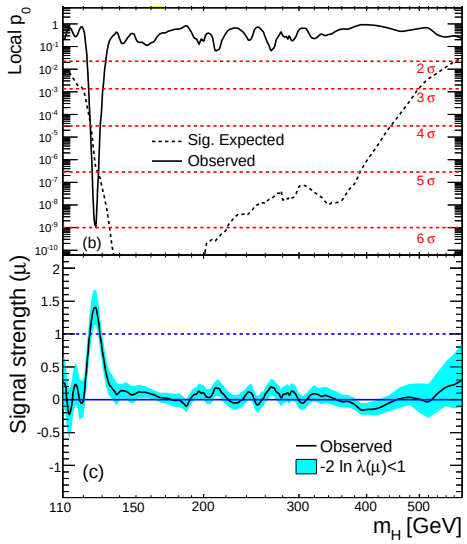

(a) ATLAS p-values [103]

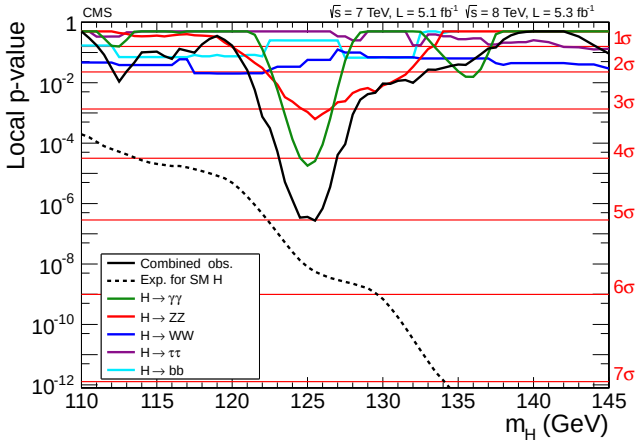

(b) CMS p-values by channel [100]

Figure 112: Statistical analysis combining the different production and decay modes during the SM Higgs boson searches during the initial years of the LHC.

The statistical significance is computed by

$$Z = \Phi^{-1}(1 - p_0), \tag{15.13}$$

where Φ is the inverse cumulative probability distribution. A statistical significance of 5 standard deviations (5σ) corresponds to a p-value $p_0 = 2.87 \times 10^{-7}$. Therefore, 5σ implies less 3 in 10 million chance an excess is due to statistical fluctuations alone. To exclude the presence of a signal, the LHC experiments uses a conservative $\mathrm{CL_s}$ value defined by

$$\mathrm{CL_s} = \frac{p_{s+b}}{1 - p_b}. \tag{15.14}$$

Injected signals with a μ parameter that causes $\mathrm{CL_s} < 0.05$ are excluded at 95% CL.

The ATLAS and CMS statistical analyses feature greater complexity, given they combine different Higgs boson production and decay channels, and account for systematic uncertainties. Figure 112a shows background-only p-values p_0 and the signal strength μ by the ATLAS combination for different Higgs boson masses m_h. Figure 112b shows the CMS p-value plot for different m_h separated by the different Higgs boson decay modes, showing the di-photon $\gamma\gamma$ and four-lepton $Z^*Z \to 4\ell$ channels dominate the discovery sensitivity. A new boson consistent with this Standard Model Higgs boson was announced in 2012 by the ATLAS [103] and CMS [100] Collaborations. This was promptly recognised by the 2013

Nobel prize in physics[64]. The mass of the Higgs boson was initially measured in 2012 to be

$$m_h(\text{ATLAS}) = 126.0 \pm 0.4\,(\text{stat}) \pm 0.4\,(\text{syst})\ \text{GeV}, \tag{15.15}$$

$$m_h(\text{CMS}) = 125.3 \pm 0.4(\text{stat}) \pm 0.5(\text{syst})\ \text{GeV}. \tag{15.16}$$

The statistical compatibility between the two independent collaborations and experimental apparatus is a gold standard of scientific reproducibility. The signal significance and statistical precision has since been improved with the large LHC dataset collected since.

15.3 Higgs–Yukawa interaction

A hallmark of the Higgs boson is that its interaction strength is characterised by the Yukawa coupling y_{hff} to fermions. The mass of the fermion is given by its coupling to the Higgs and the electroweak vacuum expectation value (v_{EW}):

$$m_f = \frac{y_f}{\sqrt{2}} v_{\text{EW}}. \tag{15.17}$$

Figure 113 shows a recent ATLAS measurements of Higgs coupling strengths to massive fermions and bosons. This provides a direct test of the dynamical structure of the Standard Model.

From the fermion-lepton Yukawa part of the electroweak Lagrangian (14.23), we have explicitly

$$\mathscr{L}_{\text{Yukawa}} = -y_\ell \left[\begin{pmatrix} \bar{\nu}_\ell & \bar{\ell} \end{pmatrix}_L \begin{pmatrix} \phi^+ \\ \phi_0 \end{pmatrix} \ell_R + \bar{\ell}_R \begin{pmatrix} \phi^{+\dagger} & \phi^{0\dagger} \end{pmatrix} \begin{pmatrix} \nu_\ell \\ \ell \end{pmatrix}_L \right] \tag{15.18}$$

Now recall from (14.32) that after symmetry breaking, the scalar fields in the unitary gauge become

$$\begin{pmatrix} \phi^+ \\ \phi^0 \end{pmatrix} = \frac{1}{\sqrt{2}} \begin{pmatrix} 0 \\ v + h(x) \end{pmatrix}. \tag{15.19}$$

Substituting this into (15.18) we obtain the Lagrangian after symmetry breaking

$$\mathscr{L} = -\frac{y_\ell v}{\sqrt{2}} \left(\bar{\ell}_L \ell_R + \bar{\ell}_R \ell_L \right) - \frac{y_\ell h(x)}{\sqrt{2}} \left(\bar{\ell}_L \ell_R + \bar{\ell}_R \ell_L \right) \tag{15.20}$$

We recognise the first set of terms are precisely the form of a Dirac fermion mass term:

$$\boxed{\mathscr{L} = \underbrace{-m_\ell \left(\bar{\ell}_L \ell_R + \bar{\ell}_R \ell_L \right)}_{\text{lepton mass term}} \underbrace{- \frac{m_\ell}{v} h(x) \left(\bar{\ell}_L \ell_R + \bar{\ell}_R \ell_L \right)}_{\text{lepton-Higgs interaction}}, \quad \text{where} \quad m_\ell = \frac{y_\ell v}{\sqrt{2}}.} \tag{15.21}$$

[64] https://www.nobelprize.org/prizes/physics/2013/summary/

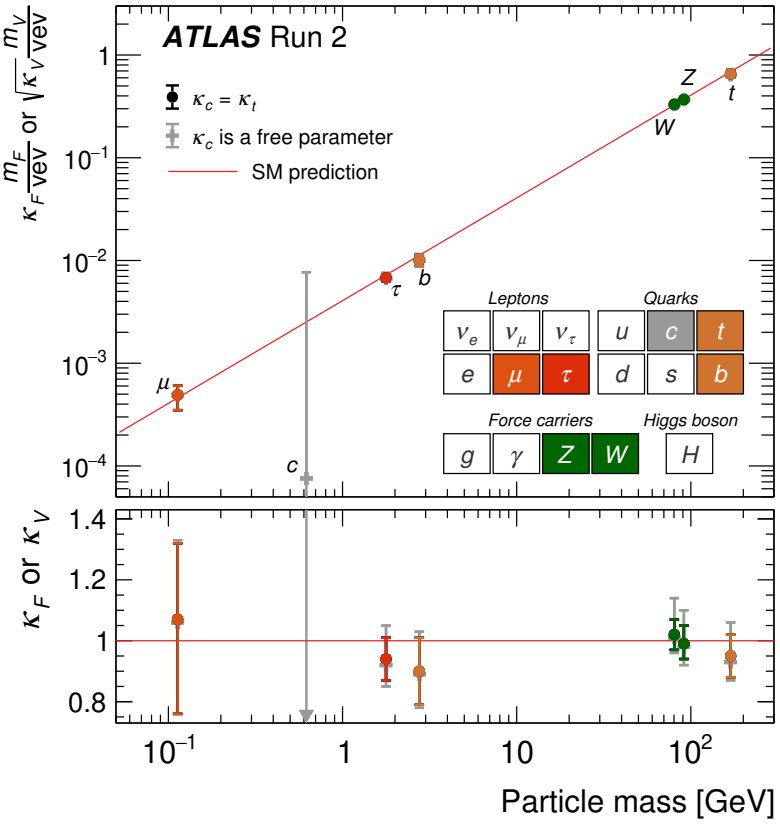

Figure 113: Higgs couplings measured relative to the Standard Model prediction from ATLAS [104] with similar measurements by CMS [105]. These measurements are from 2022, based on the full Run 2 LHC results. The red line shows the Standard Model expectation where the Higgs coupling is proportional to the mass of the particle.

The second term is the lepton-Higgs interaction term which gives the amplitude for leptons to emit a Higgs boson, with coupling m_ℓ/v. Originally, the Glashow–Salam–Weinberg model was developed to describe only leptons given quarks remained speculative in the 1960s and evidence for non-trivial neutrino masses was lacking. Remarkably, the quarks follow a similar construction with quark–Higgs mass generation mechanism analogous but slightly enlarged. We place the left-handed quarks into SU(2) doublets as

$$Q_L = \begin{pmatrix} q_u \\ q_d \end{pmatrix}_L \in \left\{ \begin{pmatrix} u_L \\ d_L \end{pmatrix}, \begin{pmatrix} c_L \\ s_L \end{pmatrix}, \begin{pmatrix} t_L \\ b_L \end{pmatrix} \right\}. \tag{15.22}$$

Quark	m_q [GeV]	$y_q = m_q(\sqrt{2}/v$
Up	$\approx 2.3 \times 10^{-3}$	$\approx 1.3 \times 10^{-5}$
Down	$\approx 4.8 \times 10^{-3}$	$\approx 2.8 \times 10^{-5}$
Strange	0.0958	5.51×10^{-4}
Charm	1.28	7.36×10^{-3}
Bottom	4.7	0.027
Top	173.2	0.996

Table 7: **Quark masses and Yukawa couplings**. Masses taken from reading off figure 5.

The right-handed quarks just exist as SU(2) singlets in their up and down types:

$$u_R^i = \{u_R, c_R, t_R\}, \quad d_R^i = \{d_R, s_R, b_R\}. \tag{15.23}$$

Then construct the Yukawa interactions analogously

$$\mathscr{L}_{\text{quark-Yukawa}} = -Y_u^{ij} \bar{Q}_L^i \tilde{\Phi} u_R^j - Y_d^{ij} \bar{Q}_L^i \Phi d_R^j, \tag{15.24}$$

where $\tilde{\phi} = \mathrm{i}\sigma_2 \phi^*$ with σ_2 being the second Pauli matrix. The i, j indices run over generations.

To reach the physical mass basis, we can rotate the quark fields in the flavour basis via a set of 3×3 unitary matrices $\mathbb{V}_d, \mathbb{V}_u$, conventionally:

$$d_L \to \mathbb{V}_d \cdot d_L, \quad u_L \to \mathbb{V}_u \cdot u_L, \tag{15.25}$$

$$d_R \to \mathbb{U}_d \cdot d_R, \quad u_R \to \mathbb{U}_u \cdot u_R. \tag{15.26}$$

This allows the reach the basis that is diagonal in masses for the Yukawa couplings

$$Y_d \to \mathbb{V}_d^\dagger \cdot Y_d \cdot \mathbb{U}_d = \begin{pmatrix} y_d & & \\ & y_s & \\ & & y_b \end{pmatrix}, \quad Y_u \to \mathbb{V}_u^\dagger \cdot Y_u \cdot \mathbb{U}_u = \begin{pmatrix} y_u & & \\ & y_c & \\ & & y_t \end{pmatrix}. \tag{15.27}$$

From the quark masses the mass, we can divide by $\sqrt{2}/(246\ \text{GeV})$ as predicted by the Standard Model to obtain the expected Yukawa couplings. These are displayed in table 7. We can then test this hypothesis by measuring the Yukawa couplings directly via events with e.g. tth processes for y_t. It is possible to performa similar exercise for the charged leptons. Figure 113 displays recent status of these measurements by the ATLAS Collaboration. Why is the top quark Yukawa coupling nearly unity and others span five orders of magnitude? We currently do not know.

15.4 Cabibbo–Kobayashi–Maskawa matrix

We see six degrees of freedom in the Yukawa matrices are for the six quark masses. There are actually four further independent degrees of freedom corresponding to angles and a complex phase. During the diagonalisation of the Higgs–Yukawa matrices, the quark fields in the charged-current interaction with the $W^{\pm}$ bosons (14.47) are also rotated:

$$j_{+}^{\mu} = \bar{u}_L \bar{\sigma}^{\mu} d_L \to \bar{u}_L \bar{\sigma}^{\mu} (\mathbb{V}_u^{\dagger} \mathbb{V}_d) d_L, \tag{15.28}$$

$$j_{-}^{\mu} = \bar{d}_L \bar{\sigma}^{\mu} u_L \to \bar{d}_L \bar{\sigma}^{\mu} (\mathbb{V}_u^{\dagger} \mathbb{V}_d)^{\dagger} u_L. \tag{15.29}$$

The combination $\mathbb{V}_u^{\dagger}\mathbb{V}_d$ is not the identity matrix but rather the **Cabibbo-Kobayashi-Maskawa (CKM) matrix**:

$$V_{\mathrm{CKM}} = \mathbb{V}_u^{\dagger} \mathbb{V}_d. \tag{15.30}$$

The discovery of a third generation of quarks, namely the bottom and top quark, naturally extends the Cabibbo mixing matrix into a 3×3 mixing matrix. Now we see the origin of quark flavour mixing proposed by Cabibbo: it actually comes from diagonalising the Higgs–Yukawa matrices to reach the mass basis! One conventional way to write the CKM matrix is via an equation for quark flavour mixing:

$$\begin{pmatrix} d' \\ s' \\ b' \end{pmatrix} = \begin{pmatrix} V_{ud} & V_{us} & V_{ub} \\ V_{cd} & V_{cs} & V_{cb} \\ V_{td} & V_{ts} & V_{tb} \end{pmatrix} \begin{pmatrix} d \\ s \\ b \end{pmatrix}, \tag{15.31}$$

$$(\text{mass basis}) = \quad V_{\mathrm{CKM}} \quad \times \quad (\text{flavour basis}). \tag{15.32}$$

We see that the upper left 2×2 part of the matrix is exactly the Cabibbo matrix. The mass basis comprises the states coupling to the Higgs boson while the flavour basis are the states coupling to the weak gauge bosons. This describes how each up-type quark mixes with the other three generations. The standard parametrisation of the CKM matrix [75] is to write it in terms of three Euler angles $\theta_{12}, \theta_{13}, \theta_{23}$, where $s_{ij} = \sin\theta_{ij}, c_{ij} = \cos\theta_{ij}$ and one irreducible complex phase δ

$$V_{\mathrm{CKM}} = \begin{pmatrix} 1 & 0 & 0 \\ 0 & c_{23} & s_{23} \\ 0 & -s_{23} & c_{23} \end{pmatrix} \begin{pmatrix} c_{13} & 0 & s_{13} e^{-\mathrm{i}\delta} \\ 0 & 1 & 0 \\ s_{13} e^{-\mathrm{i}\delta} & 0 & c_{13} \end{pmatrix} \begin{pmatrix} c_{12} & s_{12} & 0 \\ -s_{12} & c_{12} & 0 \\ 0 & 0 & 1 \end{pmatrix}. \tag{15.33}$$

The values of the four independent parameters comprising three angles and the complex phase are, as taken from the PDG 2024 update [75]:

$$\sin\theta_{12} = 0.22501 \pm 0.00068, \quad \sin\theta_{13} = 0.003732^{+0.000090}_{-0.000085} \tag{15.34}$$

$$\sin\theta_{23} = 0.04183^{+0.00079}_{-0.00069}, \qquad \delta \qquad = 1.147 \pm 0.026. \tag{15.35}$$

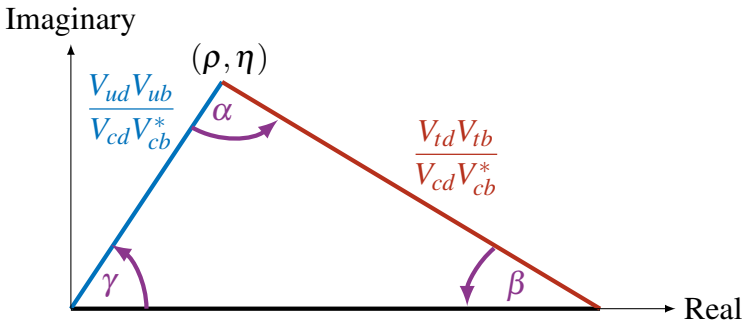

Figure 114: Sketch of CKM matrix unitarity triangle in the complex plane, with the angle names following the α, β, γ convention and base of triangle being unit normalised.

Interestingly, the values of the CKM matrix are nearly diagonal [75]:

$$\begin{pmatrix} |V_{ud}| & |V_{us}| & |V_{ub}| \\ |V_{cd}| & |V_{cs}| & |V_{cb}| \\ |V_{td}| & |V_{ts}| & |V_{tb}| \end{pmatrix} = \begin{pmatrix} 0.97435\,(16) & 0.22501\,(68) & 0.003732^{+0.000090}_{-0.000085} \\ 0.22487\,(68) & 0.97349\,(16) & 0.04183^{+0.00079}_{-0.00069} \\ 0.00858^{+0.00019}_{-0.00017} & 0.04111^{+0.00077}_{-0.00068} & 0.999118^{+0.000029}_{-0.000034} \end{pmatrix}. \quad (15.36)$$

We see the near-diagonal structure of the CKM matrix means quarks interactions via the weak force that stay within its own generation have the highest probability. This is strongest for the third generation, where we see $V_{tb} \approx 0.999$ being close to unity means a top-quark decays via the weak force predominantly to a bottom-quark, and very rarely to a down or strange quark due to the smallness of $V_{td} \approx 0.009$ and $V_{ts} \approx 0.04$, respectively. We can visualise the relative sizes of the CKM matrix elements to see the hierarchy of quark flavour mixing more clearly:

$$V_{\text{CKM}} \approx$$

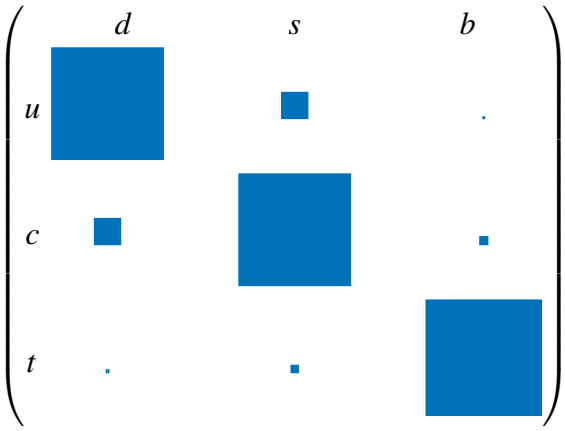

. (15.37)

Motivated by the near-diagonal structure in the CKM matrix elements, this is often re-

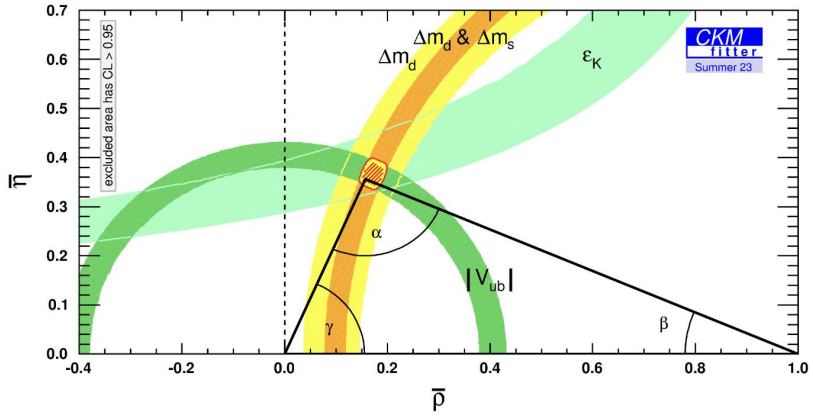

(a) Non-angle measurements

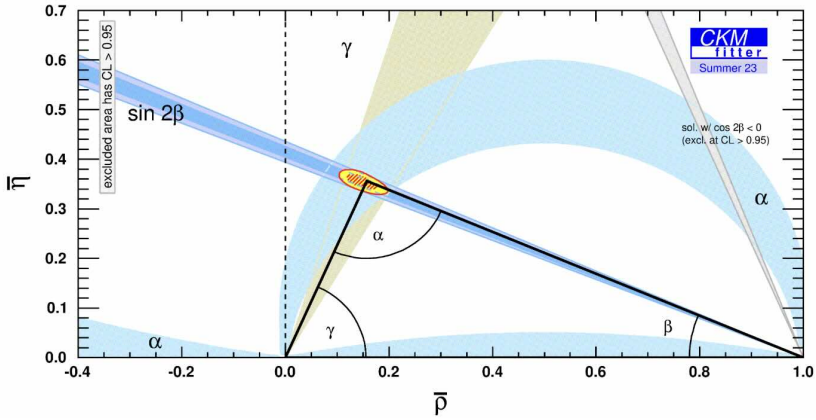

(b) Only angle measurements

Figure 115: Experimental constraints from the CKMFitter collaboration and the best fit values divided into measurements of the unitarity triangle lengths and angles.

casted into what is called the Wolfenstein parametrisation as an expansion in small λ:

$$V_{\text{CKM}} = \begin{pmatrix} 1 & 0 & 0 \\ 0 & 1 & 0 \\ 0 & 0 & 1 \end{pmatrix} + \lambda \begin{pmatrix} -\frac{\lambda}{2} & 1 & A\lambda^2(\rho - \mathrm{i}\eta) \\ -1 & -\frac{\lambda}{2} & A\lambda \\ A\lambda^2(\rho - \mathrm{i}\eta) & -A\lambda & 0 \end{pmatrix} + \dots$$
$$\approx \begin{pmatrix} 1 - \frac{\lambda^2}{2} & \lambda & A\lambda^3(\rho - \mathrm{i}\eta) \\ -\lambda & 1 - \frac{\lambda^2}{2} & A\lambda^2 \\ A\lambda^3(1 - \rho - \mathrm{i}\eta) & -A\lambda^2 & 1 \end{pmatrix}. \tag{15.38}$$

With this, λ, A, ρ, η are the four parameters mapped to the original three Euler angles and one phase, with the correspondence to the Cabibbo angle $\lambda \approx \sin\theta_{12}$. This approximation

is phenomenologically motivated and makes the hierarchical structure of the CKM matrix more manifest.

The CKM matrix is unitary in the Standard Model, where the unitarity conditions are $\sum_i V_{ij}V_{ik}* = \delta_{ij}, \sum_j V_{ij}V^*_{kj} = \delta_{ik}$. This leads to the CKM triangle constraints, where the standard choice for experimental tests is

$$1 + \frac{V_{ud}V^*_{ub}}{V_{cd}V^*_{cb}} + \frac{V_{td}V^*_{tb}}{V_{cd}V^*_{cb}} = 0 \tag{15.39}$$

As the right two terms are in general complex, we can plot this as a triangle, know as the **unitarity triangle**. Cecilia Jarlskog introduced an invariant J [106] to parametrise the amount of CP-violation, which is twice the area of the unitarity triangle using the cross product

$$J = \mathrm{Im}\,(V_{us}V_{cb}V^*_{ub}V^*_{cs}) = c_{12}s_{12}s_{13}s_{23}c^2_{13}\sin\delta = (2.96 \pm 0.20) \times 10^{-5}. \tag{15.40}$$

Measuring $J \neq 0$ implies the existence of CP violation and is equivalent to half the area of the unitarity triangle.

Figure 114 shows a sketch of this triangle in the complex plane adopting widely used convention. Figure 115 displays recent experimental constraints on the triangle.

Let us see how this relates to CP violation first observed in kaon mixing we introduced in section 12.5. Consider this matrix element for a kaon transitioning into its antiparticle:

$$\mathscr{M}(K \to \bar{K}) = \quad \propto V_{ud}V^*_{cs}V_{us}V^*_{cd}. \tag{15.41}$$

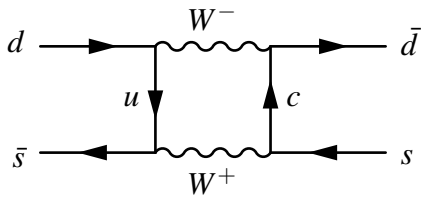

The *CP* conjugate process is

$$\mathscr{M}(\bar{K} \to K) \propto \quad \propto V^*_{ud}V_{cs}V^*_{us}V_{cd}. \tag{15.42}$$

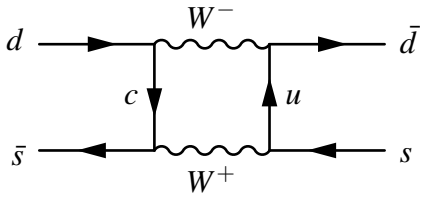

This is equivalent to the conjugating the matrix element $\mathscr{M}^*(K \to \bar{K})$. Because the CKM elements in such combinations have a non-zero imaginary part, CP violation is encapsulated by $\mathscr{M}(K \to \bar{K}) - \mathscr{M}(\bar{K} \to K) \neq 0$ being non-vanishing by an amount

$$\mathscr{M}(\bar{K} \to K) - \mathscr{M}(K \to \bar{K}) \propto \mathrm{Im}(V^*_{ud}V_{cs}V^*_{us}V_{cd}). \tag{15.43}$$

Together with other diagrams in the box loop, this sets the value of ε in equation (12.75).

The underlying origin of the three angles plus one complex phase, which appear to have non-random structure is unknown. It is an open question in particle physics. This is reminiscent of the periodic table first being constructed in the nineteenth century before quantum mechanics and atomic nuclei were discovered. It is similar to the particle zoo of hadrons in the 1950s, where the particle zoo of newly discovered hadrons motivated detailed measurement of mass, spin, lifetime properties before motivating a deeper explanation of the quark model and the strong force. This motivates significant research effort to measure and explain these values of the CKM matrix. This is **the problem of flavour**.

16 Massive neutrinos

The 2015 Nobel prize in physics[65] recognised the experimental evidence for atmospheric and solar neutrino oscillations, which were subsequently confirmed by laboratory and reactor neutrinos. This requires extending the conventional Standard Model to include neutrinos with non-zero mass differences.

16.1 Two-flavour oscillation model

The behaviour is elucidated using non-relativistic quantum mechanics. For algebraic simplicity, we consider the possibility of two flavours of neutrinos $\{\nu_e, \nu_\mu\}$ mixing. We assume their non-zero masses are not well-defined states, but are instead superpositions of mass eigenstates $\{i, j\}$. We write the electron-neutrino and muon-neutrino states as a mixed state, similar to quark flavour mixing:

$$\begin{pmatrix} |\nu_e\rangle \\ |\nu_\mu\rangle \end{pmatrix} = \begin{pmatrix} \cos\theta & -\sin\theta \\ \sin\theta & \cos\theta \end{pmatrix} \begin{pmatrix} |i\rangle \\ |j\rangle \end{pmatrix} \tag{16.1}$$

We suppose an electron-neutrino was produced at time $t = 0$ with well-defined momentum[66] $\mathbf{p}$. So the initial state of the electron-neutrino is

$$|\nu_e, \mathbf{p}\rangle = \cos\theta |i, \mathbf{p}\rangle - \sin\theta |j, \mathbf{p}\rangle \tag{16.2}$$

i.e. simply multiplying the top row of the matrix in (16.1).

Solving the time-dependent Schrödinger equation in stationary states, each term in the initial state (16.2) acquires a phase related to the energy of the corresponding mass eigenstate:

$$|\psi(t)\rangle = \exp(-\mathrm{i}E_i t)\cos\theta |i\rangle - \exp\big(-\mathrm{i}E_j t\big)\sin\theta |j\rangle \tag{16.3}$$

where we drop the $\mathbf{p}$ label in the kets. We now seek the amplitude for measuring $|\nu_\mu\rangle$ at some arbitrary time by using the linear combinations formed from the lower row of (16.1):

$$\langle\nu_\mu|\psi(t)\rangle = (\sin\theta|i\rangle + \cos\theta|j\rangle)\left(\mathrm{e}^{-\mathrm{i}E_i t}\cos\theta|i\rangle - \mathrm{e}^{-\mathrm{i}E_j t}\sin\theta|j\rangle\right). \tag{16.4}$$

Using orthogonality of the mass eigenstates, this becomes

$$\langle\nu_\mu|\psi(t)\rangle = \sin\theta\cos\theta\left(\mathrm{e}^{-\mathrm{i}E_i t} - \mathrm{e}^{-\mathrm{i}E_j t}\right). \tag{16.5}$$

[65] https://www.nobelprize.org/prizes/physics/2015/summary/

[66] We assume the momenta of both mass eigenstates are equal $\mathbf{p}_i = \mathbf{p}_j$ from the outset. This is a questionable assumption textbooks usually make, but this simplification turns out to agree with experiment rather well.

Extracting a factor of $e^{-i(E_i+E_j)/2}$ and taking the modulus square $|\langle \nu_\mu | \psi(t) \rangle|^2$ gives the probability of finding the neutrino in the muon type state:

$$P(\nu_e \to \nu_\mu, t) = \sin^2(2\theta) \sin^2 \left[\frac{(E_j - E_i)t}{2} \right] \tag{16.6}$$

Neutrinos are ultra-relativistic so we can make the binomial approximations

$$E_j - E_i = p\sqrt{1 + \left(\frac{m_j}{p}\right)^2} - p\sqrt{1 + \left(\frac{m_i}{p}\right)^2} \approx \frac{m_j^2 - m_i^2}{2p} \tag{16.7}$$

Then taking $E \approx p$, we see neutrinos travel a distance x in time t given by $x \approx ct$. With these approximations, we rewrite (16.6) as

$$\boxed{P(\nu_e \to \nu_\mu, x) \approx \sin^2(2\theta) \sin^2 \left(\frac{x}{L_{\text{osc}}} \right)} \tag{16.8}$$

where the characteristic oscillation length L_{osc} is

$$L_{\text{osc}} = \frac{4E}{\Delta m_{ij}^2}, \quad \Delta m_{ij}^2 = m_i^2 - m_j^2. \tag{16.9}$$

16.2 Atmospheric neutrinos

Atmospheric neutrinos provide evidence for neutrino oscillations. Energetic cosmic-rays striking the Earth's atmosphere produce showers of charge pions, which decays to muons with 99.988% probability (due to helicity suppression of weak decays):

$$\begin{aligned} \pi^+ &\to \mu^+ + \nu_\mu, \\ &\downarrow \\ &\mu^+ \to e^+ + \bar{\nu}_\mu + \nu_e \end{aligned} \tag{16.10}$$

and its charge conjugate for antiparticles. We therefore expect a 2 : 1 ratio of muon : electron type neutrinos.

$$R = \frac{N(\nu_\mu) + N(\bar{\nu}_\mu)}{N(\nu_e) + N(\bar{\nu}_e)} \approx 2 \tag{16.11}$$

This ratio allows the correlated systematic uncertainties related to the atmospheric neutrino flux to partly cancel. The Kamiokande and its upgrade Super-Kamiokande (Super-K) experiments[67] are located 1000 m underground in the Mozumi Mine of Kamioka, Japan. Super-K

[67] Originally, these experiments were constructed to look for proton decay $p \to e^+ + \pi^0$.

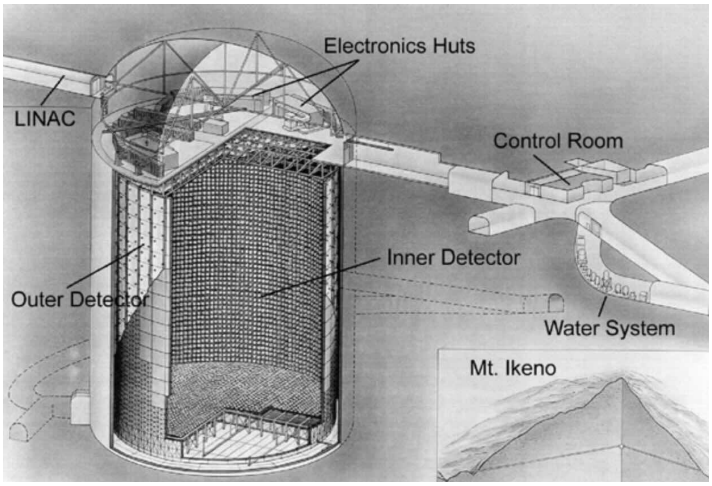

Figure 116: Super-Kamiokande detector situated in Mount Ikenoyama, Japan. Image: Ref. [107]

uses a large 40 m $\times$ 40 m vessel containing 50 kilotonnes of ultra-pure water surrounded by photomultiplier tubes to detect Cerenkov light from the neutrinos turning back into electrons or muons to identify its flavour. The electrons produce fuzzier rings due to electromagnetic showers in contrast to muons which are heavier. Experimental results present the double ratio $R' = R_{\text{obs}}/R^{\text{no-osc}}_{\text{model}}$, which should be unity if the no-oscillation model predicts the observed data.

The decisive experimental results came from Super-Kamiokande in 1998. They used a very large 535-day dataset comprising 33 kilotonne-years of exposure to report a significant overall deficit [108]:

$$\frac{R_{\text{obs}}}{R^{\text{no-osc}}_{\text{model}}} = 0.63 \pm 0.03\,(\text{stat.}) \pm 0.05\,(\text{syst.}) \tag{16.12}$$

This rejects the no-oscillation hypothesis $R_{\text{expectation}}/R^{\text{no-oscillation}}_{\text{model}} \simeq 1$ with high statistical significance.

Further evidence is available by measuring the rates as a function of propagation distance. Down-going and up-going atmospheric neutrinos traverse vastly different distances of the Earth's atmosphere vs diameter. Super-K can measure the zenith asymmetry of up-vs-down arrival of neutrinos $A = (N_{\text{up}} - N_{\text{down}})/(N_{\text{up}} + N_{\text{down}})$, where they define N_{up} for $-1 < \cos\Theta_Z < -0.2$ otherwise they are assigned to N_{down}. In no-oscillation models, the expectation should be zero. Instead they measure a significant deficit for muon-type neutrinos with GeV momenta:

$$A_{\text{osc}} = -0.296 \pm 0.048\,(\text{stat.}) \pm 0.01\,(\text{syst.}), \tag{16.13}$$

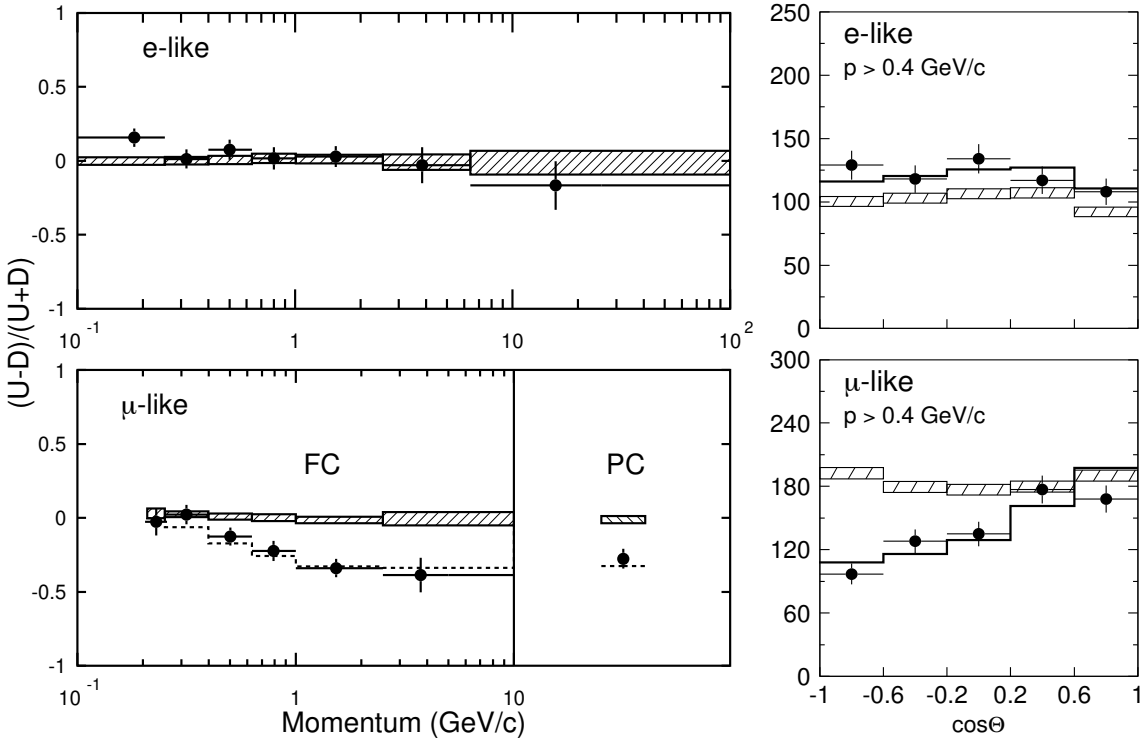

(a) Zenith asymmetry vs momentum

(b) Counts vs zenith angle

Figure 117: Atmospheric neutrino measurements from the 1998 Super-Kamiokande paper [108]. Hatched boxes show the simulated prediction from the no-oscillation model; lines (dotted on left, solid on right) show the best-fit to a $\nu_\mu \to \nu_\tau$ oscillation model. Upper (lower) panels show electron-like (muon-like) candidates. A zenith angle of $\cos\Theta_Z$ corresponds to directly overhead, $\cos\Theta_Z < 0$ is up-going and $\cos\Theta_Z > 0$ is down-going.

which alone rejects the no-oscillation hypothesis $A^{\text{no-osc}}_{\text{model}} \approx 0$ by over 6 standard deviations. Figure 117a shows this for electron-type and muon-type neutrinos as a function of momentum. Figure 117b shows this as a function of zenith angle for momenta $p > 0.4$ GeV. In both cases, there is a significant deficit for muon-type neutrinos, whereas electrons see no deficit. shows a significant deficit for muon-neutrinos arriving from below compared with above, consistent with $\nu_\mu \to \nu_\tau$ oscillations:

$$\text{Down-going} : \cos\Theta_Z > 0, \quad L^{\oplus}_{\text{atmosphere}} \approx 10\,\text{km}, \quad \nu_e, \nu_\mu \text{ little change}, \tag{16.14}$$

$$\text{Up-going} : \cos\Theta_Z < 0, \quad L^{\oplus}_{\text{diameter}} \approx 10\,000\,\text{km}, \quad \nu_\mu \to \nu_\tau \text{ inferred}. \tag{16.15}$$

These data represent the observation of atmospheric neutrino oscillations. Meanwhile, electron-neutrinos show no oscillations.

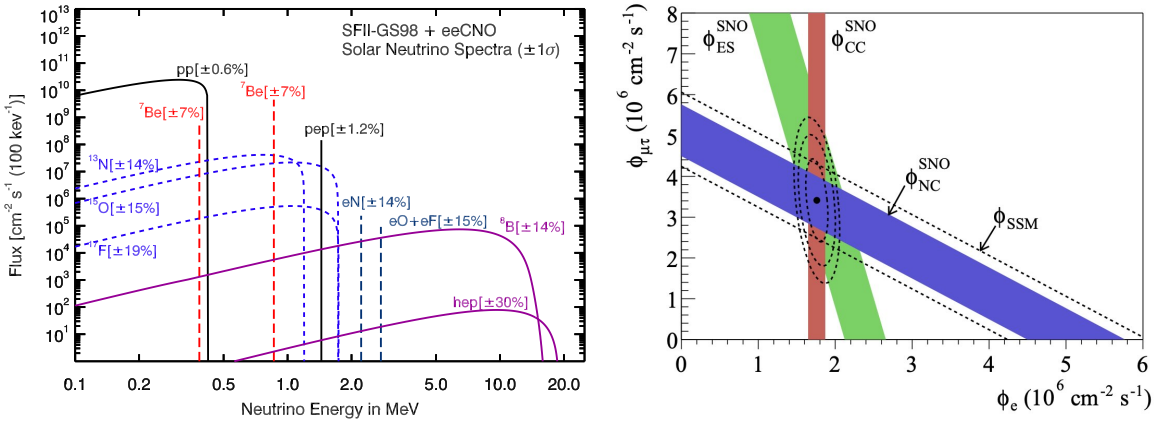

(a) Standard Solar Model neutrinos [109] (b) Measured fluxes by SNO [110]

Figure 118: Solar neutrino flux. The Standard Solar Model (SSM) shows the nuclear reactions in the Sun and the corresponding neutrino energy spectra, which only has sufficient energy to produce electron-type neutrinos ν_e. The SNO flux measurements for electron-type neutrinos ϕ_e and a significant combined muon-type and tau-type flux $\phi_{\mu\tau}$.

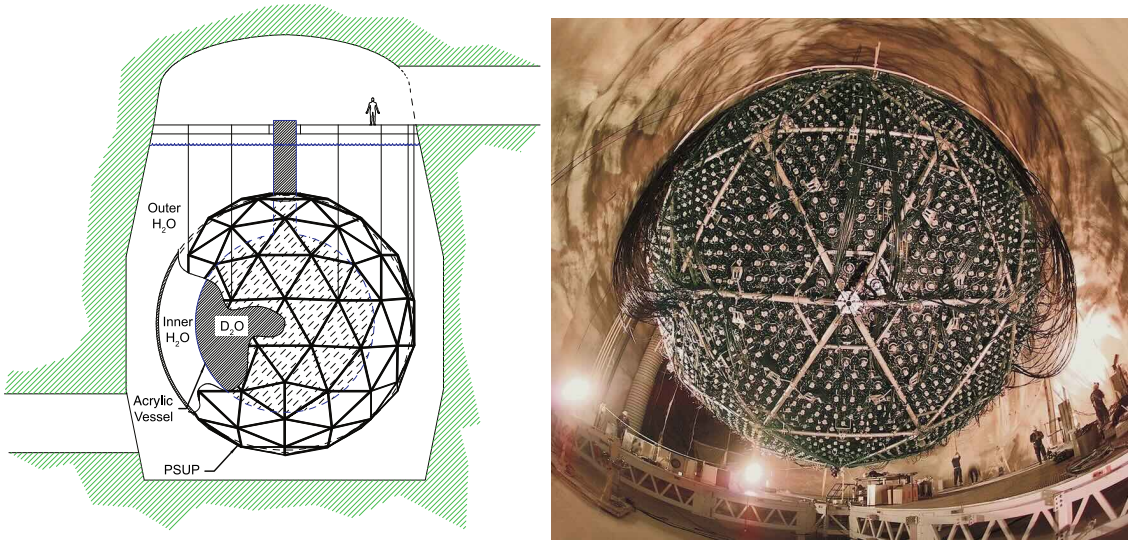

(a) Detector schematic (b) Detector photo

Figure 119: Sudbury Neutrino Observatory situated at Sudbury, Ontario, Canada. Images: Ref. [111], LBNL/R. Kaltschmidt

16.3 Solar neutrinos

Independent evidence of neutrino oscillations were observed with solar neutrinos. Undergoing nuclear fusion processes, the Sun only emits electron-type neutrinos under the reactions.

The pp cycle fusion reaction entails

$$4p \rightarrow {}^{4}_{2}\mathrm{He} + 2e^{+} + 2\nu_e + 26.73 \text{ MeV} \tag{16.16}$$

with the initial fusion being

$$p + p \rightarrow {}^{2}_{1}\mathrm{H} + e^{+} + \nu_e. \tag{16.17}$$

The photons carry most of the energy, with a small amount imparted into the neutrino kinetic energy $\langle E_{2\nu_e} \rangle = 0.59$ MeV. There are several other production mechanisms for solar neutrinos shown in figure 118a and understood from the Standard Solar Model:

$$^{7}\mathrm{Be} + e^{-} \rightarrow {}^{7}\mathrm{Li} + \nu_e + \gamma, \tag{16.18}$$

$$^{8}\mathrm{B} \rightarrow {}^{8}\mathrm{Be} + e^{+} + \nu_e. \tag{16.19}$$

We subsequently detect and identify electron-neutrinos through reactions involving the reaction

$$\nu_e + {}^{37}\mathrm{Cl} \rightarrow e^{-} + {}^{37}\mathrm{Ar} \tag{16.20}$$

To obtain a large source of chlorine atoms, 630 tonnes of C_2Cl_4 (perchloroethylene) often used for dry cleaning was procured and placed inside a vessel. Non-electron-type neutrinos cannot trigger this reaction. Therefore, any deficit in the measured amount of ^{37}Ar indicates neutrinos having oscillated to other flavours. This was first measured by Davis et al. in 1968. The Standard Solar Model of nuclear reactions without oscillations had a calculated capture rate of 7.6 solar neutrino units (SNU $\approx 10^{-36}$ captures per second). The observed result was 2.56 SNU, a third of the calculated rate. This suggests the ν_e has oscillated to equal amounts of ν_μ and ν_τ over its 149 million kilometre journey from the Sun to Earth.

More decisive evidence came from the Sudbury Neutrino Observatory (SNO) experiment. This comprises heavy water D_2O and detects three types of neutrino reactions

$$\nu_e + \mathrm{D} \rightarrow p + p + e^{-} \quad \text{charged current} \quad \text{(electron-neutrino only)}, \tag{16.21}$$

$$\nu_x + \mathrm{D} \rightarrow p + n + e^{-} \quad \text{neutral current} \quad \text{(all neutrino flavours)}, \tag{16.22}$$

$$\nu_x + e^{-} \rightarrow \nu_x + e^{-} \quad \text{elastic scattering} \quad \text{(all neutrino flavours)}. \tag{16.23}$$

These have the following reaction rates:

- Charged-current interaction can only produce electron type neutrinos because Solar neutrinos are produced via nuclear processes and have energies below the muon and tau-lepton mass threshold.

- Neutral current interaction via Z boson exchange occurs for all three neutrino flavours and can be tagged by its neutron emission compared to the charged current.
- Elastic scattering also occurs for all flavours with a signature of isolated electron recoil. This has a cross-section six times larger than for the neutral current case.

By carefully measuring these three rates, it is possible to determine the $\nu_e + \nu_\mu + \nu_\tau$ rate and fit for the flux from electron-type only vs muon-type plus tau-type neutrinos (figure 118b). The measured rates are [110]:

$$\phi_{\text{charged}} = 1.68 \pm 0.06\,(\text{stat.})^{+0.08}_{-0.09}\ (\text{syst.}), \tag{16.24}$$

$$\phi_{\text{neutral}} = 4.94 \pm 0.21\,(\text{stat.})^{+0.38}_{-0.24}\ (\text{syst.}), \tag{16.25}$$

$$\phi_{\text{elastic}} = 2.35 \pm 0.22\,(\text{stat.}) \pm 0.15\,(\text{syst.}) \tag{16.26}$$

This allowed SNO measured the flux ϕ of muon-type and tau-type neutrinos to be

$$\phi(\nu_\mu) + \phi(\nu_\tau) = 3.26 \pm 0.25\,(\text{stat.})^{+0.40}_{-0.35}\,(\text{syst.}) \tag{16.27}$$

This provides evidence that Solar electron-type neutrinos are oscillating into muon-type and tau-type neutrinos during its journey to Earth.

16.4 Neutrino mass determination

Determination of the neutrino mass hierarchy is a major research effort, and the following discussion is subject to be updated in the coming years. Global fits to oscillation data give the following measurements [75, 113]:

$$\Delta m^2_{21} = 7.50^{+0.22}_{-0.20} \times 10^{-5}\ \text{eV}^2, \tag{16.28}$$

$$|\Delta m^2_{32}| = 2.47^{+0.02}_{-0.03} \times 10^{-3}\ \text{eV}^2. \tag{16.29}$$

The sign of Δm^2_{32} being positive (negative) value is referred to **normal (inverted) ordering**. Combining recent oscillation with cosmological data give mild $\sim 2.5\sigma$ preference for normal ordering [75, 113].

The main absolute mass constraints come from kinematic endpoint measurements of tritium decay

$$^3\text{H} \rightarrow\ ^3\text{He} + e^- + \bar{\nu}_e. \tag{16.30}$$

Massive neutrinos distort the endpoint as illustrated in figure 120. The most recent limit for the electron-neutrino is from the Karlsruhe Tritium Neutrino (KATRIN) experiment [112]

$$m_{\nu_e} < 0.8\ \text{eV}, \quad 90\%\ \text{CL}. \tag{16.31}$$

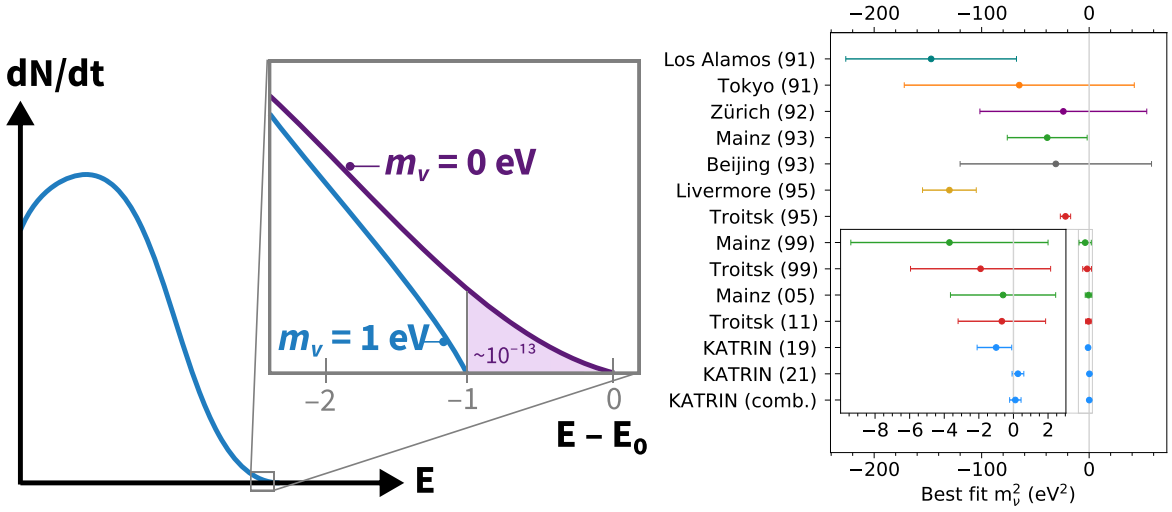

(a) Beta decay endpoint

(b) KATRIN constraints

Figure 120: **Beta decay spectrum for massless vs massive neutrinos**. Only around 2×10^{-13} of all decays reside in the last 1 eV. Right image: Ref. [112].

The value is still consistent with zero but the KATRIN experiment is expected to improve sensitivity to 0.2 eV:

$$m_\nu^2 = (0.26 \pm 0.34)\ \text{eV}^2. \tag{16.32}$$

The muon and tau neutrino masses have poorer laboratory constraints and arise from kinematic endpoint analyses of pion π^- and tau-lepton τ^- decays at 95% CL:

$$m_{\nu_\mu} < 190\ \text{keV}, \qquad \pi^- \to \mu^- + \bar{\nu}_\mu \quad [114], \tag{16.33}$$

$$m_{\nu_\tau} < 18.2\ \text{MeV}, \qquad \tau^- \to n\pi + \nu_\tau \quad [115]. \tag{16.34}$$

In a three-neutrino mixing scenario, distortions to tritium beta decay spectra lead to a lower bound on one of the neutrino species. This depends on the mass ordering scheme with the following bounds at 95% CL [75]:

$$m_{\nu_e} > 0.048\ \text{eV}, \qquad \text{normal ordering}, \tag{16.35}$$

$$m_{\nu_e} > 0.0085\ \text{eV}, \qquad \text{inverted ordering}. \tag{16.36}$$

Neutrinos on early universe cosmology leave their imprints the spectrum of the cosmic microwave background provide limits on the total mass of neutrino species being [75, 113]:

$$\sum_i \nu_i < 0.12\ (0.15)\ \text{eV} \qquad \text{normal (inverted) ordering}. \tag{16.37}$$

References

[1] G. Barr, R. Devenish, R. Walczak and T. Weidberg, "Particle Physics in the LHC Era." Oxford University Press, 978–0–19–874855–7, Open Access sponsored by SCOAP3 https://library.oapen.org/handle/20.500.12657/59108.

[2] X. Fan, T. G. Myers, B. A. D. Sukra and G. Gabrielse, *Measurement of the electron magnetic moment*, *Phys. Rev. Lett.* **130** (2023) 071801.

[3] L. Morel, Z. Yao, P. Cladé and S. Guellati-Khélifa, *Determination of the fine-structure constant with an accuracy of 81 parts per trillion*, *Nature* **588** (2020) 61.

[4] D. Clowe, M. Bradac, A. H. Gonzalez, M. Markevitch, S. W. Randall, C. Jones et al., *A direct empirical proof of the existence of dark matter*, *Astrophys. J. Lett.* **648** (2006) L109 [astro-ph/0608407].

[5] CERN, "History of the Universe." https://cds.cern.ch/record/39397, 1991.

[6] PLANCK collaboration, N. Aghanim et al., *Planck 2018 results. VI. Cosmological parameters*, *Astron. Astrophys.* **641** (2020) A6 [1807.06209].

[7] T. J. Berners-Lee, "Information Management: A Proposal." https://cds.cern.ch/record/369245, CERN-DD-89-001-OC (1989).

[8] A. Rao, "Screenshot of the recreated page of the first website." https://cds.cern.ch/record/2665153, 2019.

[9] M. Brice, "CERN Member State flags on the Esplanade des Particules." https://cds.cern.ch/record/2857083, 2023.

[10] A. Lasocki and R. J. Hicks, *How we read: the combined use of mri and novel pet tracers for the characterisation and treatment planning of masses in neuro-oncology*, *Cancer Imaging* **19** (2019) 57.

[11] S. Procureur et al., *Precise characterization of a corridor-shaped structure in Khufu's Pyramid by observation of cosmic-ray muons*, *Nature Commun.* **14** (2023) 1144.

[12] K. Morishima et al., *Discovery of a big void in Khufu's Pyramid by observation of cosmic-ray muons*, *Nature* **552** (2017) 386 [1711.01576].

[13] MURAVES collaboration, A. Giammanco et al., *Simulation Tools, First Results, and Experimental Status of the MURAVES Experiment*, *JAIS* **2024** (2024) 501 [2311.13663].

[14] R. Van Noorden, *Open-access deal for particle physics*, *Nature* **489** (2012) 486.

[15] S. Banerjee et al., *Environmental sustainability in basic research: a perspective from HECAP+*, 2306.02837.

[16] CERN, *Environment report 2021–22*, *CERN e-publishing* **3** (2023) .

[17] C. Burgard and S. Kottwitz, "Tikz Example: Standard model of physics." https://texample.net/tikz/examples/model-physics/.

[18] J. Woithe, G. J. Wiener and F. F. Van der Veken, *Let's have a coffee with the Standard Model of particle physics!*, *Phys. Educ.* **52** (2017) 034001.

[19] ATLAS Collaboration, "Standard Model Summary Plots June 2024." https://cds.cern.ch/record/2903866, 2024.

[20] C. T. R. Wilson, *On an expansion apparatus for making visible the tracks of ionising particles in gases and some results obtained by its use*, *Proc. R. Soc. Lond. A* **87** (1912) 277.

[21] E. Rutherford and H. Geiger, *An electrical method of counting the number of α-particles from radio-active substances*, *Proc. R. Soc. Lond. A* **81** (1908) 141.

[22] C. T. R. Wilson, *On a method of making visible the paths of ionising particles through a gas*, *Proc. R. Soc. Lond. A* **85** (1911) 285.

[23] N. G. J., *The β-ray spectrum of radium e*, *Proc. R. Soc. Lond. A* **17** (1940) 87.

[24] H. Geiger and E. Marsden, *Lxi. the laws of deflexion of a particles through large angles*, *The London, Edinburgh, and Dublin Philosophical Magazine and Journal of Science* **25** (1913) 604.

[25] E. Rutherford, *Lxxix. the scattering of α and β particles by matter and the structure of the atom*, *The London, Edinburgh, and Dublin Philosophical Magazine and Journal of Science* **21** (1911) 669.

[26] V. Nesvizhevsky and J. Villain, *The discovery of the neutron and its consequences (1930–1940)*, *Comptes Rendus Physique* **18** (2017) 592.

[27] I. Curie and F. Joliot, *Émission de protons de grande vitesse par les substances hydrogénées sous l'influence des rayons tres pénétrants*, .

[28] J. Chadwick, *Possible Existence of a Neutron*, *Nature* **129** (1932) 312.

[29] P. Carlson and A. De Angelis, *Nationalism and internationalism in science: the case of the discovery of cosmic rays*, *Eur. Phys. J. H* **35** (2010) 309 [1012.5068].

[30] "Domenico Pacini and the origin of cosmic rays." https://cds.cern.ch/record/1734821, 2012.

[31] V. F. Hess, *Über Beobachtungen der durchdringenden Strahlung bei sieben Freiballonfahrten (On the Observations of the Penetrating Radiation during Seven Balloon Flights)*, *Phys. Z.* **13** (1912) 1084.

[32] C. D. Anderson, *The positive electron*, *Phys. Rev.* **43** (1933) 491.

[33] P. M. S. Blackett and G. P. S. Occhialini, *Some Photographs of the Tracks of Penetrating Radiation*, *Proc. Roy. Soc. Lond. A* **139** (1933) 699.

[34] J. C. Street and E. C. Stevenson, *New evidence for the existence of a particle of mass intermediate between the proton and electron*, *Phys. Rev.* **52** (1937) 1003.

[35] PARTICLE DATA GROUP collaboration, R. L. Workman et al., *Review of Particle Physics*, *PTEP* **2022** (2022) 083C01.

[36] S. H. Neddermeyer and C. D. Anderson, *Note on the nature of cosmic-ray particles*, *Phys. Rev.* **51** (1937) 884.

[37] N. Nereson and B. Rossi, *Further measurements on the disintegration curve of mesotrons*, *Phys. Rev.* **64** (1943) 199.

[38] M. Conversi, E. Pancini and O. Piccioni, *On the disintegration of negative mesons*, *Phys. Rev.* **71** (1947) 209.

[39] C. Evoli, *The cosmic-ray energy spectrum*, .

[40] EAS-MSU, ICECUBE, KASCADE-GRANDE, NEVOD-DECOR, PIERRE AUGER, SUGAR, TELESCOPE ARRAY, YAKUTSK EAS ARRAY collaboration, H. P. Dembinski et al., *Report on Tests and Measurements of Hadronic Interaction Properties with Air Showers*, *EPJ Web Conf.* **210** (2019) 02004 [1902.08124].

[41] PIERRE AUGER collaboration, A. Aab et al., *Observation of a Large-scale Anisotropy in the Arrival Directions of Cosmic Rays above* 8×10^{18} *eV*, *Science* **357** (2017) 1266 [1709.07321].

[42] A. A. Michelson and E. W. Morley, *On the Relative Motion of the Earth and the Luminiferous Ether*, *Am. J. Sci.* **34** (1887) 333.

[43] G. Breit and J. A. Wheeler, *Collision of two light quanta*, *Phys. Rev.* **46** (1934) 1087.

[44] J. D. Cockcroft and E. T. S. Walton, *Experiments with high velocity positive ions. II. -The disintegration of elements by high velocity protons*, *Proc. Roy. Soc. Lond. A* **137** (1932) 229.

[45] "The Cockcroft-Walton Column." https://cds.cern.ch/record/39553, 1975, CERN-HI-7504054.

[46] B. Bell, H. Friedsam, W. Oren and R. E. Ruland, "Datum definition problems in accelerator alignment." https://cds.cern.ch/record/209215, 1990, SLAC-PUB-5226.

[47] S. Bethke and A. Wagner, *The JADE Experiment at the PETRA* e^+e^- *collider – history, achievements and revival*, *Eur. Phys. J. H* **47** (2022) 16 [2208.11076].

[48] W. E. Lamb and R. C. Retherford, *Fine structure of the hydrogen atom by a microwave method*, *Phys. Rev.* **72** (1947) 241.

[49] P. Kusch and H. M. Foley, *Precision measurement of the ratio of the atomic 'g values' in the* ${}^2p_{\frac{3}{2}}$ *and* ${}^2p_{\frac{1}{2}}$ *states of gallium*, *Phys. Rev.* **72** (1947) 1256.

[50] P. Kusch and H. M. Foley, *The magnetic moment of the electron*, *Phys. Rev.* **74** (1948) 250.

[51] J. S. Schwinger, *On Quantum electrodynamics and the magnetic moment of the electron*, *Phys. Rev.* **73** (1948) 416.

[52] R. H. Parker, C. Yu, W. Zhong, B. Estey and H. Müller, *Measurement of the fine-structure constant as a test of the Standard Model*, *Science* **360** (2018) 191 [1812.04130].

[53] T. Aoyama, T. Kinoshita and M. Nio, *Theory of the Anomalous Magnetic Moment of the Electron*, *Atoms* **7** (2019) 28.

[54] T. Aoyama, M. Hayakawa, T. Kinoshita and M. Nio, *Tenth-order qed contribution to the electron* $g-2$ *and an improved value of the fine structure constant*, *Phys. Rev. Lett.* **109** (2012) 111807.

[55] E. Tiesinga, P. J. Mohr, D. B. Newell and B. N. Taylor, *Codata recommended values of the fundamental physical constants: 2018*, *Rev. Mod. Phys.* **93** (2021) 025010.

[56] L3 collaboration, L3 Collaboration, *Measurement of the running of the electromagnetic coupling at large momentum-transfer at LEP*, *Phys. Lett. B* **623** (2005) 26 [hep-ex/0507078].

[57] I. Neutelings, A. Tsagkaropolulos and S. Kottwitz, "History timeline and energy scale of particle physics." https://tikz.net/timeline/.

[58] I. I. Rabi, J. M. B. Kellogg and J. R. Zacharias, *The magnetic moment of the proton*, *Phys. Rev.* **46** (1934) 157.

[59] I. I. Rabi, J. M. B. Kellogg and J. R. Zacharias, *The magnetic moment of the deuton*, *Phys. Rev.* **46** (1934) 163.

[60] L. W. Alvarez and F. Bloch, *A quantitative determination of the neutron moment in absolute nuclear magnetons*, *Phys. Rev.* **57** (1940) 111.

[61] R. Brown, U. Camerini, P. H. Fowler, H. Muirhead, C. F. Powell and D. M. Ritson, *Observations With Electron Sensitive Plates Exposed to Cosmic Radiation*, *Nature* **163** (1949) 82.

[62] G. D. Rochester and C. C. Butler, *Evidence for the Existence of New Unstable Elementary Particles*, *Nature* **160** (1947) 855.

[63] V. E. Barnes, P. L. Connolly et al., *Observation of a hyperon with strangeness minus three*, *Phys. Rev. Lett.* **12** (1964) 204.

[64] R. Hofstadter, *Electron scattering and nuclear structure*, *Rev. Mod. Phys.* **28** (1956) 214.

[65] B. Hahn, D. G. Ravenhall and R. Hofstadter, *High-Energy Electron Scattering and the Charge Distributions of Selected Nuclei*, *Phys. Rev.* **101** (1956) 1131.

[66] R. Hofstadter and R. W. McAllister, *Electron Scattering From the Proton*, *Phys. Rev.* **98** (1955) 217.

[67] D. R. Yennie, D. G. Ravenhall and R. N. Wilson, *Phase-Shift Calculation of High-Energy Electron Scattering*, *Phys. Rev.* **95** (1954) 500.

[68] M. Breidenbach, J. I. Friedman, H. W. Kendall, E. D. Bloom, D. H. Coward, H. DeStaebler et al., *Observed behavior of highly inelastic electron-proton scattering*, *Phys. Rev. Lett.* **23** (1969) 935.

[69] J. I. Friedman and H. W. Kendall, *Deep inelastic electron scattering*, *Ann. Rev. Nucl. Part. Sci.* **22** (1972) 203.

[70] C. G. Callan and D. J. Gross, *High-energy electroproduction and the constitution of the electric current*, *Phys. Rev. Lett.* **22** (1969) 156.

[71] GARGAMELLE NEUTRINO collaboration, H. Deden et al., *Experimental Study of Structure Functions and Sum Rules in Charge Changing Interactions of Neutrinos and anti-neutrinos on Nucleons*, *Nucl. Phys. B* **85** (1975) 269.

[72] J. J. Aubert, U. Becker, P. J. Biggs, J. Burger, M. Chen, G. Everhart et al., *Experimental observation of a heavy particle J*, *Phys. Rev. Lett.* **33** (1974) 1404.

[73] J. E. Augustin, A. M. Boyarski, M. Breidenbach, F. Bulos, J. T. Dakin, G. J. Feldman et al., *Discovery of a narrow resonance in e^+e^- annihilation*, *Phys. Rev. Lett.* **33** (1974) 1406.

[74] G. S. Abrams, D. D. Briggs, W. Chinowsky, C. E. Friedberg, G. Goldhaber, J. A. Kadyk et al., *Decay of $\psi(3684)$ into $\psi(3095)$*, *Phys. Rev. Lett.* **34** (1975) 1181.

[75] PARTICLE DATA GROUP collaboration, S. Navas et al., *Review of particle physics*, *Phys. Rev. D* **110** (2024) 030001.

[76] P. Soding, *On the discovery of the gluon*, *Eur. Phys. J. H* **35** (2010) 3.

[77] JADE collaboration, W. Bartel et al., *Observation of Planar Three Jet Events in e+ e- Annihilation and Evidence for Gluon Bremsstrahlung*, *Phys. Lett. B* **91** (1980) 142.

[78] CMS collaboration, S. Chatrchyan et al., *Measurement of the Ratio of the Inclusive 3-Jet Cross Section to the Inclusive 2-Jet Cross Section in pp Collisions at $\sqrt{s}$ = 7 TeV and First Determination of the Strong Coupling Constant in the TeV Range*, *Eur. Phys. J. C* **73** (2013) 2604 [1304.7498].

[79] M. L. Perl et al., *Evidence for anomalous lepton production in $e^+ - e^-$ annihilation*, *Phys. Rev. Lett.* **35** (1975) 1489.

[80] C. L. Cowan, F. Reines, F. B. Harrison, H. W. Kruse and A. D. McGuire, *Detection of the Free Neutrino: a Confirmation*, *Science* **124** (1956) 103.

[81] H. Bethe and R. Peierls, *The 'neutrino'*, *Nature* **133** (1934) 532.

[82] Christine Sutton, "Ghosts in the machine." https://cds.cern.ch/record/2232603, 2016.

[83] C. S. Wu, E. Ambler, R. W. Hayward, D. D. Hoppes and R. P. Hudson, *Experimental Test of Parity Conservation in β Decay*, *Phys. Rev.* **105** (1957) 1413.

[84] R. L. Garwin, L. M. Lederman and M. Weinrich, *Observations of the failure of conservation of parity and charge conjugation in meson decays: the magnetic moment of the free muon*, *Phys. Rev.* **105** (1957) 1415.

[85] M. Gell-Mann and A. Pais, *Behavior of neutral particles under charge conjugation*, *Phys. Rev.* **97** (1955) 1387.

[86] J. H. Christenson, J. W. Cronin, V. L. Fitch and R. Turlay, *Evidence for the 2π Decay of the K_2^0 Meson*, *Phys. Rev. Lett.* **13** (1964) 138.

[87] ALEPH, DELPHI, L3, OPAL, SLD, LEP Electroweak Working Group, SLD Electroweak Group, SLD Heavy Flavour Group, *Precision electroweak measurements on the Z resonance*, *Phys. Rept.* **427** (2006) 257 [hep-ex/0509008].

[88] J.-L. Caron, "LHC layout. Schema general du LHC." https://cds.cern.ch/record/841573, 1997.

[89] M. Brice, "Aerial View of the CERN taken in 2008." https://cds.cern.ch/record/1295244, 2008, CERN-MI-0807031.

[90] M. Brice and J. M. Ordan, "LHC tunnel point 1 various angles." https://cds.cern.ch/record/2302977, CERN-PHOTO-201802-030.

[91] P. Allport, *Applications of silicon strip and pixel-based particle tracking detectors*, *Nature Rev. Phys.* **1** (2019) 567.

[92] ATLAS Collaboration, *The ATLAS experiment at the CERN Large Hadron Collider: a description of the detector configuration for Run 3*, *JINST* **19** (2024) P05063 [2305.16623].

[93] ATLAS collaboration, S. Mehlhase, "ATLAS detector slice (and particle visualisations)." https://cds.cern.ch/record/2770815, 2021.

[94] ATLAS Collaboration, *Configuration and performance of the ATLAS b-jet triggers in Run 2*, *Eur. Phys. J. C* **81** (2021) 1087 [2106.03584].

[95] UA1 collaboration, G. Arnison et al., *Experimental Observation of Isolated Large Transverse Energy Electrons with Associated Missing Energy at $\sqrt{s} = 540$ GeV*, *Phys. Lett. B* **122** (1983) 103.

[96] UA2 collaboration, M. Banner et al., *Observation of Single Isolated Electrons of High Transverse Momentum in Events with Missing Transverse Energy at the CERN anti-p p Collider*, *Phys. Lett. B* **122** (1983) 476.

[97] UA1 collaboration, C. Albajar et al., *Studies of Intermediate Vector Boson Production and Decay in UA1 at the CERN Proton - Antiproton Collider*, *Z. Phys. C* **44** (1989) 15.

[98] GFITTER collaboration, M. Baak, M. Goebel, J. Haller, A. Hoecker, D. Kennedy, K. Moenig et al., *Updated Status of the Global Electroweak Fit and Constraints on New Physics*, *Eur. Phys. J. C* **72** (2012) 2003 [1107.0975].

[99] ATLAS Collaboration, *Measurements of the Higgs boson inclusive and differential fiducial cross sections in the 4ℓ decay channel at $\sqrt{s}$ = 13 TeV*, *Eur. Phys. J. C* **80** (2020) 942 [2004.03969].

[100] CMS Collaboration, *Observation of a New Boson at a Mass of 125 GeV with the CMS Experiment at the LHC*, *Phys. Lett. B* **716** (2012) 30 [1207.7235].

[101] G. Cowan, K. Cranmer, E. Gross and O. Vitells, *Asymptotic formulae for likelihood-based tests of new physics*, *Eur. Phys. J. C* **71** (2011) 1554 [1007.1727].

[102] ROOT collaboration, K. Cranmer, G. Lewis, L. Moneta, A. Shibata and W. Verkerke, *HistFactory: A tool for creating statistical models for use with RooFit and RooStats*, .

[103] ATLAS Collaboration, *Observation of a new particle in the search for the Standard Model Higgs boson with the ATLAS detector at the LHC*, *Phys. Lett. B* **716** (2012) 1 [1207.7214].

[104] ATLAS Collaboration, *A detailed map of Higgs boson interactions by the ATLAS experiment ten years after the discovery*, *Nature* **607** (2022) 52 [2207.00092].

[105] CMS collaboration, A. Tumasyan et al., *A portrait of the Higgs boson by the CMS experiment ten years after the discovery.*, *Nature* **607** (2022) 60 [2207.00043].

[106] C. Jarlskog, *Commutator of the quark mass matrices in the standard electroweak model and a measure of maximal* CP *nonconservation*, *Phys. Rev. Lett.* **55** (1985) 1039.

[107] SUPER-KAMIOKANDE collaboration, Y. Fukuda et al., *The Super-Kamiokande detector*, *Nucl. Instrum. Meth. A* **501** (2003) 418.

[108] SUPER-KAMIOKANDE collaboration, Y. Fukuda et al., *Evidence for oscillation of atmospheric neutrinos*, *Phys. Rev. Lett.* **81** (1998) 1562 [hep-ex/9807003].

[109] A. Serenelli, *Alive and well: a short review about standard solar models*, *Eur. Phys. J. A* **52** (2016) 78 [1601.07179].

[110] SNO collaboration, Q. R. Ahmad et al., *Direct evidence for neutrino flavor transformation from neutral current interactions in the Sudbury Neutrino Observatory*, *Phys. Rev. Lett.* **89** (2002) 011301 [nucl-ex/0204008].

[111] SNO Collaboration, *Constraints on neutrino lifetime from the sudbury neutrino observatory*, *Phys. Rev. D* **99** (2019) 032013.

[112] KATRIN collaboration, M. Aker et al., *Direct neutrino-mass measurement with sub-electronvolt sensitivity*, *Nature Phys.* **18** (2022) 160 [2105.08533].

[113] P. F. de Salas, D. V. Forero, S. Gariazzo, P. Martínez-Miravé, O. Mena, C. A. Ternes et al., *2020 global reassessment of the neutrino oscillation picture*, *JHEP* **02** (2021) 071 [2006.11237].

[114] K. Assamagan et al., *Upper limit of the muon-neutrino mass and charged pion mass from momentum analysis of a surface muon beam*, *Phys. Rev. D* **53** (1996) 6065.

[115] ALEPH collaboration, R. Barate et al., *An Upper limit on the tau-neutrino mass from three-prong and five-prong tau decays*, *Eur. Phys. J. C* **2** (1998) 395.